Fakultät für Medizin

Institut für Biologische und Medizinische Bildgebung

Analysis of optoacoustic efficiency and study of heterogeneous solid tumors with mesoscopic multispectral optoacoustic tomography

Juan Salichs San José

Abstract

In recent years, multispectral optoacoustic tomography (MSOT) has emerged as a powerful preclinical imaging modality and offers promising prospects in clinical practice, particularly to monitor cancer development. MSOT uniquely combines high optical contrast provided by optical imaging and high resolution at deep locations delivered by acoustic imaging. Thereby, MSOT permits the non-invasive acquisition of anatomical and functional information in a single experimental data set. Important considerations to further the capabilities of MSOT are the development of probes to enhance detection sensitivity of molecular targets and the design of new hardware to improve the spatial resolution.

Efficient probes are those capable of providing strong optoacoustic signals with a relative low injected dose and therefore reducing toxicity and side effects. First, optoacoustic efficiency is studied using common probes for small-animal optical imaging. Moreover, we developed an optoacoustic spectrometer for the analysis of the optoacoustic spectra of contrast agents at different concentrations in solution. Since measuring microenvironment gradients in solid tumors is important for pre-clinical and clinical research as well as development of theranostic methods, we next sought to study probes identified as efficient in tumor-bearing animals with optoacoustics. A novel mesoscopic MSOT system with enhanced resolution was then developed to examine microenvironment gradients. This mesoscopic system provides cross-sectional optoacoustic images with in-plane resolution of 50 μm and vertical resolution of 300 μm at tissue depths of about 15 mm. The system delivers superior three-dimensional images of nanoparticle distribution, heterogeneous vascular profiles and functional gradients within and around solid tumors in animal models.

Acknowledgements

The finalization of this thesis would not have been possible without the contribution and guidance of several people during the last 3 years. They support me with their knowledge, patience and motivation in the sometimes difficult path of research.

First of all, thanks to my advisor Prof. Dr. Vasilis Nzichristos who accepted me as Ph.D. student and gave me different approaches to pursue the objectives of my dissertation with his deep knowledge in the imaging field.

I am also grateful to my mentors Dr. med Mert Erkan and Dr. med. Rickmer Braren from the University Hospital Klinikum Rechts der Isar with their clinical advises.

I wish to thank Dr. Katrin Offe as coordinator of the Medical Life Science and Technology Ph.D. program and Desislava Zlatanova for the many administrative issues during the period of my studies.

I would like to thank all the members of IBMI for the feedback during the regular meetings of the group. Thanks to Prof. Dr. Daniel Razansky, Prof. Dr. Karl-Hans Englmeier and Prof. Dr. Gil Westmeyer for their valuable biomedical view. My deepest thanks to Dr. Xosé Luis Deán Ben for his support in various experiments and for his contribution with different reconstruction mathematical algorithms. In the same way I am thankful to Daniel Queirós, Andreas Bühler, Christian Lutzweiler, Alexander Dima, Lu Ding, Yiyong Han and Dr. Amir Rosenthal. I am truly thankful to Dr. Antonio Nunes and Dr. Vladimir Ermolayev for their work regarding tumor imaging. My special thanks to Murad Omar and Dr. Stephan Kellnberger for their technical advice and the time together in the office. I specially thank Panagiotis Symvoulidis for helping me with the cryoslice imaging system and Stratis Tzoumas for assisting me with the unmixing methods. I would also like to thank Karin Radrich in the experiments related to oxygen

Contents

List of figures

List of abbreviations

(AuNR) Gold nanorods

(BL) Beam length

(BW) Beam width

(CO_2) Carbon dioxide

(EMCCD) Electron multiplying charge-coupled device

(FCSI) Fluorescence cryosectioning imaging

(FEM) Finite Element method

(GUI) Graphical user interface

(Hb) Deoxygenated hemoglobin

(HbO_2) Oxygenated hemoglobin

(H&E) Hematoxylin and eosin

(ICG) Indocyanine green

(Lipo-ICG) Liposomes with ICG

(LSQR) Paige-Saunders iterative least-square QR decomposition

(MB) Mirror block

(MPE) Maximum permissible exposure

(MSOT) Multispectral optoacoustic tomography

(NO) Nitric oxide

(N_2) Nitrogen gas

(OAT) Optoacoustic tomography

(OD) Optical density

(OPO) Optical parametric oscillator

(O_3) Ozone

(RM-MSOT) Rotational Mesoscopic MSOT

(ROI) Region of interest

(SHG) Second harmonic generator

1 Objectives

Optoacoustic imaging has emerged as a powerful technique with the unique capacity to non-invasively acquire anatomical, functional and molecular information of biological samples using a single experimental setup. Being a hybrid technology, optoacoustic imaging combines key advantages provided by optical excitation in terms of rich contrast and ultrasound detection regarding resolution and penetration depth. In this way, by exciting biological tissues at several optical wavelengths, multispectral optoacoustic tomography (MSOT) enables visualization of deep-seated endogenous and exogenous optical absorbers with a much higher resolution than diffuse optical imaging techniques. Thereby, MSOT is becoming one of the most promising imaging technologies for preclinical studies, with unprecedented capabilities in biological studies of cancer diagnosis and treatment monitoring. Recently clinical optoacoustic systems have also been developed, exploiting the exclusive advantages of MSOT in the clinics, and promising prospects of optoacoustic imaging in the translation of biological studies are then expected.

Important next steps to advance on the capabilities of MSOT, particularly for molecular imaging applications, include the amplification of the detection sensitivity of molecular targets and improvement of the achievable spatial resolution. Thereby, the objective of this thesis was two-fold. On one hand, we embarked on studying the efficiency of optical probes in the generation of

optoacoustic signals. On the other hand, we aimed to develop and characterize a high-resolution MSOT system for preclinical studies.

One of the important aspects in the practical applicability of MSOT is the selection of an efficient probe that can originate a strong optoacoustic signal with a low dose concentration, thus minimizing toxicity and other adverse effects. In order to get an estimation of the efficiency of probes, defined as the optoacoustic signal generated per concentration unit, we studied different exogenous probes inserted into tissue-mimicking phantoms by imaging in a small-animal optoacoustic system. Furthermore, we designed an optoacoustic spectrometer in order to measure the intensity of the optoacoustic signals originated by endogenous and exogenous contrast agents at different concentrations and illumination wavelengths.

The spatial resolution of the imaging system is also an important element of MSOT. Particularly, examination of microenvironment gradients in solid tumors is a key factor for preclinical and clinical research, as well as development of theranostic methods. However, imaging with enhanced resolution is needed. Thereby, we aimed to develop and calibrate a novel mesoscopic optoacoustic imaging system capable of generating high-resolution optoacoustic images of tumor models. In this way, we intended to achieve superior capacities for three-dimensional imaging of external contrast agents distribution, heterogeneous vascular profiles, and functional gradients within and around solid tumors in preclinical cancer models. We expect that the results obtained with the mesoscopic optoacoustic imaging system have a high potential to contribute to new insights in the challenging field of molecular imaging in oncology, in particular by providing detailed information regarding neovascular and microenvironment gradients.

This dissertation is organized as follows. The main objectives are summarized in chapter 1. In chapter 2, the optoacoustic theory and imaging principles are introduced. In chapter 3, a study on the experimental measurement of the

optoacoustic efficiency of different probes is presented. The description and characterization of the novel rotational mesoscopic optoacoustic system is showcased in chapter 4 along with the tumor experiments performed with this system. Finally, the conclusions of the work and outlook are given in chapter 5.

2 Optoacoustic imaging background

2.1 The photoacoustic effect

The principle of optoacoustic imaging is based in the physical generation of acoustic waves due to light absorption and localized thermal expansion in a sample. The photoacoustic effect was first reported by Alexander Graham Bell in 1880 with the invention of the "photophone", in which a sunlight beam was reflected by a vocally modulated mirror and recovered with an ordinary telephone receiver attached to a selenium solar cell [1]. The speaker directed his voice to a plane mirror of flexible material and the surface became convex or concave, modulating the light with scattering or condensation. The receiver system used a selenium cell at the focus of a parabolic mirror to modulate the current into the circuit and convert it into sound in the earphone (Figure 2.1). On June 21, 1880, with the help of his assistant Charles Sumner Tainter, Bell was able to transmit a wireless voice message from the roof of the Franklin School to the window of Bell's laboratory (213 meters away). The results were published in the American Association for the Advancement of Science the same year.
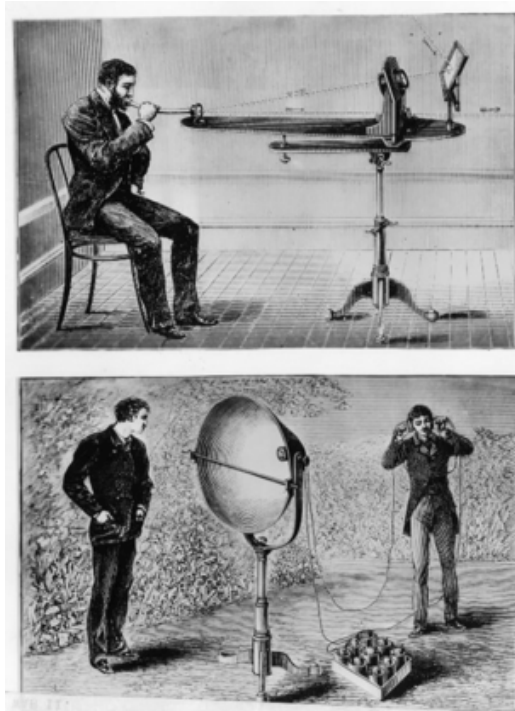
Figure 2.1: Invention of the photophone. Alexander Graham Bell developed the system for a wireless communication in 1880. The transmitter is shown in the top image, presenting the path of the reflected light before and after being modulated by the mirror. The lower image displays the receiver and the conversion of the modulated light into audible sound (collected at Washington Post Library on March 4, 1947. Reproduction from the original).

Graham Bell observed, while experimenting with the photophone, that a light beam interrupted rapidly (on the order of kHz) by rotating a slotted disk and then focused in a solid sample, was able to produce sound waves [2]. He noticed that the acoustic waves were dependent on the absorbing material sample and also on the intensity of the absorbed light beam. Bell additionally worked with non-visible light (infra-red and ultra-violet) and also detected sound in different samples.

As a result of Bell's discovery, he invented a device called the "spectrophone" in 1881 to use the optoacoustic effect in spectroscopy and spectral identification of materials (Figure 2.2). This device was a simple spectroscope equipped with a hearing tube instead of an eyepiece, where a chopped source of light was applied

[3]. Bell noted that the ear was not as good as the eye while examining the light spectrum and this technique was early abandoned until the development of intense light sources and sensitive detectors. He demonstrated the optoacoustic effect in the solid phase of matter and some years later, John Tyndall and Wilhelm Roentgen performed subsequent experiments with liquids and gases [4].
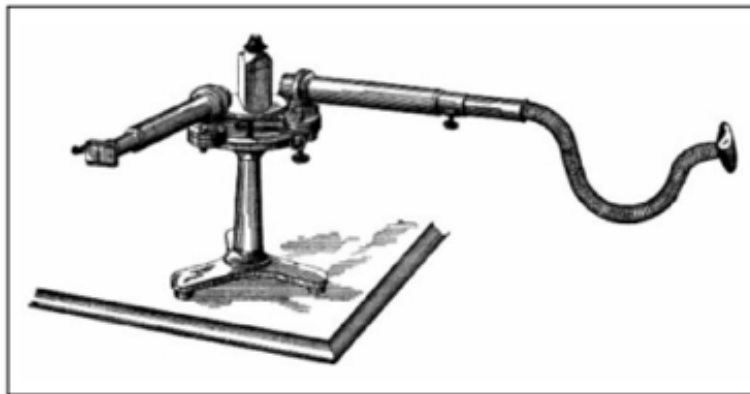
Figure 2.2: Spectrophone. The setup consists of a common spectroscope with a hearing tube instead of an eyepiece. Samples could be analyzed using the photoacoustic effect (image taken from Popular Science Monthly Volume 19).

Tyndall was the first person to report that the intensity of the sound created was proportional to the amount absorbed heat or applied light in the samples. Some years later, in 1938, the photoacoustic effect was applied in gas analysis [5]. Mark Leonidovich Veingerov measured CO_2 concentrations in N_2 gas down to 0.2% by volume with the photoacoustic effect. However, his measurements were affected by the low sensitivity of his microphone and the photoacoustic signal excited in the glass chamber.

The development of lasers in the 1960s [6] brought the advantages of high intensity light and tunable frequencies, increasing the amplitude and sensitivity of the optoacoustic signals and a wider use of this technology. As an example, the

optoacoustic effect was used to measure the O_3 depletion cause by nitric NO emission with a detector transported by a balloon in the early 1970s [7].

2.2 Ultrasonic transducers

Sound waves with frequencies higher than the human hearing range (approximately 20 KHz) are referred to as ultrasound. An ultrasonic transducer is a device that converts mechanical energy in the form of sound to electrical energy. The most widely used type of ultrasonic transducer is based on piezoelectric elements [8]. In this work, the optoacoustic signals are collected with this type of transducers. Thereby, a brief description of the components and ultrasound field parameters of piezoelectric transducers is provided in this section.

2.2.1 Components

The principal components of a piezoelectric transducer are the active element, backing and wear plate (Figure 2.3). The core of the transducer is the active element, which is made of a piezoelectric material. The active element transforms electrical energy into acoustic energy and vice versa with a polarized element and electrodes attached to the two opposite faces. The most commonly used materials are polarized ceramics that can be cut in different ways in order to create special wave modes. The backing is a dense material that controls the vibration of the transducer, absorbing the energy coming from the back face of the active element. The wear plate protects the transducer element from the environment. In the case of immersion transducers (detectors used in this work), the wear plate also acts as a matching layer reducing the acoustic impedance mismatch between the active element and water. With the matching layer being a ¼ wavelength thick

(λ/4) and an active element that is nominally λ/2, the waves created in the active element are in phase with the one reverberating in the matching layer. When signals are in phase in the transducer, their amplitudes are additive, avoiding a disruption in the wavefront.
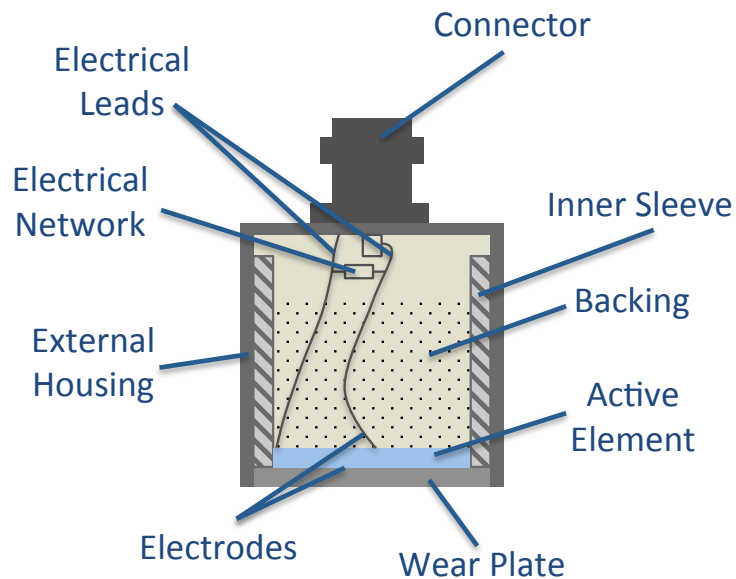
Figure 2.3: Main components of a piezoelectric transducer.

2.2.2 Sound field parameters

The sound field of a transducer is divided in two regions, known as the near field and the far field [9]. The near field is the area in front of the transducer where the echo amplitude has several maxima and minima. The near field ends in the last maximum at a distance N from the transducer. This distance N is the natural focus of the transducer, and beyond it, the sound energy gradually drops to zero in what is named the far field. The near field length is a function of several parameters of the transducer, including the element diameter D, the central

frequency f, and c the speed of sound in the measuring medium. It can be estimated as

$$N = D^2 f / 4c.$$

<div align="right">(2.1)</div>

On the other hand, diffraction effects limit the width and the length of the focal zone and certain spatial dimensions can then be defined.
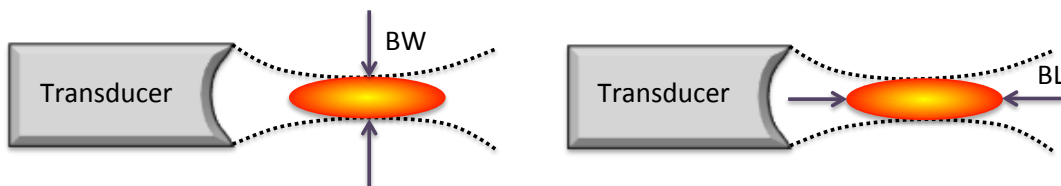
Figure 2.4: Focal zone of a transducer. The beam width (*BW*) is represented in the left and the beam length in the right (*BL*).

The -6 dB pulse-echo beam width (BW) for cylindrically-focused transducers (Figure 2.4) can be first approximated with

$$BW = \frac{1.02Fc}{fD},$$

<div align="right">(2.2)</div>

where F is the focal length of the transducer. The drop of -6 dB of the amplitude limits the beam length (BL) in Figure 2.4 and is given by

$$BL = \frac{2NS_F{}^2}{1 + 0.5S_F},$$

<div align="right">(2.3)</div>

where S_F is the normalized focal length defined as

$$S_F = F/N.$$

<div align="right">(2.4)</div>

Although near field interference and the exact shape of the transducer are not considered in Eqs. (2.1) to (2.4) some important parameters can be approximated while imaging, like the vertical and in-plane resolution.

2.3 Acoustic wave excitation and transmission

We review herein the mechanisms governing generation of ultrasound waves and subsequent transmission through an acoustic medium. In this way, a forward optoacoustic model is established that is then applied for deriving reconstruction strategies to form an image in OAT [10].

2.3.1 Stress and thermal confinement

Two parameters are important for optoacoustic excitation when laser pulses illuminate biological tissue. First, the stress relaxation time, which describes the pressure propagation, is defined as

$$\tau_s = \frac{d_c}{c},$$

<div align="right">(2.5)</div>

where d_c is the characteristic dimension of the heated region and c is the speed of sound. When the laser pulse duration τ_{pulse} is much shorter than τ_s, the excitation pulse is referred as been in *stress confinement,* which allows the assumption of neglecting the stress propagation in tissue. The stress confinement condition is then expressed as

$$\tau_{pulse} \ll \tau_s.$$

<div align="right">(2.6)</div>

The thermal relaxation time is defined as

$$\tau_{th} = \frac{d_c^2}{\alpha_{th}},$$

<div align="right">(2.7)</div>

with α_{th} expressing the thermal diffusivity (m^2/s). When the laser pulse width is much shorter than the thermal relaxation time, it is said that it is working in *thermal confinement* and the heat propagation during the pulse can be neglected. The thermal confinement condition is then expressed as

$$\tau_{pulse} \ll \tau_{th}.$$

<div align="right">(2.8)</div>

For laser pulse durations shorter than 100 ns, both confinement conditions are satisfied and the photoacoustic equation is further simplified. The laser pulse widths used in the experimental setups described in this dissertation were below this value.

2.3.2 Heating function

The heating function $H(r,t)$ refers to the thermal energy conversion per unit volume and unit time during a time shorter than the thermal confinement limit described above [11]. It is defined as

$$H(r,t) = \rho C_V \frac{\partial T(r,t)}{\partial t},$$

<div align="right">(2.9)</div>

where ρ is the mass density, C_V the medium's specific heat capacity at constant volume, and $(\frac{\partial T}{\partial t})$ the change of temperature over time. This formula relates the energy change according to the temperature variation.

2.3.3 Initial photoacoustic pressure

Taking into account that the heating and subsequent expansion due to pressure increment produces the photoacoustic waves, the derivation of the initial photoacoustic pressure starts with the Hooke's Law for thermal expansion [12]

$$\nabla \xi(r,t) = -\kappa p(r,t) + \beta T(r,t).$$

<div align="right">(2.10)</div>

Here $\nabla \xi(r,t)$ describes the fractional volume expansion $(\frac{dV}{V})$ in the form of a medium displacement; $p(r,t)$ represent the acoustic pressure and $T(r,t)$ symbolizes the temperature rise at time t and location r. The isothermal compressibility κ is defined as

$$\kappa = -\frac{1}{V}\left(\frac{\partial V}{\partial p}\right)_T = \frac{C_P}{\rho c^2 C_V}.$$

<div align="right">(2.11)</div>

The parameter ρ is the mass density, C_P is the specific heat capacity for constant pressure and C_V the equivalent specific heat capacity for constant volume. β in Eq. (2.10) is the thermal volume expansion coefficient and is expressed as

$$\beta = \frac{1}{V}\left(\frac{\partial V}{\partial T}\right).$$

<div align="right">(2.12)</div>

2.3.4 General photoacoustic equation

The motion equation (linear inviscid force equation) associates the force applied as a pressure change to the acceleration, given as a second derivative, i.e., [12]

14

$$\rho \frac{\partial^2}{\partial t} \xi(r,t) = -\nabla p(r,t),$$

(2.13)

where ξ represents the medium displacement. Taking the divergence of Eq. (2.13), it results in

$$\rho \frac{\partial^2}{\partial t^2} \left(\nabla \xi(r,t) \right) = -\nabla^2 p(r,t).$$

(2.14)

Eq. (2.14) can be replaced in Eq. (2.10) to obtain the general photoacoustic equation [13]

$$\left(\nabla^2 - \frac{1}{c^2} \frac{\partial^2}{\partial t^2} \right) p(r,t) = -\frac{\beta}{\kappa c^2} \frac{\partial^2 T(r,t)}{\partial t^2}.$$

(2.15)

Substituting Eq. (2.9) in Eq. (2.15), the photoacoustic equation can alternatively be expressed as

$$\left(\nabla^2 - \frac{1}{c^2} \frac{\partial^2}{\partial t^2} \right) p(r,t) = -\frac{\Gamma}{c^2} \frac{\partial H(r,t)}{\partial t},$$

(2.16)

where the Grueneisen parameter Γ is defined as

$$\Gamma = \frac{\beta}{\kappa \rho C_V} = \frac{\beta c^2}{C_P}.$$

<div align="right">(2.17)</div>

When the confinement conditions are satisfied, the energy absorption function can be expressed as [14]

$$H(r, t) = H_r(r)\delta(t),$$

<div align="right">(2.18)</div>

where $\delta(t)$ is the Dirac delta function. Eq. (2.16) can be simplified with the previous calculation as

$$\left(\nabla^2 - \frac{1}{c^2}\frac{\partial^2}{\partial t^2}\right)p(r, t) = -\frac{\Gamma}{c^2}H_r(r)\frac{\delta(t)}{\partial t}.$$

<div align="right">(2.19)</div>

Eq. (2.19) defines the conversion of heat into ultrasonic pressure waves. Tomographic acquisition of these signals around the sample with ultrasonic detectors is the basis of optoacoustic tomographic imaging as described in the next section.

2.4 Optoacoustic tomography

The photoacoustic effect is also the basic principle of biomedical optoacoustic (photoacoustic) imaging and tomography. Specifically, the excitation of acoustic waves within biological tissues consists of several steps. Initially, short light pulses are typically used to illuminate the sample and the light energy is absorbed. Then, the irradiated molecules become thermally excited, which subsequently leads to a volumetric expansion of the material and the creation of an acoustic pressure wave that propagates through the sample. Acoustic detectors are eventually employed to acquire the acoustic pressure at several positions around the illuminated sample (Figure 2.5).
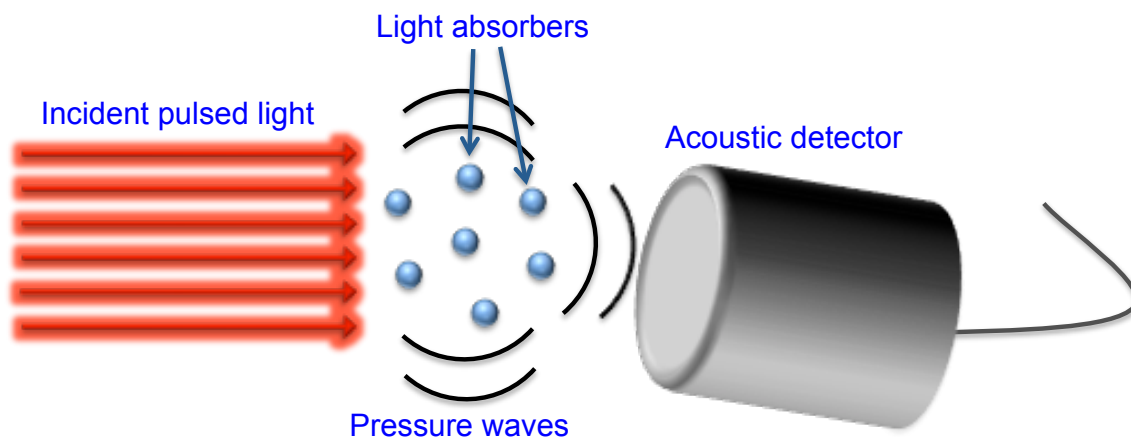
Figure 2.5: The photoacoustic effect.

Optoacoustic tomography (OAT) is able to recover the spatial distribution of optical absorption in biological samples by collecting optoacoustic signals at several locations around it and subsequent processing with a reconstruction algorithm [15–17]. Although the photoacoustic phenomenon was discovered more than one century ago, it was not used in medicine until nanosecond-range

pulsed lasers and sensitive transducers were commercially available. After local illumination with short laser pulses, individual transducers or ultrasonic detector arrays around the sample recover the generated acoustic waves. While the photoacoustic effect can be produced with any electromagnetic radiation able to create an increase of temperature, such as microwaves [18], light has the important advantage of rich contrast provided by the interaction of visible and near-infrared photons with molecules making up biological tissues [19,20]. OAT provides a spatial resolution in the order of a few hundred microns or less for imaging depths of several millimeters to centimeters, which is at least an order of magnitude higher as compared with other optical small-animal whole-body methods.

While anatomical images can be produced with OAT at single wavelengths, multiwavelength illumination in multispectral optoacoustic tomography (MSOT) offers the opportunity to distinguish different absorption profiles of contrast agents over background absorption after applying unmixing tools [21,22]. Common tissue cromophores are water, hemoglobin, melanin, lipids, etc (Figure 2.6).
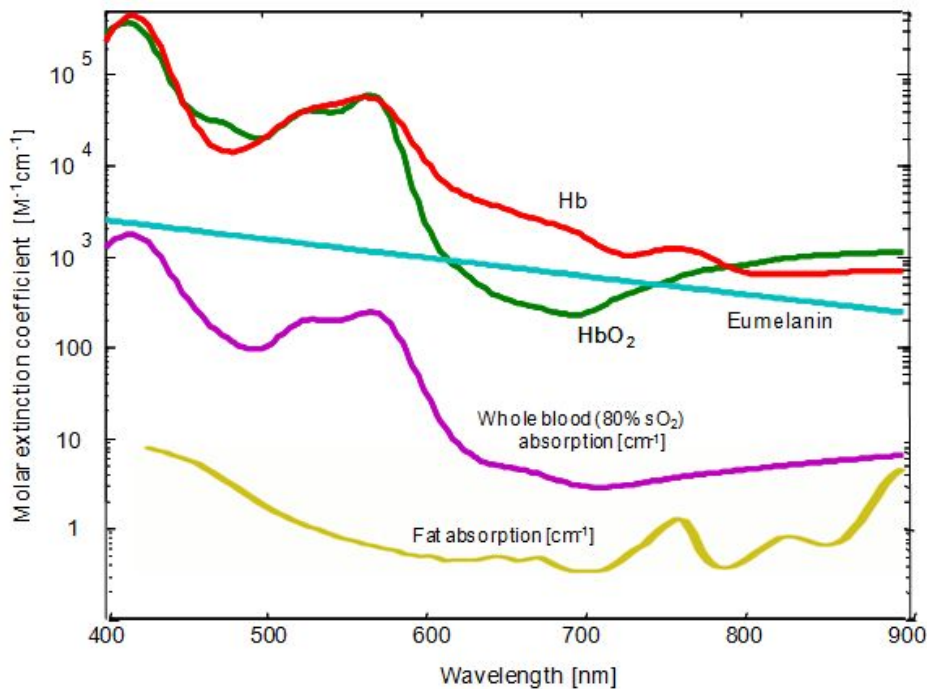
Figure 2.6: Spectra of principal cromophores in biological tissue. Each intrinsic absorber has a different molar extinction coefficient profile, and based of this, can be differentiated with MSOT (data taken from [23,24]).

Furthermore, a large range of photo-absorbing contrast agents are available with absorption profiles different to the endogenous background tissue absorbers. Thereby, as OAT provides good contrast and high resolution with a penetration depth equivalent to diffuse imaging optical techniques, it can be used to noninvasively image small animals or regions of the human body.

More specifically, MSOT offers the following advantages [25,26]:

- Breaks through the optical diffusion limit due to the low scattering of ultrasonic waves in tissues.
- Enables high-resolution imaging at different scales of biological structures.
- Reports superior contrast in relation to the chemical composition, using different optical wavelengths.
- Provides optical absorption with 100% sensitivity, higher than confocal microscopy and optical coherence tomography techniques.

- Delivers background-free detection, considering that the optoacoustic amplitude is proportional to the optical absorption, and tissue components without absorption present no background in the images.
- Involves no leakage of excitation photons into detectors, contrary to fluorescence imaging.
- Is speckle-free, contrary to optical coherence tomography and ultrasonography.
- Can potentially image all molecules considering that they are optically absorbing at some wavelengths.

Despite the large number of benefits, some factors have to be taken into account. First, the illumination source has to be sufficiently powerful to create a relatively high transient increase in the tissue temperature. In biological tissues, the excitation light pulse undergoes scattering and absorption as it reaches deeper locations and hence decreases in amplitude. The generated ultrasound waves also undergo different acoustic phenomena as they propagate through tissues. For example, regions with changes in the speed of sound or mass density lead to distortions in the acoustic wavefront. Acoustic attenuation also plays a role and limits the achievable imaging depth and resolution. Finally, effects specific to each ultrasound transducer can further lead to distortion in the collected signals. Therefore, as image formation in OAT depends on a reconstruction algorithm, the accuracy of the inversion model to account for all the aforementioned factors conditions the quantitativeness, resolution and overall image quality retrieved. Different reconstruction methods can be used, which are presented in the following section.

2.5 Image reconstruction methods

We review in this part two image reconstruction procedures applicable in the optoacoustic tomography systems employed in this work. The first one is a back-projection reconstruction algorithm commonly used in OAT and the second one is a model-based inversion procedure developed at our institute. Different variations of the model-based approach are described.

2.5.1 Back-projection reconstruction

This method is probably the most straightforward approach for image reconstruction in OAT. For each pixel, the optical absorption is estimated as the summation of the time dependent acoustic waves measured at different positions (projections) [27,28]. This procedure can be used for reconstructions in 2-dimensional (2-D) and 3-dimensional (3-D) optoacoustic systems [29].
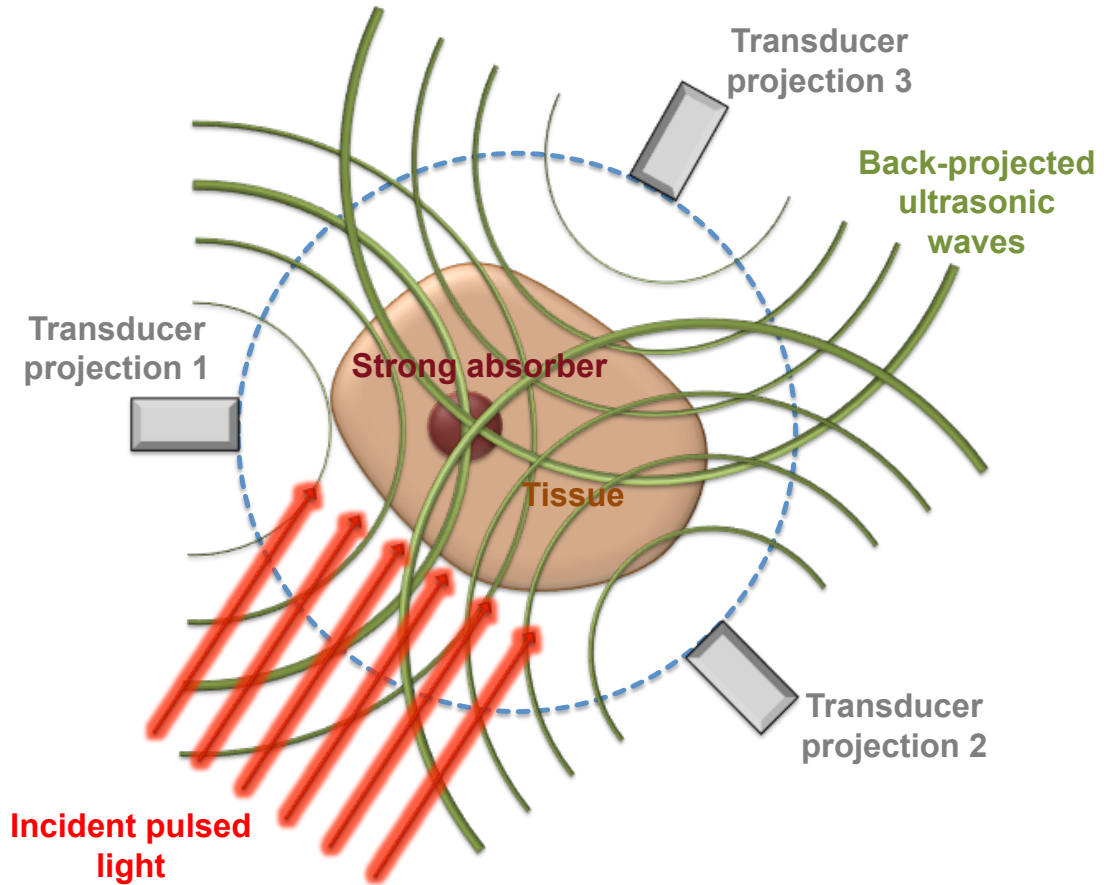
Figure 2.7: Back-projection principle. The transducer(s) acquire time-dependent optoacoustic signals around the object at different positions (projections). The signals are "back-projected" in spherical surfaces shown in green with radii r=ct in order to create an image.

Poisson's solution of Eq. (2.19) for a uniform non-attenuating acoustic medium can be expressed as [13]

$$p(r,t) = \frac{\Gamma}{4\pi c}\frac{\partial}{\partial t}\int\limits_{S'(t)} \frac{H(r')}{|r - r'|}\,d\,S'(t),$$

(2.20)

where $S'(t)$ is a time-dependent spherical surface for which $|r - r'| = ct$. Eq. (2.20) establishes that the acoustic pressure signal $p(r,t)$ at a certain point r is

proportional to the integral of the optical absorption $H(r')$ at locations r' along a spherical surface centered at r and with radius ct. Thereby, a reconstruction strategy consists in "back-projecting" the measured signals at r and t to the points where such signal could have been generated [27], and subsequently add the contribution of all measuring positions (Figure 2.7). This concept is exploited in back-projection reconstruction. For example, in a universal back-projection algorithm for homogeneous acoustic media, the reconstructed optical absorption field $H_r(r')$ is given by [28]

$$H_r(r') = \frac{1}{\Gamma} \int_\Omega \frac{d\Omega}{\Omega} \left[2p(r,t) - 2t \frac{\partial p(r,t)}{\partial t} \right]\Bigg|_{t=\frac{|r-r'|}{c}}.$$

(2.21)

The last equation is derived for a surface S surrounding r, i.e., the solid angle $\Omega = 4\pi$ (Figure 2.8). The differential $d\Omega$ is the solid angle for an element dS and acts as a weighting factor in the reconstruction. In practical cases, the number of measuring positions is finite. In this case, the reconstruction can be done with a simplified discretization of Eq. (2.21), where the constant terms are not included for the sake of simplicity, as [30]

$$H_r(r'_j) = \sum_i \left[p(r_i, t_{ij}) - t_{ij} \frac{\partial p(r_i, t_{ij})}{\partial t} \right],$$

(2.22)

being r'_j the position of the j-th voxel of the reconstructed region of interest (ROI), r_i the position of the i-th transducer and $t = |r - r'|/c$. If quantitative

images are required, the constants that have been omitted in Eq. (2.22) need to be considered.

There are different optoacoustic systems for which a two-dimensional geometry can be assumed. For example, if a thin section of the tissue is illuminated, the optoacoustic waves are only created in this slice of the sample [31,32]. Due to scattering of light in deep tissue, the light beam is broadened and diffused, making this approach not practical. In this case, cylindrically-focused transducers, can be used to provide only sensitivity in a cross-sectional plane, so that the two dimensional reduction is also applicable [33]. Eq. (2.22) can also be applicable in a two dimensional case, being computationally easy to implement and very fast. However, it is not a quantitative method and produces artifacts, e.g., streaking-type artifacts due to the limited number of projections and negative values in the reconstructed absorption [34]. Also, the shape and size of the transducer is not taken into account, i.e., point-detectors are assumed, which may also lead to artifacts in many cases [35,36].
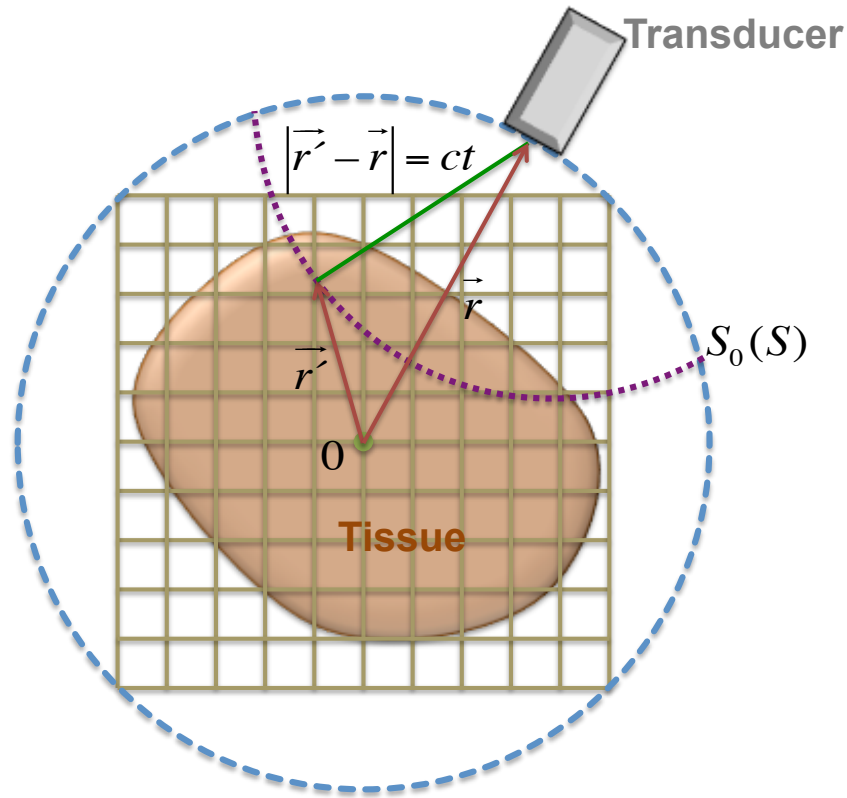
Figure 2.8: Reconstruction in 2-D Back-projection. A cross-sectional view of the sample is displayed with a circular scanning geometry. The image is created after projecting the signals from all the detection angles into a grid with a distance=ct and summing them up.

2.5.2 Model-based reconstruction

A different and more flexible reconstruction procedure developed at our institute is based on a discrete approximation of the optoacoustic forward model, where the detected acoustic signals are modeled as linear function of the optical absorption. With this linear model, the optical absorption solution can be solved at a grid of points after a least-squares minimization of the difference between the acoustic pressure measured at a number of projections and time points and the theoretically calculated pressure [37].

For cross-sectional reconstruction, the Poisson-type integral in Eq. (2.20) in arbitrary units is simplified to two dimensions as [37]

$$p(r,t) = \frac{\partial}{\partial t} \int_{L'(t)} \frac{H_{\vec{r}}(r')}{|r - r'|} \, d \, L'(t),$$

(2.23)

where $L'(t)$ represents a circumference for which $|r - r'| = ct$. Eq. (2.23) represents the pressure wave (in arbitrary units) detected at a distance r and a time t, i.e., the pressure is calculated as the derivative of a line integral of the optical absorption for points with a fixed radius ct to the detector. The model-based reconstruction procedure described in this section is based on a discretization and inversion of this formula.

In a first stage, a numerical approximation for the time derivative in Eq. (2.23) is done so that

$$p(r,t) \approx \frac{I(t + \Delta t) - I(t - \Delta t)}{2\Delta t},$$

(2.24)

where

$$I(t) = \int_{L'(t)} \frac{H_{\vec{r}}(r')}{|r - r'|} \, d \, L'(t).$$

(2.25)

The integral in Eq. (2.25) is discretized by approximating of the curve $L'(t)$ with a number of M points corresponding to the intersection of straight lines with equally-spaced angular position from the transducer position [38]. The total angle

covered by these lines is selected so they fill the imaging grid i.e., the value of α is calculated as [38]

$$\alpha = 2arcsin\left(\frac{\sqrt{2}(n+1)\Delta xy}{2R}\right),$$

(2.26)

where n is the number of pixels of the ROI in the horizontal and vertical directions, Δxy is the size of each pixel and R is the distance from the transducer to the center of the ROI.
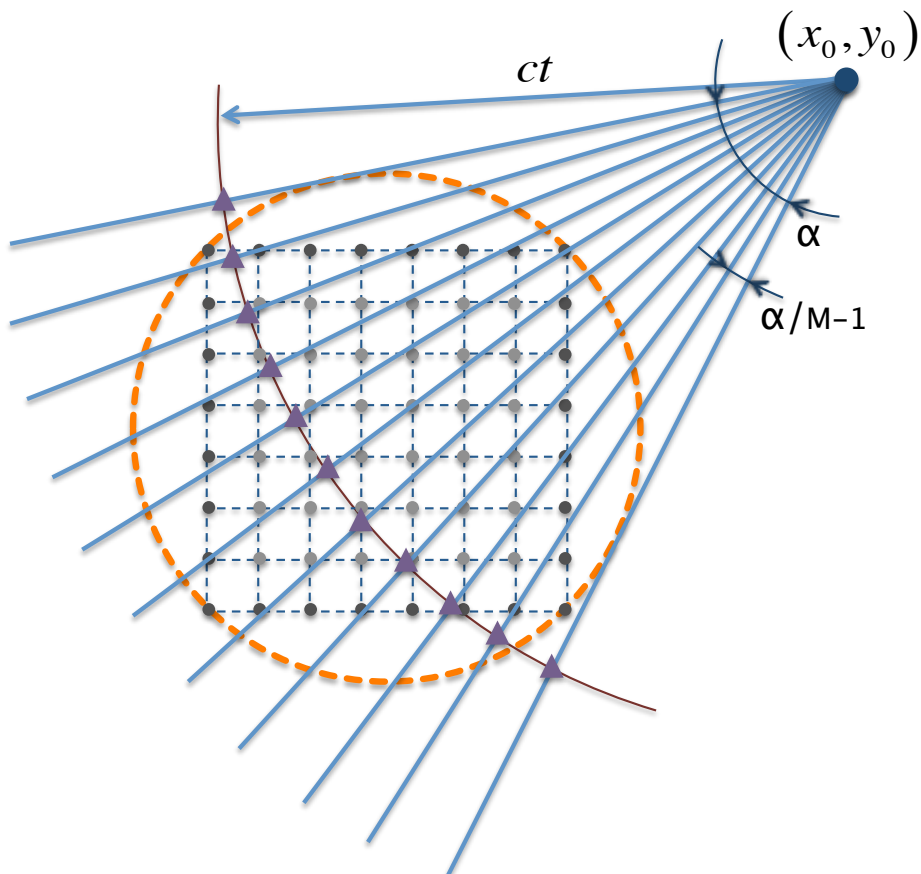
Figure 2.9: Discretization of the optoacoustic forward model in 2-D. The curve $L'(t)$ is estimated by M points indicated as triangles in the figure.

The integral $I(t)$ is then estimated from the M points of the curve $L'(t)$ with locations r'_i (triangles in Figure 2.9) as

$$I(t) \approx \frac{1}{2} \sum_{l=1}^{M-1} \left[\frac{H(r'_l)}{|r - r'_l|} + \frac{H_r(r'_{l+1})}{|r - r'_{l+1}|} \right] d_{l,l+1},$$

(2.27)

or alternatively

$$I(t) \approx \frac{1}{2} \sum_{l=1}^{M} \frac{H(r'_l)}{|r - r'_l|} \left(d_{l-1,l} + d_{l,l+1} \right),$$

(2.28)

where $d_{0,1} = d_{M,M+1} = 0$. $H(r'_l)$ is calculated by interpolation of the pixels in the ROI. After combining Eqs. (2.24) and (2.28), the acoustic pressure $p(r_i, t_j)$ at position r_i and time t_j can be estimated as a linear combination of the absorbed energy at the position r'_k of the pixels in the ROI, i.e.,

$$p(r_i, t_j) \approx \sum_{k=1}^{N} a_k^{ij} H(r'_k),$$

(2.29)

being $N = nn$ is the total number of pixels in the grid. The values a_k^{ij} can be calculated with different methods of interpolation.

The discretization of the forward model in a medium with a non-uniform speed of sound is also possible. In soft biological tissues, the speed of sound can vary between $\pm10\%$ compare to the one in water [39]. In this case, the M points of the integration curve are found with the line integral of the inverse of the speed of sound.

The pressure $p(r_i, t_j)$ in Eq. (2.29) is estimated at different P positions and I time instants, so that a system of linear equations is built, which is expressed in a matrix form as

$$P = AH.$$

(2.30)

Eq. (2.30) corresponds to the theoretical acoustic pressure of a group of transducer positions and time points. The model matrix A depends only on the geometry of the optoacoustic set-up and the speed of sound distribution. H is the energy absorption in the reconstruction ROI expressed in a vector form, which is calculated by minimizing the mean square difference between the theoretical pressure and the measured pressure p_m as

$$H_{sol} = argmin_H\|p_m - AH\|^2.$$

(2.31)

The solution to Eq. (2.31) can be calculated by means of the Paige-Saunders iterative least-square QR decomposition (LSQR) algorithm [40], where the sparsity of the model matrix is advantageously used to achieve a faster reconstruction [37].

The model-based inversion procedure renders more quantitative optoacoustic images that those obtained with back-projection reconstruction. Nevertheless,

the computational requirements are much higher. Generally, the model matrix A in Eq. (2.30) needs to be calculated several times to calibrate the reconstruction parameters. However, once the calibration is done, A can be stored for a setup with fixed illumination and the distance between transducers and samples [41], so that the inversion procedure is fast.

2.5.2.1 Thikonov regularization

It has been experimentally demonstrated that representative tomographic reconstructions can be obtained with Eq. (2.31), i.e., with no additional regularization of the inversion, when the signals are recorded at locations covering 360^0 degrees with respect to the sample (full-view acquisition). However, in limited-view cases, it is useful to regularize the inversion process. Tikhonov regularization is probably the most common method for ill-posed problems. In this case, the reconstruction of the optical absorption is done by modifying Eq. (2.31) as [42]

$$H_{sol} = argmin_H \|p_m - AH\|^2 + \lambda^2 \|LH\|^2,$$

(2.32)

being λ the regularization parameter, which controls the effect of the penalty term and L is the Tikhonov matrix. For the reconstructions done in this work, the matrix L was chosen to be the identity matrix.

2.5.2.2 Positive constrain reconstruction

Although the model-based algorithm as described above is a suitable reconstruction method to estimate the optical absorption in OAT, the rendered images are still affected by negative values without any physical value. In this

case, it is useful to solve the inversion problem with a positive constrain to H, i.e., Eq. (2.31) is modified as

$$H_{sol} = argmin_{H \geq 0} \|p_m - AH\|^2$$

(2.33)

As opposed to the unconstraint formula in Eq. (2.31), which can be inverted directly, Eq. (2.33) can only solved in an iterative manner.

2.5.2.3 Weighted model-based

As mentioned above, model-based reconstruction algorithms are efficient in removing common artifacts related to the use of back-projection methods. However, artifacts associated to internal reflections and scattering of the acoustic waves in strongly mismatched tissues may appear. Weighted model-based refers to an algorithm based in weighting the tomographic contribution of each of the measured signals at a given detector position and time with the probability that the signal corresponds to a scattered or reflected wave [43]. This reconstruction method is very useful in the presence of organs or tissues with high acoustic impedance variations such as bones, lungs, etc.

The forward model in Eq. (2.30) assumes the straight propagation of the acoustic waves with a constant speed of sound between emission and reception. Nevertheless, there is a probability that the signals are reflected or scattered during the propagation before reaching the transducer. To calculate this probability, an area A with all the possible optical absorbers ($H(r')\neq0$), acoustic reflectors and acoustic scatterers is considered (Figure 2.10). The probability of

detecting a reflected or scattered wave ($P_r^i(t_j)$), assuming unit amplitude, at the ith location of the transducer r_i and at time t_j can be expressed as [30] with

$$P_r^i(t_j) = \int_{A_{ij}} P_r^i(t_j|r')f_E(r')dr'.$$

<div align="right">(2.34)</div>

$f_E(r')$ represents the probability density function in a location where a diferential energy is absorbed and $P_r^i(t_j|\mathbf{r}')$ the conditional probability that a reflected or scattered acoustic wave with unitary amplitude is received by the transducer at an instant t_j, assuming that all the energy is absorbed at r'. All the points r' in which a reflected or scattered wave may have been generated and detected at the transducer located in r_i at time t_j, are inside the area A_{ij}. $P_{r,dist}^i(t_j|r')$ is the probability that the acoustic wave (measured with the ith transducer at instant t_j) is distorted by a reflected or scattered wave. It was showed in [30] that $P_r^i(t_j)$ can be calculated as

$$P_r^i(t_j) = min\left[1, \omega\left(\frac{A_{ij}}{A}\right)\right].$$

<div align="right">(2.35)</div>

Here ω is a weighting factor to be calculated heuristically. The probability $P_d^i(t_j)$ that the wave is not affected by reflection or scattering by the i-th transducer and time t_j is then set as

$$P_d^i(t_j) = 1 - P_{r,dist}^i(t_j).$$

<div align="right">(2.36)</div>
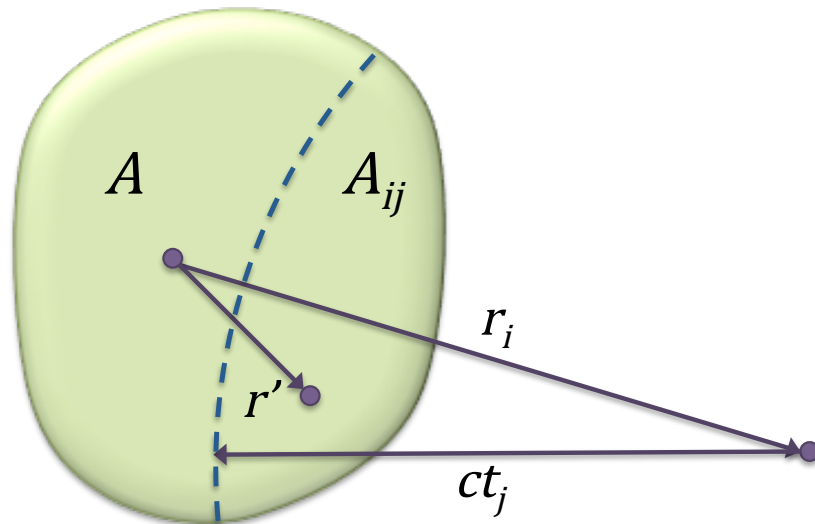
Figure 2.10: Statistical weighting algorithm. All the optical absorbers, potential acoustic reflectors and possible scatterers are inside the area A. All the points r' where a reflected or scattered wave may have been produced and detected by the transducer placed in the position ri, are in the area Aij.

The statistical approach improves the quality of the reconstruction method in the presence of acoustic reflections or scattering, giving more preference to optoacoustic signals with direct wave propagation and less weight to the reflected or scattered ones in the reconstruction.

The adjustment in Eq. (2.29) includes weighting each of the equations with the probability that each of the signals (related to the several time points and projections) is affected by reflection or scattering events. As a result, signals with a direct path between emission and reception are weighted higher in the reconstructions. Mathematically, the system of linear equations in Eq. (2.29) is modified as

$$P_d^i(t_j)p(r_i, t_j) = P_d^i(t_j) \sum_{k=1}^{N} a_k^{ij} H(r'_k).$$

<div align="right">

(2.37)

</div>

Therefore, the resulting equation is expressed as

$$Wp_m = WAH,$$

<div align="right">

(2.38)

</div>

so that the reconstruction is made with the mean square difference minimization problem as

$$H_{sol} = argmin_H \|Wp_m - WAH\|^2.$$

<div align="right">

(2.39)

</div>

2.5.2.4 Model-based reconstruction considering the shape of the transducer

Cylindrically-focused transducers are commonly used since the optoacoustic problem can be efficiently reduced to 2-D by selectively acquiring signals produced in the imaging plane. Although as a first order approximation this type of transducer can be modeled as a point detector, sophisticated reconstruction methods have been explored, taking into account the geometrical characteristics of the transducers [36,44,45]. The model matrix A in Eq. (2.30) assumes that the optoacoustic signal was recorded at a certain position (point detector) when performing the image reconstruction of the optical absorbance. This hypothesis represents a simplification. In actual scenarios the optoacoutic pressure is

spatially averaged over the active area of the transducer so that the collected signal can be approximated as

$$P_{det}(x_c, t) \approx \iint_S P(x', t) dx',$$

(2.40)

where x_c is the center of the transducer and S is the detection surface. Therefore, a new model matrix representing the finite size of the detector needs to be calculated. There are different approaches to model the shape of a transducer. For example, the pressure field could be convolved at different measuring projections with the spatially dependent signal impulse response (SIR) of the element. Alternatively, the transducer surface can be discretized by a number of surface elements with the optoacoustic signal superimposed on to each of these components. The SIR of a finite length line detector can be estimated analytically using the first method [35]. Afterwards, one cylindrically-focused transducer could be modeled as a number of lines having each a different impulse response. In the next formula, the estimated total response of the transducer is expressed as

$$h_{det}(x_c, x', t) \approx \sum_{i=1}^{n} h(x_i, x', t),$$

(2.41)

where $h(x_i, x', t)$ is the impulse response of each of the lines (centered at x_i) and x_c is the center of the detector. The numerical convolution between h_{det} and the model-matrix A, creates the new model-matrix A_{det} so that the theoretical pressure can be calculated as

$$P_{det} = A_{det}H'.$$

<div align="right">(2.42)</div>

In this case, the number of lines to approximate the transducer could be much lower than the number of points in the second method mentioned before. The cylindrically-focused transducers could also be estimated as single lines due to the good performance of the detector rejecting out-of-plane signals in a 2-D imaging plane approach. In this way, the computing times are considerably faster than having a transducer shape modeled with several lines.

The reconstruction of the optical absorbance can be calculated with the LSQR algorithm in the same way as in the previously mentioned model-based imaging methods.

2.5.2.5 Model-based reconstruction with tomographic symmetries

One of the problems when performing optoacoustic reconstructions with the model-based approaches described above is the memory requirements needed to store large model matrices, even when the amount of non-zero values is large (sparse matrices). This problem can be overtaken by considering the symmetries in certain acquisition geometries [46,47].

The method presented in this section reduces the computation time of model-based procedures. By using the characteristic geometrical symmetries in most of the optoacoustic tomographic systems, an efficient model matrix can be calculated leading to less memory requirements and faster calculation periods. This algorithm discretizes the time-domain optoacoustic forward model in a polar grid and is applicable in full-view and limited-view imaging situations [48].

The method used to build the model matrix A in a polar grid is described herein. In a tomographic scan, the signals are typically acquired with equally

projections angles $(\phi = 1 \ldots N_\phi)$ at positions x', regularly instants t_τ $(\tau = 1 \ldots N_t)$ and at a constant radius. For a two-dimensional system, Eq. (2.25) is applicable. In order to discretize this equation, a polar grid around the imaged sample is described with equidistant circles for the radial direction $(r = 1 \ldots N_\varphi)$ and angles $(\varphi = 1 \ldots N_\varphi)$ for the azimuthal direction, matching each of the transducer positions. In Eq. (2.25), $L(t)$ is an arc with center in x' and radius ct, which can be approximated as a number of regularly distributed points N_{int} (red diamonds in Figure 2.11).
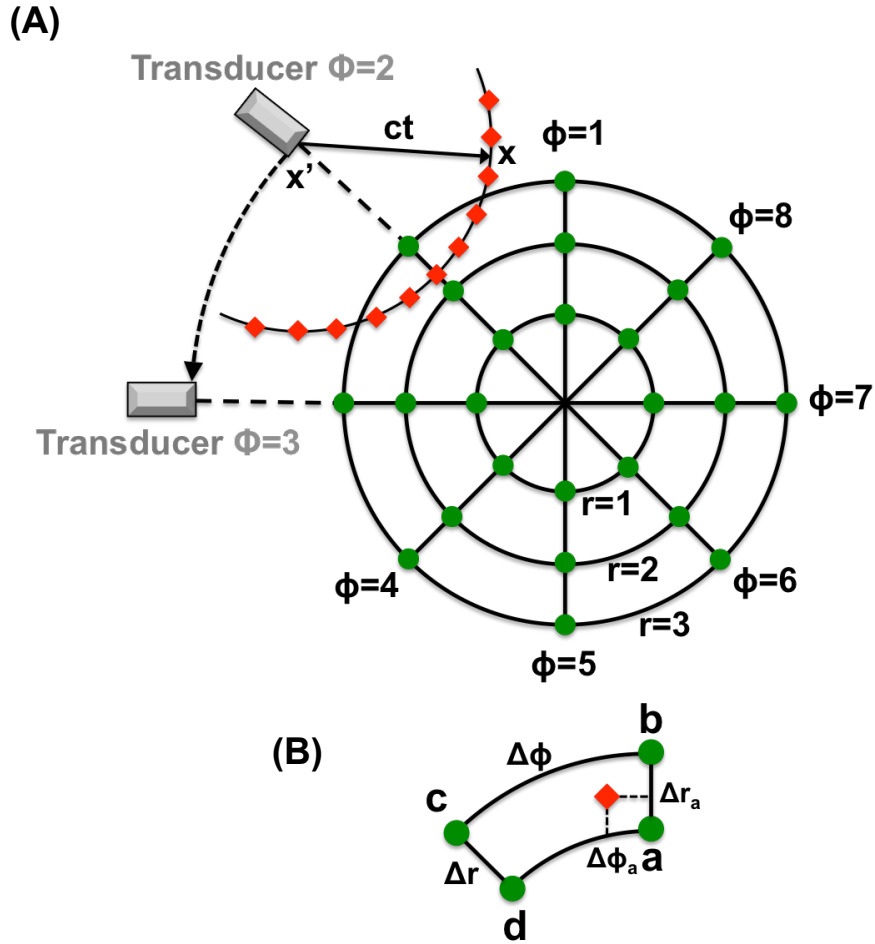
Figure 2.11: Polar grid discretization. (A) Image discretization and detection pattern. The image grid is represented with green circles. The angles ϕ where the detection is done at a given location x' coincide with the angular discretization of the grid φ. The integration arc can be approximated by a certain number N_{int} of equally-spaced points (red diamonds). (B) Interpolation used to calculate the model-matrix A. The integrated pressure on a detector arc for a given point (red diamond) can be mapped in the grid in both spatial coordinates by interpolation with 4 neighboring points (green circles a-d).

Eq. (2.25) can then be discretized as

$$I(x',t) \approx \frac{1}{2} \sum_{s=1}^{N_{int}-1} \left[\frac{H(x_s)}{[x'-x_s]} + \frac{H(x_s+1)}{|x'-x_{s+1}|} \right] d_s.$$

<div align="right">(2.43)</div>

The optical energy $H(x_s)$ can be interpolated from the four neighboring points (a-d) from the grid as

$$H(x_s) = (1-\Delta r_a)(1-\Delta\varphi_a)H_a + \Delta r_a(1-\Delta\varphi_a)H_b + \Delta r_a\Delta\varphi_a H_c$$
$$+ (1-\Delta r_a)\Delta\varphi_a H_d,$$

<div align="right">(2.44)</div>

where Δr and $\Delta\varphi$ are the spacings of the grid in the radial and azimuthal directions, and $\Delta r_a = (r-r_a)/\Delta r$ and $\Delta\varphi_a = (\varphi-\varphi_a)/\Delta\varphi$. Combining Eqs. (2.24) and (2.43), the pressure at a projection x'_Φ and time t_τ is given as a function of the optical energy at the different points of the image grid like

$$p_{\Phi,\tau} = p(x'_\Phi, t_\tau) = \sum_{r,\varphi} A(x'_\Phi, t_\tau, r, \varphi) \cdot H(r, \varphi) = \sum_{r,\varphi} A_{\Phi,\tau,r,\varphi} \cdot H_{r,\varphi}.$$

<div align="right">(2.45)</div>

Eq. (2.45) represents a special expression of Eq. (2.30) with rotational invariance. However, in this case only a submatrix of $A = A_{\Phi,\tau,r,\varphi}$ corresponding to a projection needs to be saved and subsequently used for inversion. The rest of submatrices have the same redundant information due to the fact that they are just rotated versions of the first one. Thereby, model-based reconstruction in polar coordinates can be performed with less memory costs.

2.6 Multispectral unmixing

As mentioned before, MSOT explores the functional and molecular imaging capability within biological tissues by illuminating the sample with different wavelengths and recording the resulting generated signals. In this way, the different signatures of the intrinsic chromophores like oxygenated and deoxygenated hemoglobin and externally administered contrast agents in tissue can be analyzed, increasing the capacities of single wavelength imaging [49,50].

Unmixing algorithms allow estimating the different distribution of substances by accounting for their particular spectral absorbance. Unmixing is done by processing the set of images corresponding to different excitation optical wavelengths with different types of mathematical methods [23,51–53]. Below we explain the spectral fitting procedure [31], which is the particular mathematic method used in this work.

2.6.1 Spectral fitting

The most common method for spectral unmixing in MSOT is spectral fitting. Optoacoustic images represent the distribution of the optical absorbance energy $H(r)$ inside tissue. At one single illumination wavelength λ_i, different absorbing substances can contribute to the map of optical absorbance. For n contrast agents or components, $H(r, \lambda_i)$ in arbitrary units can be expressed as

$$H(r, \lambda_i) = U(r, \lambda_i)\epsilon_1(\lambda_i)c_1(r)+...+U(r, \lambda_i)\epsilon_n(\lambda_i)c_n(r),$$

(2.46)

being $U(r,\lambda_i)$ the light fluence and $\epsilon_j(\lambda_i)$ and $c_j(r)$ the molar extinction coefficient and concentration for the jth absorber respectively. A homogeneous Grüneisen parameter was assumed in this case.

For w acquisition wavelengths, Eq. (2.46) can be expressed in a matrix form for a given pixel p in the image as

$$H^p = \epsilon^p c^p,$$

(2.47)

where H^p represents a w-dimensional column vector containing the absorption $H(r_p,\lambda_i)$ for the different wavelengths, c^p is a q-dimensional column vector with all the concentrations $c_j(r_p)$ for the different absorbers and ϵ^p is a matrix with $m \times q$ dimensions and with elements

$$[\epsilon^p]_{i,j} = U(r_p,\lambda_i)\epsilon_j(\lambda_i).$$

(2.48)

If spatially independent light fluence is assumed for each of the wavelengths, Eq. (2.47) can be approximated as

$$H^p \approx \overline{U}(r_p)\epsilon c^p,$$

(2.49)

where $\overline{U}(r_p)$ symbolizes the average value of $U(r_p,\lambda_i)$ over the total number of wavelengths and $\boldsymbol{\epsilon}$ is a matrix with the elements $\epsilon(i,j) = \epsilon_j(\lambda_i)$. The last formula can be resolved for the concentrations with least squares minimization as

$$U(r_k)c_{sol}^p = argmin_c \left\| H_{exp}^p - \epsilon c^p \right\|^2.$$

H_{exp}^p represents the optical absorption reconstruction for the p-th pixel. In realistic scenarios, multispectral images further suffer from spatial light fluence variations that have to be taken into account for quantitative results. Eq. (2.50) can be expressed assuming constant light fluence, so that the concentration in arbitrary units is approximated as

$$c_{sol}^p = argmin_c \left\| H_{exp}^p - \epsilon c^p \right\|^2.$$

When all the pixels in the images are considered, Eq. (2.51) can be written as

$$C_{sol} = argmin_c \left\| H_{exp} - \epsilon C \right\|^2.$$

Eq. (2.52) can be solved with the pseudo-inverse of matrix ϵ, so that

$$C_{sol} = \epsilon^+ H_{exp}.$$

3 Study of optoacoustic signal efficiency with different probes

3.1 Introduction

As any other molecular imaging technology, MSOT relies on intrinsic or exogenous agents to deliver particular molecular information (Figure 3.1). Then, parallel to the improvements enabled with novel hardware designs, the election and development of new contrast agents is a key aspect for the practical applicability of this technique [54]. MSOT can potentially be used with a larger number of contrast agents compared with other optical imaging technologies that use mostly fluorescent molecules to produce suitable contrast. This is due to the fact, as already commented, that any substance absorbing light can generate spectrally-distinctive optoacoustic signals. As a result, chromophoric and fluorescent dyes, nobel metal and carbon nanoparticles and other absorbing constructs has been proposed as MSOT contrast agents [23,31,55–63].
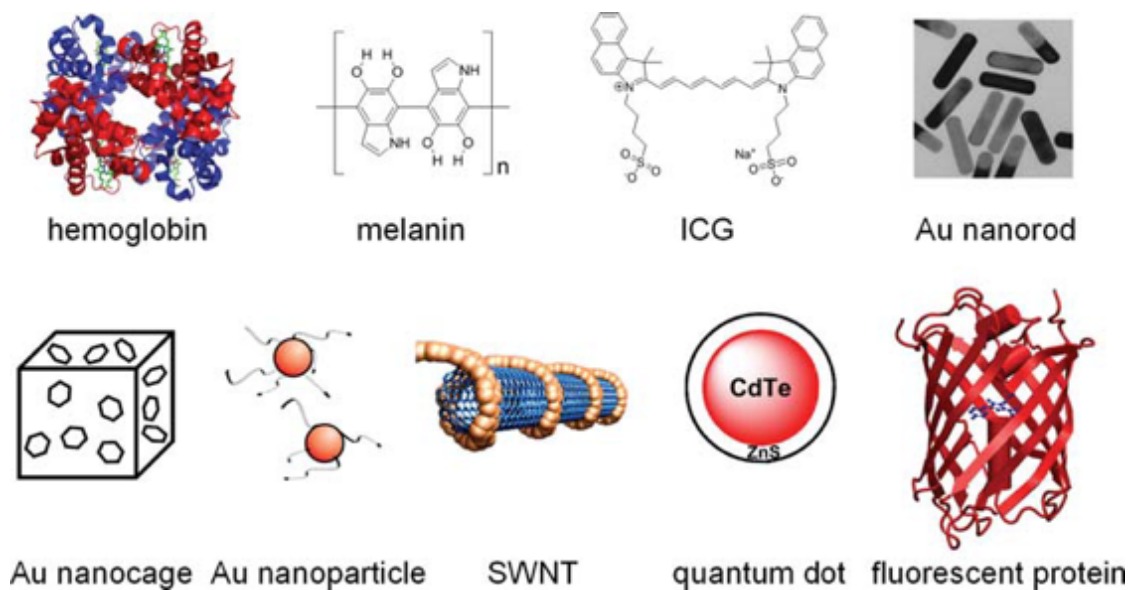
Figure 3.1: Some cromophores used in MSOT imaging. A variety of endogenous and exogenous contrast agents can be employed for different applications (image taken from [64]).

The selection of the optimal contrast agent to use depends on the target of the specific application. Some criteria to be considered in an imaging experiment are the optoacoustic signal efficiency, absorption spectrum, photostability, dimensions, chemical composition, ability to attach to targeting moieties and drugs, biotoxicity and dynamics of clearance from the organism [65]. Despite the fact that the size, shape and chemical composition are important factors regarding the toxicity of the probe, the amount of injected dose has also a significant role in the toxicity and crosstalk effects inside the body. Thereby, it is of high interest to select efficient probes capable of generating a strong optoacoustic signal with a relatively low dose. A probe with a high absorbance per concentration unit and a distinguishable spectrum from the background tissue absorption chromophores, like hemoglobin or melanin, is then a good candidate to be imaged with MSOT. On the other hand, the efficiency of a contrast agent in long imaging sessions with optical radiation can be reduced if they are not photostable. For example, fluorescent dyes often experience photobleaching

[66], whereas laser light can also produce deformation in the shape of plasmonic nanoparticles, which leads to changes in their absorption spectrum [67].

In this chapter, the efficiencies of different exogenous probes are analyzed in tissue phantoms measured in a small animal imaging system. Photobleaching effects due to continuous light exposure are also examined for different substances. Finally, a self-developed optoacoustic spectrometer is presented and used to characterize spectrally-dependent optoacoustic signals.

3.2 Optoacoustic efficiency

The optoacoustic efficiency of a probe is defined in this section. For a certain probe, the initial optoacoustic pressure excited at a given wavelength λ with a pulse duration satisfying thermal and acoustical confinement conditions can be approximated by a temporal Dirac delta as

$$p_0(\lambda) = \Gamma \mu_a(\lambda)\phi(\lambda),$$

(3.1)

where Γ is the Gruneisen parameter, $\mu_a(\lambda)$ the optical absorption of the probe and $\phi(\lambda)$ the light fluence. The wavelength-dependent optical absorption $\mu_a(\lambda)$ of a photo-absorbing agent is given by

$$\mu_a(\lambda) = \varepsilon(\lambda)C \ln(10) \approx 2.3\varepsilon(\lambda)C,$$

(3.2)

where C is the molar concentration and $\varepsilon(\lambda)$ is the molar extinction coefficient [10]. So we define the wavelength-dependent molar optoacoustic efficiency of the agent $\eta_{OA}(\lambda)$ as the signal generated by unit concentration and fluence, i.e.,

$$p_0(\lambda) = \eta_{OA}(\lambda)C\phi(\lambda).$$

<div align="right">(3.3)</div>

The mass optoacoustic efficiency can be analogously defined considering the mass concentration instead. Efficient contrast agents are desired due to their ability to create strong optoacoustic responses in a relatively small concentration. Combining Eqs. (3.1), (3.2) and (3.3), the molar optoacoustic efficiency can be therefore expressed as

$$\eta_{OA}(\lambda) = 2.3\Gamma\varepsilon(\lambda).$$

<div align="right">(3.4)</div>

The optical absorption or absorbance $A(\lambda)$ can be estimated with a spectrophotometer. However, $\mu_a(\lambda)$ in Eq. (3.1) refers to the amount of absorbed optical energy transformed into heat, hence producing a temperature rise. Although most substances transform the absorbed light into heat, fluorescent dyes reemit part of this energy, which does not contribute to the generation of optoacoustic signals. Assuming a sample with insignificant light scattering, the absorbance as measured in the spectrophotometer represents the non-transmitted energy when light pass throw it. Therefore, the percentage of energy transformed into heat is assumed to be the one not reemitted as fluorescence, so $\mu_a(\lambda)$ is related to $A(\lambda)$ as

$$\mu_a(\lambda) = (1 - \Phi)A(\lambda)ln(10) \approx (1 - \Phi)2.3A(\lambda),$$

<div align="right">

(3.5)

</div>

where Φ refers to the quantum yield of the contrast agent and the term $ln(10)$ is implicit in the definition of OD.

3.3 Probes preparation

Several contrast agents like fluorescent probes, nanoparticles, chromophoric dyes and substrates were used to increase the unspecific and targeted optoacoustic responses in tissue. The efficiencies of usual red and near-infrared Alexa Fluor fluorescent dyes (Invitrogen, Carlsbad, CA) and indocyanine green (ICG) (Pulsion Medical Systems, Munich, Germany) were studied. Also gold nanorods (AuNR) with peak extinction in the near-infrared spectrum (Nanopartz, Loveland, CO) were analyzed.

For each probe, different concentrations were prepared by dilution in distilled water. The optical absorption peaks as measured with a spectrophotometer (USB4000, Ocean Optics, Dunedin, FL) ranged from 2 to 0.1 OD.

A scattering agar phantom containing the contrast agents was used to measure them in a small-animal imaging system. Specifically, two straws each with 3 mm diameter were embedded in the phantom and placed at symmetrical positions with respect to the Z-axis in the system. One of the straws contains the probe to be characterized and the other one is filled with a known concentration of black India ink (Higgins, Illinois, USA) as a reference. The phantom in the small-animal imaging system is shown in Figure 3.2.

3.4 Experimental system and signal processing

A macroscopic MSOT small-animal imaging system was used to measure the efficiency of probes embedded in tissue phantoms [68] (Figure 3.2 A). The optoacoustic scanner provides parallel detection of optoacoustic signals covering 172° with a curved array of 64 cylindrically-focused ultrasonic transducers as shown in Figure 3.2. The transducer elements have a central frequency of 5 Mhz (Imasonic SaS, Voray, France). An optical parametric oscillator (OPO)-based laser (Phocus, Opotek Incorporated, Carsbad, California) provides nanosecond duration pulses at tunable optical wavelengths. The beam is guided through a silica fused-end fiber bundle (PowerLightGuide, CeramOptec GmbH, Bonn Germany) consisting of 630 fibers divided into 10 arms. The laser was tuned between 690 and 900 nm with a 10 nm step. The corresponding optoacoustic signals were acquired with a sampling frequency of 40 megasamples per second and 20 averages, giving an approximate acquisition time of 1.5 minutes per multispectral dataset.

The acquired optoacoustic signals were first band-passed filtered between 0.1 and 7 MHz. Tomographic two-dimensional slices of the phantoms were reconstructed with a time-domain model-based algorithm by using Tikhonov-based regularization in the inversion [42] (Figure 3.2 B). The initial optoacoustic pressure in each of the two probes (absorber and reference ink) was calculated with a ROI defined in each of the straws. The light fluence $\phi(\lambda)$ and Grueneisen parameter Γ were considered to be the same within both straws. By considering Eq. (3.1), the optical absorption coefficient of the contrast agent was calculated as a function of the absorption coefficient of the ink reference as

$$\mu_{a,p}(\lambda) = \frac{p_{0,p}(\lambda)}{p_{0,ink}(\lambda)} \mu_{a,ink}(\lambda),$$

<div align="right">(3.6)</div>

where $p_{0,p}(\lambda)$ and $p_{0,ink}(\lambda)$ are the reconstructed image values for the contrast agent and ink respectively. It was assumed that ink is a perfect absorber with an efficiency of 100 % and converts all the absorbed energy into heat. It was also hypothesized that the spectrum of the optoacoustic signal created by ink was the same that the OD measured with the spectrometer, i.e., $\mu_{a,ink} = 2.3\, A(\lambda)$. Then, the relative efficiency of different probes was estimated by comparing the respective optical absorption coefficients for known concentrations.
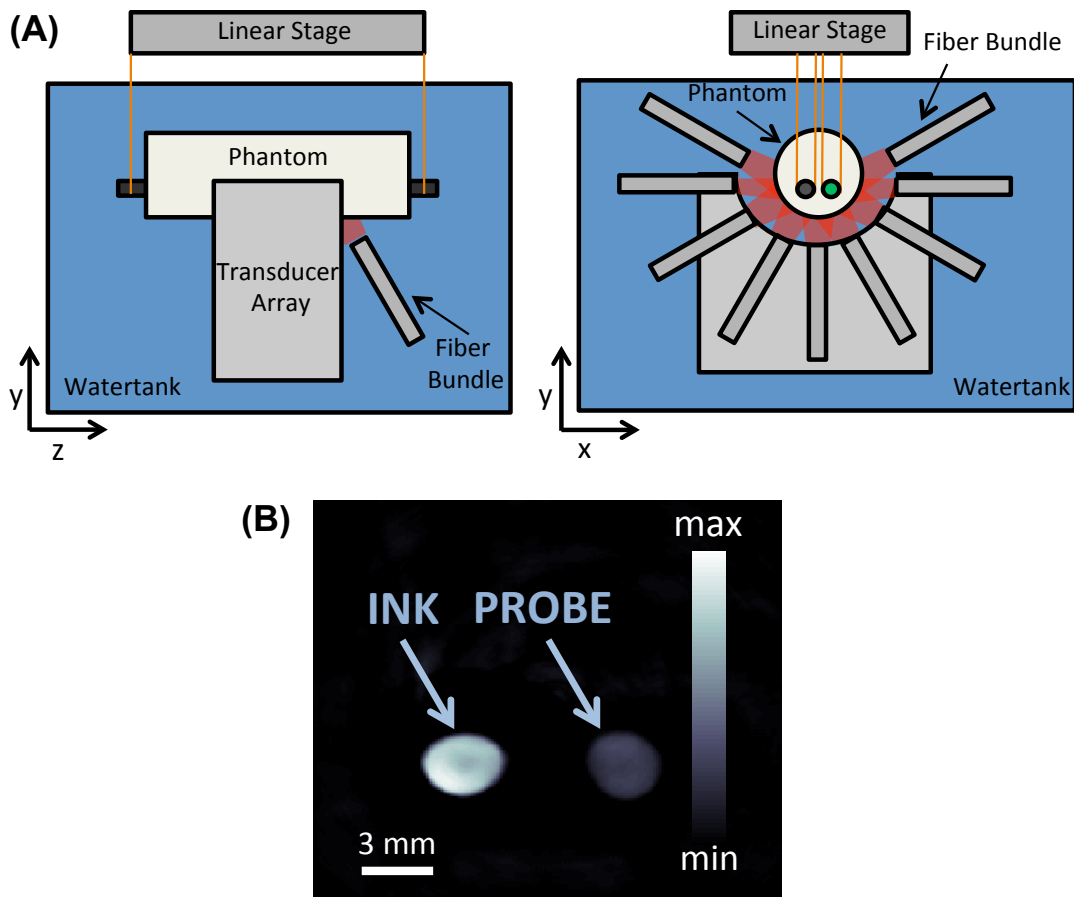
Figure 3.2: Macroscopic MSOT system. (A) Lateral view and frontal view of the system. The phantom with the two straws is placed in the center of the transducer array with linear stages and it is illuminated with the arms of the fiber bundle. (B) Optoacoustic model-based reconstruction of the two straws including ink as a reference and AF750 with 2 OD at the peak of the spectrum.

Extended exposure to optical radiation can lead to a decrease of the extinction cross-section of the probe, i.e., its absorption and/or fluorescence efficiency, via a chemical process known as photobleaching. In order to study these effects, samples of ICG and AF750 with 2 OD at the spectrometer peak were embedded in the phantom and imaged in the MSOT system. As mentioned before, each multispectral scan takes approximately 1.5 minutes, while the exposure was

maintained constant during approximately 30 minutes, corresponding to a total of 20 datasets.

3.5 Results

Figure 3.3 displays the spectra of the optical absorption coefficient for AF750 as measured with the MSOT system for 750 to 900 nm illumination wavelengths. The optoacoustic responses of AF750 with different concentrations, ranging from 8.3 to 0.42 µM (2-0.1 ODs), were estimated from the reconstructed images of the phantoms. The respective optical absorption coefficients were calculated according to Eq. (3.6) and are displayed in Figure 3.3 A. The equivalent OD spectra measured with the spectrophotometer are shown in Figure 3.3 B. The peak wavelength and the spectra shape for the curves in Figure 3.3 A and 3.3 B are very similar. Figure 3.3 C plots the optoacoustic value for the peak absorption wavelength (750nm) as a function of the corresponding OD, which presents the expected linear dependence as indicated by the high value of the R^2 parameter when fitting the points to a line. The experiments with the other probes led to similar results.
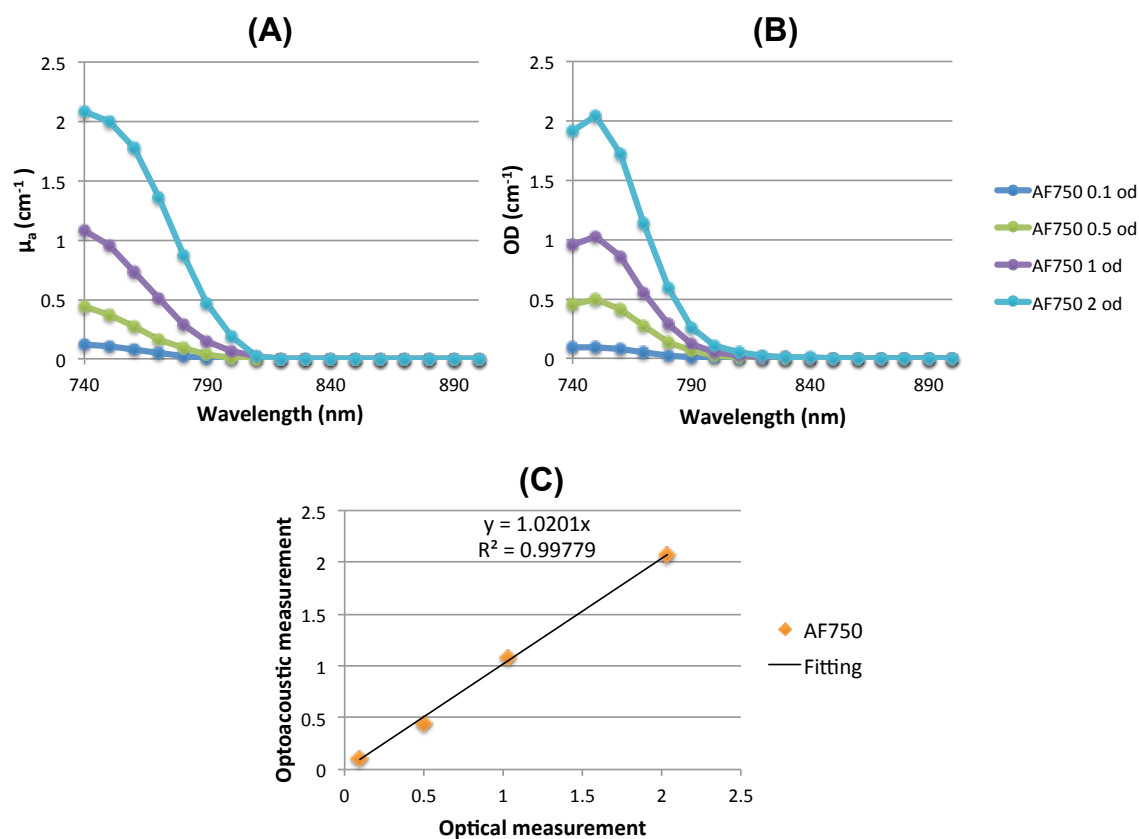
Figure 3.3: Optoacoustic and optical measurement relation for AF50. (A) Optical absorption coefficient calculated with the MSOT system as a function of the illumination wavelength. (B) OD measured with the spectrometer as a function of illumination wavelength. (C) Optioacoustic results as a function of the optical measurements at 750 nm wavelength.

The constituent probe molecules become excited due to laser light. The electrons return from the excited state to the ground state via the radiative relaxation processes fluorescence and phosphorescence or by radiationless relaxation. Radiationless relaxation processes create local heating of the medium, associated to the pressure waves through the sample in the optoacoustic principle [69,70]. Therefore in a fluorescent dye, the quantum yield is related to the slope of the linear relation between the optical and optoacoustic data. In particular, the slope *k* is proportional to *1-ϕ* as shown in Eq. (3.5). Therefore, fluorescent probes with a higher quantum yield are expected to produce weaker optoacoustic response in comparison with other probes having the same OD. The

value of k is proportional to the amplitude of the optoacoustic signal. Figure 3.4 displays the amplitudes of the optoacoustic signal generated by the different probes studied normalized to the signal amplitude generated by the most efficient probe. The quantum yields of fluorescent dyes are also presented in the figure. Generally, it is shown that the optoacoustic amplitude is proportional to 1-ϕ, although further tests with other dyes are needed to verify this hypothesis. AuNR presented the highest efficiency (last three contrast agents on the right).

Fluorescent Dyes	Optoacoustic Signal (normalized to the maximum)	1-ϕ
AF680	0.467	0.640
AF700	0.522	0.750
AF750	0.588	0.880
ICG	0.651	0.996
AF790	0.843	-
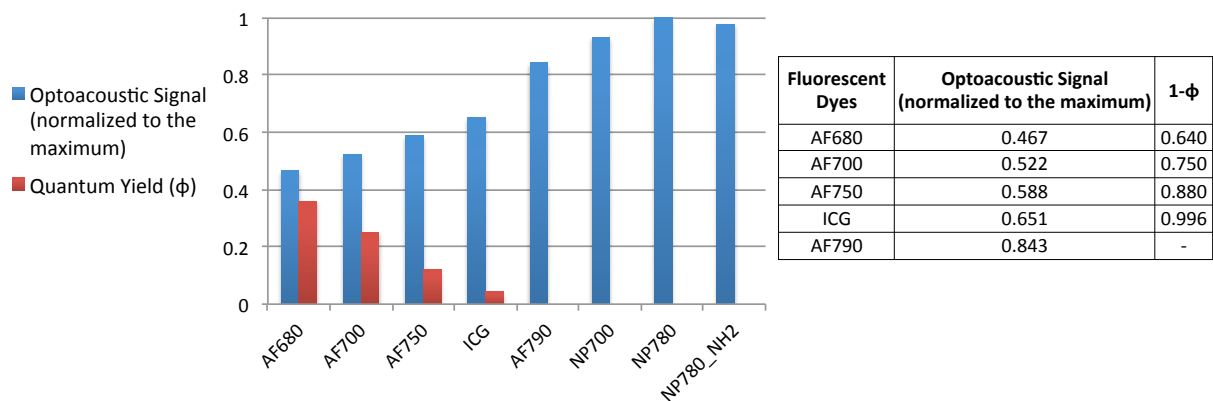
Figure 3.4: Normalized optoacoustic signal vs Quantum yield for different probes.

The bleaching effect in both probes (ICG and AF750) is displayed in Figure 3.5. Particularly, the peak of the optoacoustic spectra normalized to its maximum value is plotted as a function of time. These results show that the amplitude of the optoacoustic signal remained approximately constant AF750, i.e. no significant photobleaching effects were perceived. However, significant effects of photobleaching were evident in the case of ICG, for which the amplitude of the generated optoacoustic signals decayed 30 % after 30 minutes of exposure. ICG is a particularly suitable contrast agent that is approved by the U.S. Food and Drugs Administration (FDA) for human use in medical diagnostics since 1959 [71].

However, as shown herein, it has significant photochemical destruction and decay in optoacoustic efficacy over time.
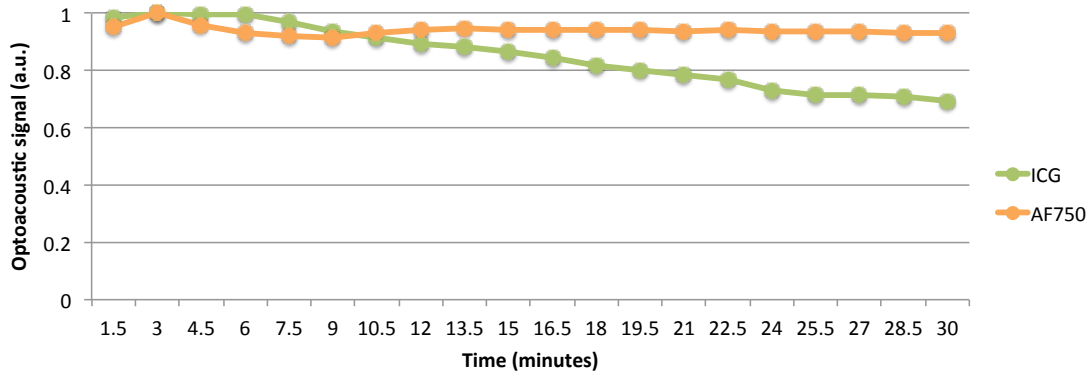
Figure 3.5: AF750 and ICG photobleaching over time.

3.6 Optoacoustic spectrometer

A spectrometer is one of the tools used to measure the absorbance along the electromagnetic spectrum of different intrinsic and extrinsic contrast agents. Whereas the optoacoustic spectrum can be measured with the small animal imaging system described above, a dedicated optoacoustic spectrometer is more convenient in many cases for the measurement of the optoacoustic spectrum of absorbing substances. In this section we describe an optoacoustic spectrometer developed in this Ph.D. project.

The layout of the optoacoustic spectrometer is depicted in Figure 3.6. Illumination is provided by means of an OPO laser (Phocus, Opotek Inc., Carlsbad, CA, USA) giving nanoseconds width pulses with a repetition rate of 10 Hz. The wavelength range of the laser is 700 to 900 nm. The beam was guided into a silica fused-end fiber bundle (CeramOptec GmbH, Bonn, Germany) with 640 fibers equally divided into 4 arms. Twp of these arms were fixed symmetrically in the

optoacoustic spectrometer and a 1 mm inner diameter Fine-Bore Polyethylene tube (Smiths Medical, London, England) containing the different samples was placed at the same vertical position. The laser power was monitored with a power meter FieldMaxII-Top (Coherent®, Santa Clara, CA, USA) at the output of one of the free fiber bundle arms. The optoacoustic signals originated at the tube were acquired with a cylindrically-focused transducer (PNDT V382, Panametrics NDT, Waltam, MA, USA) having a 3.5 MHz central frequency and a focal distance of 1.5 inches. The transducer is positioned at the top of the system.
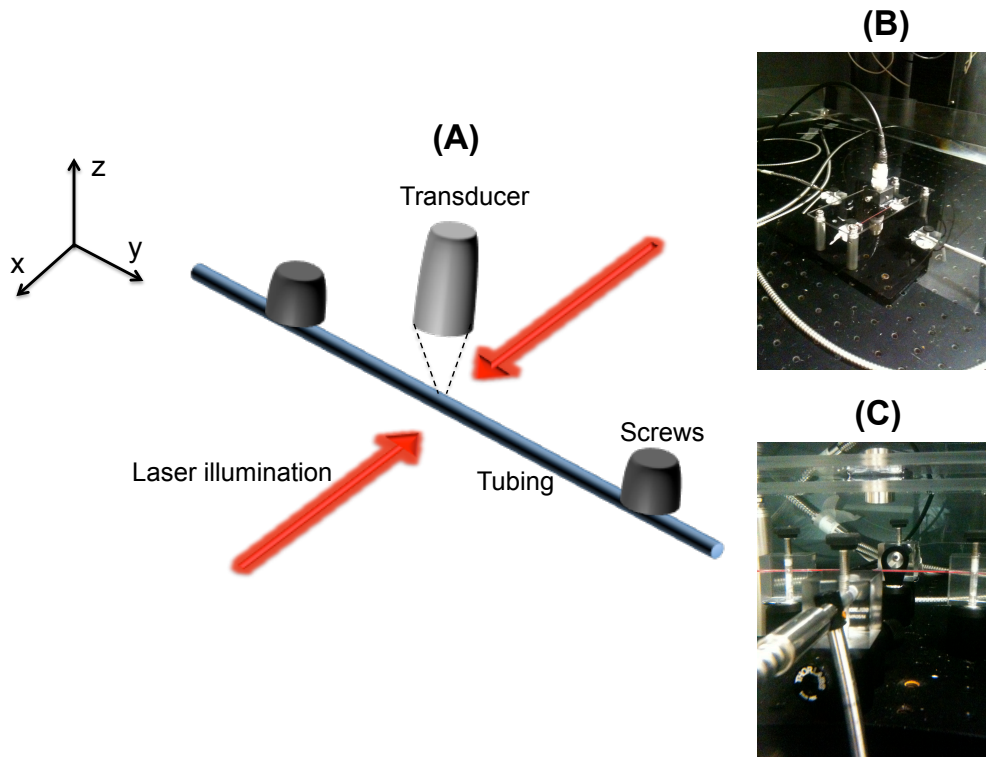
Figure 3.6: Optoacoustic spectrometer. (A) Setup diagram. The plastic tube with the probe is fixed with 2 screws and illuminated by two arms fiber bundle from opposite directions. The PNDT V382 transducer with 3.5 MHz central frequency received the optoacoustic signals coming from the irradiated tube. (B) Top view of the optoacoustic spectrometer system inside the water tank with blood as a probe to measure the absorbance spectrum at different wavelengths. (C) Front view of the optoacoustic spectrometer system in the same experiment as (B).

The performance of the optoacoustic spectrometer was first tested with black India ink (Higgins, Illinois, USA). The ink was diluted in distilled water at different concentrations and measured by using 750 nm as illumination wavelength. The signals were averaged 50 times. The OD of each of the samples was previously measured in the optical spectrophotometer. The maximum of the recorded time-resolved optoacoustic signal is plotted as a function of the OD in Figure 3.7. The trend line is also displayed with equation along with the R^2. As expected, there is a linear relationship between the readings in the optical and optoacoustic spectrometers.
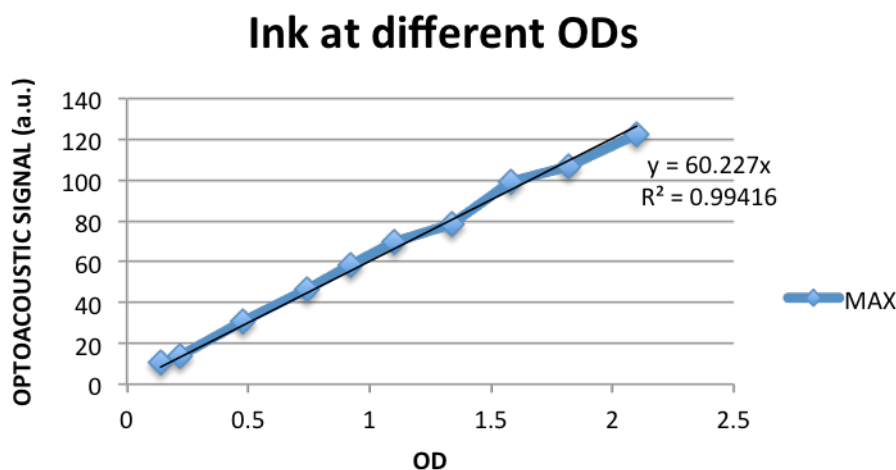
Figure 3.7: Ink measured at different ODs with the optoacoustic spectrometer. The optoacoustic signal is plotted as a function of the OD. The trendline and R2 parameter are also shown.

The optoacoustic spectrum of ink was also measured with the developed system. A tube containing 2.1 OD was scanned from 700 to 900 nm where 50 averages were done for each wavelength. The maximum of the optoacoustic signal for this tube is shown Figure 3.8 before and after correction with the laser power at the different wavelengths.

(A)

Ink 2.1 OD

OPTOACOUSTIC SIGNAL (a.u.)

140
120
100
80
60
40
20
0

700   750   800   850   900

WAVELENGTH (nm)

MAX

(B)

Laser power

ENERGY (mJ)

14
12
10
8
6
4
2
0

700   750   800   850   900

WAVELENGTH (nm)

ENERGY (mJ)

(C)

Ink 2.1 OD corrected

OPTOACOUSTIC SIGNAL (a.u.)

12
10
8
6
4
2
0

700   750   800   850   900

WAVELENGTH (nm)

MAX
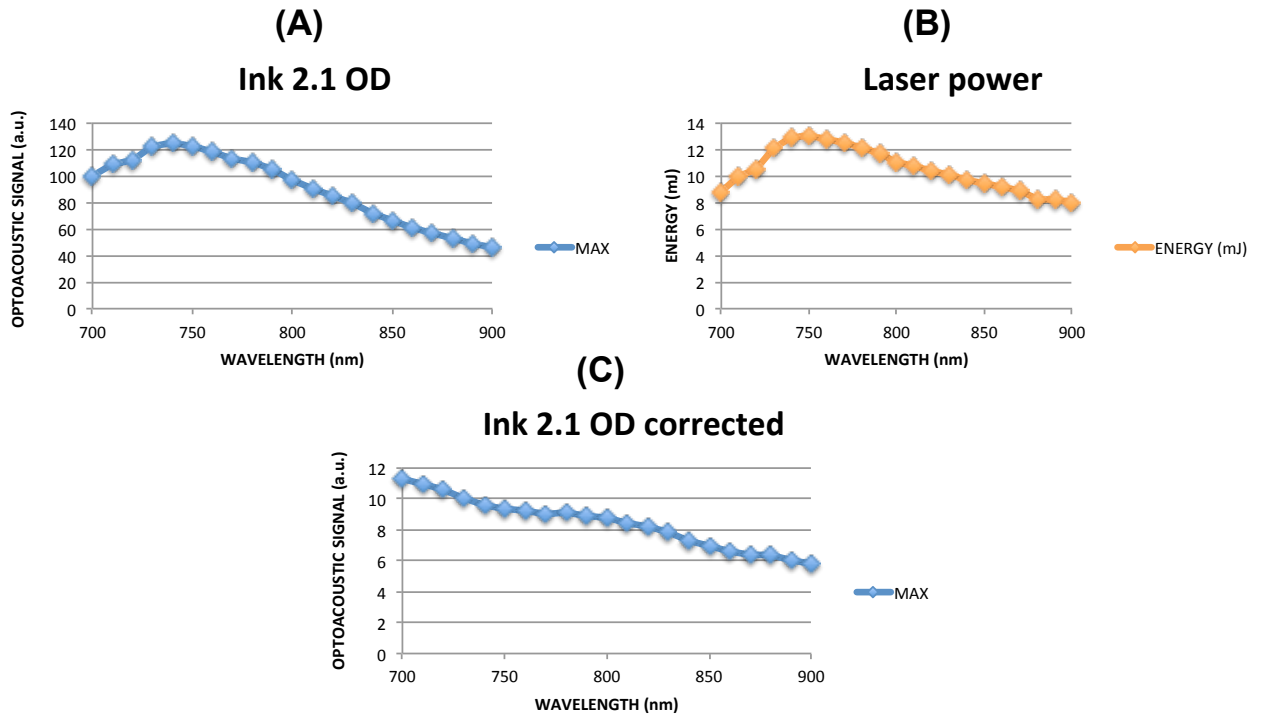
Figure 3.8: Multispectral optoacoustic spectrometer results with ink. (A) Maximum of the optoacoustic signal from ink before correction with the laser power. (B) Laser power measurements. (C) Ink corrected with the laser power (A divided B).

The potential of the optoacoustic spectrometer for actual biological experiments is showcased by characterizing blood at different oxygenation levels. Several tubes were prepared with New Zealand white rabbit blood. The oxygenation level was controlled by adding sodium hydrosulfite (Sigma-Aldrich, St. Louis, USA) in Dulbecco's Phosphate-Buffered Saline (DPBS, Gibco®|Life Technologies, Carsbad, CA, USA) as in [72] and checked by a gas analyzer. The tubes were scanned in the optoacoustic spectrometer from 720 to 870 nm with 50 averages for each wavelength. Spectral fitting was then performed using the maximum of the integral of the signal as measuring parameter in this case. A fewer number of wavelengths was employed in this case to prevent oxygenation during data acquisition. The oxygen saturation estimated with the optoacoustic

spectrometer was similar to the one obtained with the gas analyzer as shown in Figure 3.9.
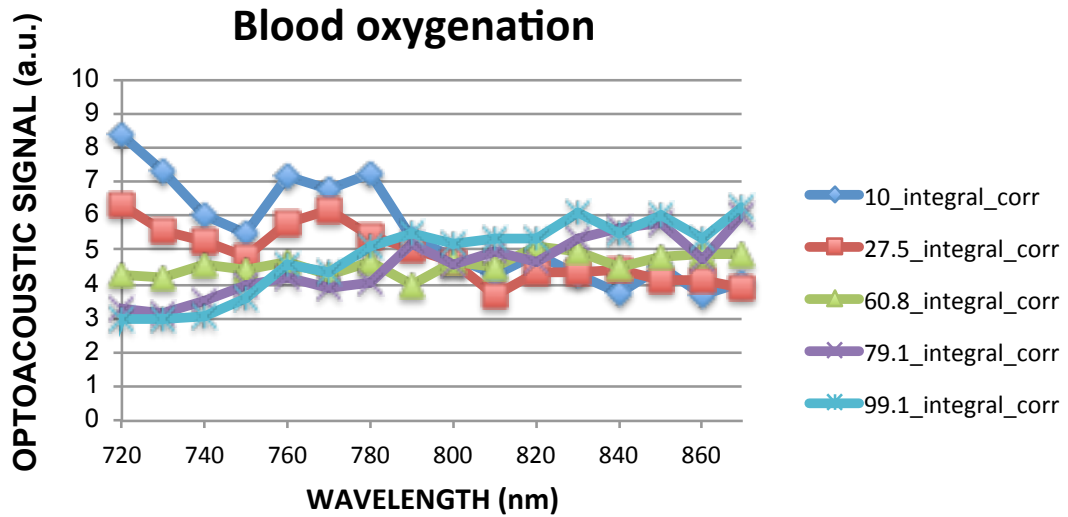
Gas analyzer (Sat.)	Integral (Sat.)
10.00%	9.50%
27.50%	30.49%
60.80%	59.71%
79.10%	78.64%
99.10%	98.00%

Figure 3.9: Blood oxygenation saturation level measurements. (Top) Graph obtained for the different blood tubes with the optoacoustic spectrometer. (Botton) Comparison between gas analyzer measurements and optoacoustic results after linear fitting.

3.7 Discussion

The adequate selection of exogenous contrast agents is crucial while enhancing the sensitivity of MSOT. A wide variety of photo-absorbing substances can be used as probes with several important characteristics depending of the specific application. Some of these features involve absorption spectrum, toxicity, size, shape, chemical composition and targeting capacity. Absorption efficiency and photostability of the probe are important parameters determining the necessary dose for a certain purpose and therefore its kinetics, targeting efficiency and potential adverse effects.

In this chapter, we analyzed the efficiency and stability of commonly used optoacoustic probes in realistic small animal imaging scenarios. For the experiments, the near-infrared spectral range was selected due to the superior penetration of light in these spectral wavelengths. As estimated, it was calculated that the amplitude of the optoacoustic signals emitted by fluorescent dyes is respectively reduced by their quantum yield in comparison to other probes having the same optical density but measured with a spectrophotometer. Finally, it was shown that the bleaching effect due to exposure to the nanosecond light may considerably vary among the different fluorescent dyes. A self-developed optoacoustic spectrometer further allowed the experimental determination the optoacoustic spectrum of the probes.

4 Rotational Mesoscopic MSOT

4.1 Introduction

Heterogeneity in the tumor microenvironment creates gradients in cell production rate and areas of hypoxia and acidity, all of which can affect the sensitivity of tumor cells to drug treatment [73]. *In vivo* high resolution imaging of tumors can thereby potentially provide a better understanding of cancer development principles and microenvironment gradients [74]. Indeed, the administration of contrast agents and the use of new imaging systems have substantially contributed to the understanding of tumor functional and histological characteristics, with the objective to progress in the development of effective anticancer therapeutic techniques [75–82].

In order to study the microenvironment gradients in living organisms, in particular within and around solid tumors, novel MSOT setups with higher resolution capacity are being developed. In this direction, we created a novel Rotational Mesoscopic MSOT (RM-MSOT) system. It is based on tomographic detection of signals with cylindrically-focused transducers, which is advantageous for many optoacoustic applications [32,68,83–88]. In a similar way to traditional MSOT setups, this system permits the simultaneous analysis of

intrinsic and/or external photo absorbers for anatomic, functional and molecular information with good penetration depth and superior resolution. In this chapter, we describe and characterize the RM-MSOT and present its application for *ex vivo* and imaging of tumors in mice.

4.2 Setup

The Rotational Mesoscopic MSOT (RM-MSOT) system was developed to image solid tumors in preclinical studies with high resolution. The system is depicted in Figure 4.1. Several important components can be distinguished, the OPO laser to provide illumination, the water tank with a capacity of 70 L offering a coupling medium for the optoacoustic signals, a cylindrically-focused ultrasound transducer (a detector with 15 MHz central frequency was primarily used), the motors to position the different samples and the acquisition PC system to register and save the data, which was subsequently used to reconstruct the images. For measurements, the water temperature was maintained at a constant value of 34^0 with two heaters HT200 (Tetra, Melle, Germany).
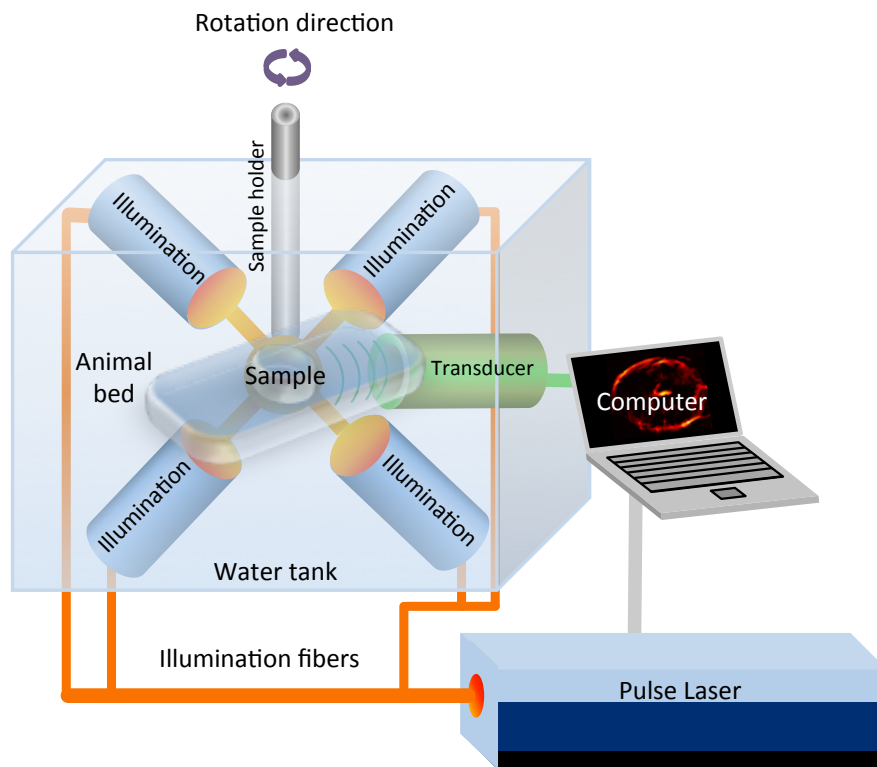
Figure 4.1: Schematics of the RM-MSOT system. The sample is illuminated with 4 waterproof optical fibers inside a water tank. An ultrasonic cylindrically-focused transducer with 15 MHz central frequency was used to receive the optoacoustic signals from the samples. An animal bed with a plastic membrane for the animal experiments, enabled positioning the area of interest to water. All the components of the RM-MSOT system as well as the acquisition card and motors (not showed in this figure) were controlled by a computer.

4.2.1 Laser illumination

The illumination elements of the system were mounted and aligned in an optical table, avoiding vibrations and providing safe operations, in particular related to laser hazards. The near-infrared light was delivered by a tunable OPO class IV laser Vibrant 5312I (OPOTEK, Carsbad, CA, USA), being pumped with a flash-lamp excited Nd:YAG laser (Brilliant, Quantel, Les Ulis, France). The pump laser creates a beam at a wavelength of 1,064 nm. Two different mirrors redirect

this beam into a Second Harmonic Generator (SHG) where is transformed to 532 nm. The initial laser beam is horizontally polarized parallel to the table, and a λ/2 waveplate turns the polarization of the beam in order to adapt it to the SHG. 4 dichroic mirrors guide the 1,064 nm beam to a beam block to prevent that it reaches the OPO. A dichroic mirror is used to guide the pump beam into the OPO. The internal prism of the OPO retro-reflects the residual pump beam at 532 nm back towards the laser. Another mirror redirects this beam away from the laser. A wavelength separation module isolates the signal from the idler. The OPO beam comes outside the laser after crossing the attenuator module.
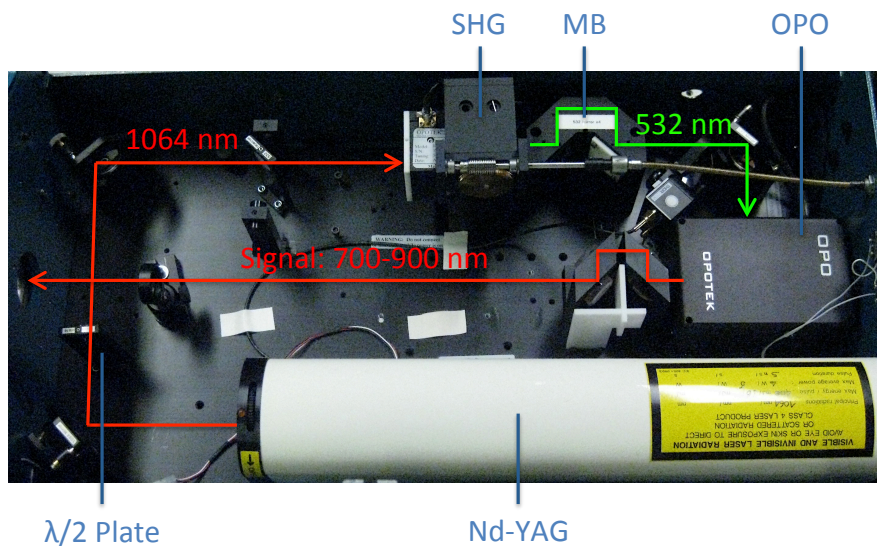
Figure 4.2: Opotek Vibrant 5312I laser system. The principal components of the Vibrant are the Nd:YAG laser, the λ/2 plate, the second harmonic generator (SHG), the mirror block (MB) and the optical parametric oscillator (OPO).

The OPO converts the input laser at a wavelength of 532 nm into two beams (signal and idler) with longer wavelengths. A laser beam (pump) with a frequency of ν_p comes into a cavity and interacts with a non-linear crystal, creating the two beams already mentioned with frequencies ν_s (signal) and ν_i (idler). These frequencies are related with the energy conservation equation as [89]

$$\nu_p = \nu_s + \nu_i.$$

<div align="right">(4.1)</div>

For a wavelength of 532 nm for the pump beam, a tunable signal wavelength λ_s between 690-950 nm and a tunable idler signal wavelength λ_i in a range of 1,200-2,450 nm are rendered. According to Eq. (4.1), the wavelength splitting is as follows

$$1/532 = 1/\lambda_s + 1/\lambda_i.$$

<div align="right">(4.2)</div>

In this work, only the signal beam coming from the laser was used and guided with a custom-made fiber bundle. The bundle has an input diameter of 3.6 mm and it consists of 260 quartz fibers melted together in the input side and arranged to 4 waterproof output arms with 65 fibers each (Ceramoptec Industries Inc., East Longmeadow, MA, USA). The arms were positioned in a symmetric way (separated by an angle of 90^0) in the water tank around the sample. Each of the fibers had a diameter of 200/230 μm core/cladding and a length of 1.8 m. The fiber bundle was protected by a flexible PVC-Kevlar compound that allows contact with water and also flexibility in the bend parts. Each arm finished in a minimal size ferrule with the fibers located next to each other, so that the sample is illuminated in a slice as thinner as possible parallel to the optical table.

The idler beam presented some disadvantages to irradiate the samples like lower pulse energy (1/3 of the signal) and absorption in the coupling water medium in the mentioned spectral range, although these wavelengths present a higher maximum permissible exposure (MPE) in tissues. The illumination energy on the sample surface was always under 20 mJ/cm² according to laser safety standards [90].

The Q-switch of the laser was coupled to a rectangle function trigger signal and transmitted to the acquisition card by a coaxial cable in order to synchronize the recorded optoacoustic signals to the transducer with the corresponding light pulse.

The laser power was measured in the first experiments with a power meter FieldMaxII-Top (Coherent®, Santa Clara, CA, USA) and saved to allow light fluctuation corrections during later analysis. In an accurate and more automatic way, a photodiode DET10A from Thorlabs (Newton, NY, USA) was added after to the system at the entrance of the 4-arms fiber bundle to correct the power for each laser pulse. The data was recorded by one of the channels of the acquisition card described later in section 4.2.3.

4.2.2 Ultrasonic detectors

The election of the ultrasonic transducer in optoacoustic tomographic imaging is conditioned by the size of the imaged structures in the sample, which relates to the frequency bandwidth of the emitted signals. The characteristics of the single element ultrasonic transducers used in this thesis are displayed in Table 4.1. The beam width and length have been calculated with Eqs. (2.2) and (2.3), respectively.

Transducer	Focus	Central Frequency (MHz)	-6dB Bandwidth (MHz)	Focal Length (mm)	Element Diameter (mm)	-6dB BW (μm)	-6dB BL (mm)
PNDT V319	CF	15.28	7.3	19.1	13	150	1.7
PNDT V320	CF	7.5	5.8	25.4	13	400	5.8
PNDT V382	CF	3.5	2.8	38.1	13	1,281	24.7

Table 4.1: Ultrasonic transducers used with different parameters. PNDT: Panametrics NDT, CF: Central Focused, BW: Beam Width at the Central Frequency, BL: Beam Length at the Central Frequency.

For a transducer with a short focal length, the BW is shorter and the BL is smaller (less depth of field) than for a transducer with a longer focal length and the same diameter. A transducer with a short beam width leads to a better vertical resolution in tomography scanning due to the ability to record slices with thinner step between them. From the transducers displayed in Table 4.1, the transducer PNDT V319 probably represents the best alternative to acquire an optoacoustic 3-D reconstruction of a small structure like a tumor by stacking multiple slices due to its smaller BW and a BL. Considering that the transducer focal length for this element is short, larger samples do not fit in the scanning geometry, so that the best option to image bigger objects is probably the PNDT V382. For this transducer, the vertical resolution is reduced but the field of view is larger. The deterioration in the tomographic reconstructions when imaging structures located out of focus can be partially resolved by modeling the shape of the transducers in the reconstruction algorithm [91].
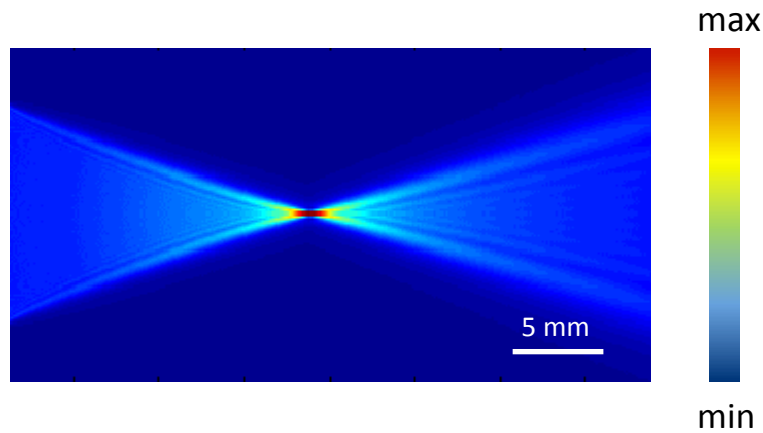
Figure 4.3: Beam shape for the PNDT V319.

4.2.3 Signal amplification and recording

The transducers were connected to active amplifiers AU-1291 (Miteq, Hauppauge, NY, USA) with a gain of 63 dB. After amplification of the optoacoustic signals, they were digitalized with a dual channel acquisition card Gage Octopus Compuscope 8327 (Gage, Lockport, IL, USA) with 14 bit vertical resolution. Due to the limitation of the acquisition card, a maximum of two simultaneous measurements with two different transducers was performed, where the transducers where positioned at opposite sides from the sample. The recording parameters, such as the number of acquired channels, amount of projections per slice, quantity of imaging slices, total time points per projection, acquisition mode (continuous or stepping the motors) and illumination wavelengths, were controlled with a self-developed graphical user interface (GUI) in Labview (National Instruments, Munich, Germany).

4.2.4 Stages

The samples were placed in the center of the transducer focal zone with 3 motorized linear stages corresponding to each of the 3 Cartesian axes. For the X and Y directions, linear stages with 50 mm travel distance were used (MTS50-Z8),

and for the Z direction a linear stage with 100 mm travel distance was employed (NRT100/M). A motorized rotation stage (PRM1-Z8) was then used to rotate the sample and acquire signals from different angular projections. The vertical rotation axis is located in the center of the transducer focal zone and fixed illumination is maintained during the rotation scan. The linear stages for the X and Y coordinates and the rotation stage were connected to 3 DC Servo Motor Controllers TDC001. On the other hand, a BSC101 one-channel stepper motor controller governed the Z- axis. The motors and controllers were manufactured by Thorlabs (Newton, NY, USA).
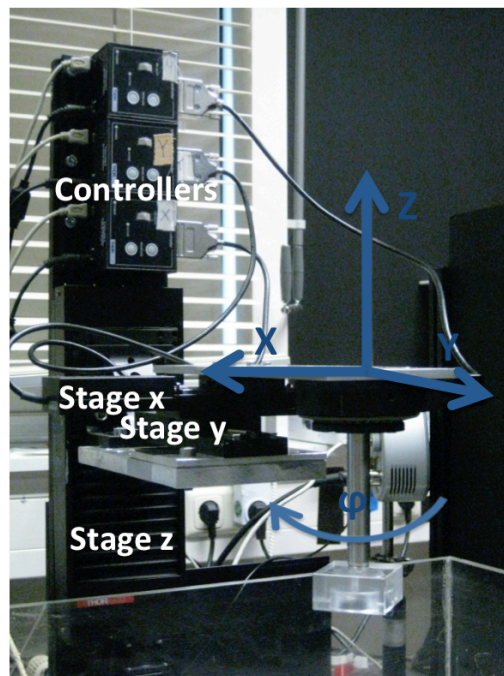
Figure 4.4: Stages and controllers in the RM-MSOT system. The linear stages for the Cartesian coordinates X, Y and Z and the rotation stage φ with a holder for phantoms connected to their respective controllers.

To acquire different cross-sectional images, the samples were moved along the Z-axis with a certain step after finalizing a complete rotation scan (360⁰). For phantom experiments, these were attached to a holder fixed to the rotation stage as presented in Figure 4.4. When experiments with mice were performed, the

animals were positioned in a plastic bed attached to the rotation stage with the tumors in contact with water as a coupling medium as explained in 4.5.2.3.

The maximum rotation speed of the PRM1-Z8 is 25^0/s, which corresponds to complete a single slice in 14.4 s. In such case, a rotational scan consists of acquisition of 288 signals for a laser repetition rate of 20 Hz. Continuous acquisition of signals while rotation (no averaging) corresponds to the fastest method to acquire optoacoustic signals. The rotation speed can then be adjusted according to the number of projections needed. Alternatively, step-wise rotation can be performed, where the rotation scan is stopped at each projection so that the signals are averaged for a given number of illumination pulses.

For the images presented in this work, continuous acquisition with a large number of projections was done, presenting similar signal to noise ratio (SNR) results that the ones done in the same time with less projections and stepping the rotation stage. The continuous acquisition approach does not suffer of Doppler distortions as it was shown in [92]. In the experiments explained below, a total of 4000 projections were acquired for every tomographic slice. This number presented a reasonable tradeoff between SNR and acquisition time for experiments.

Optoacoustic images with equivalent acquisition times of a hexagonal India ink insertion in a scattering phantom in continuous mode and stepping the rotation stage are compared in Figure 4.5 A-B respectively. Back-projection reconstruction was used in both cases. The SNR defined as the ratio between the μ_{signal} (average signal value) in the purple area and the $\sigma_{background}$ (standard deviation of the background) in the yellow square is calculated for images obtained with continuos acquisition, considering different number of projections. The results are plotted in Figure 4.5 C, where the SNR follow a non-linear increase with the number of projections [93].
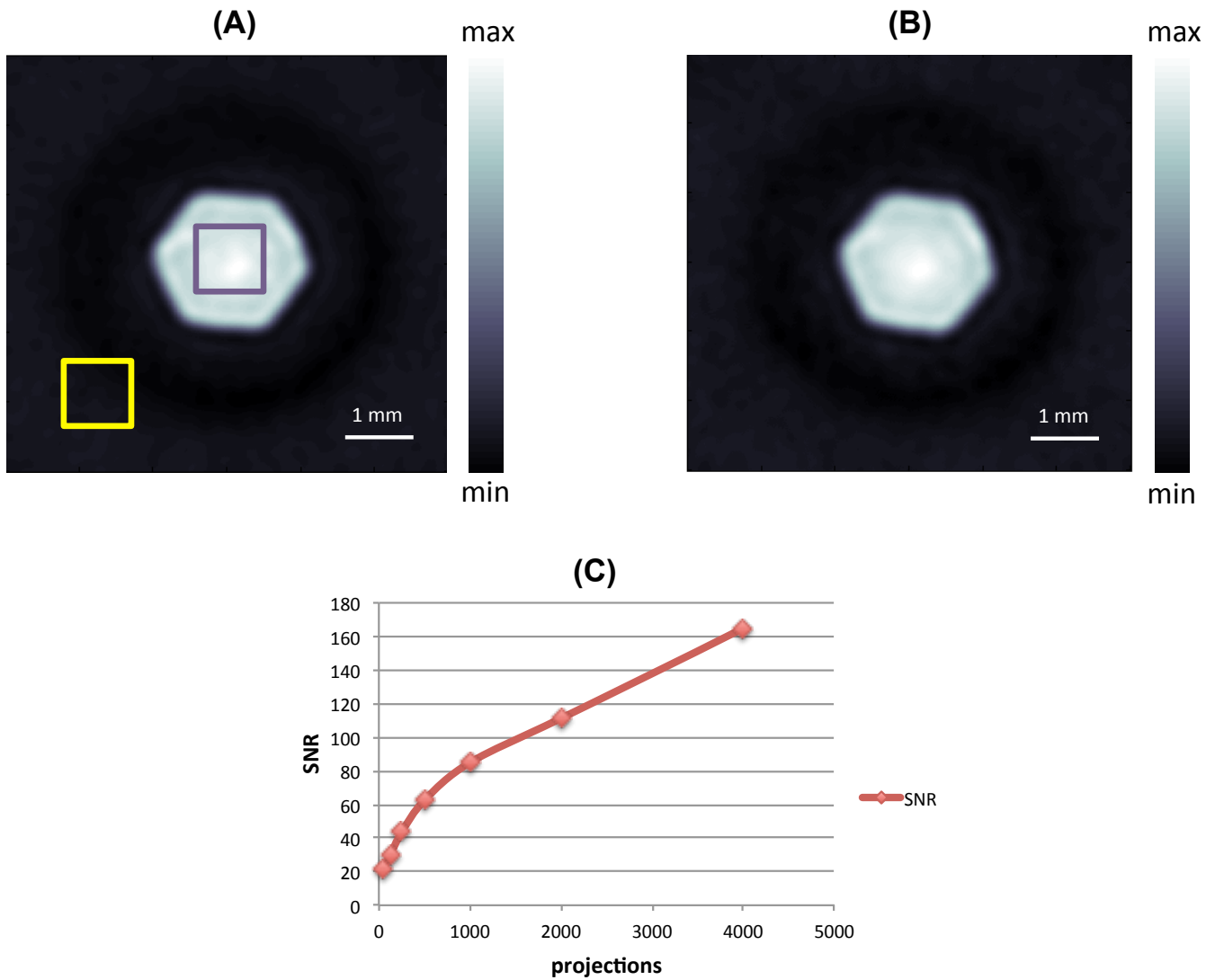
Figure 4.5: Optoacoustic reconstructions with different number of projections. (A) Optoacoustic image of an India ink insertion in a scattering phantom acquired with 4000 projections in continuos mode. (B) Same optoacoustic slice obtained by stepping the rotation stage with 91 angular projections around the 360⁰ and 18 averages in each projection (same acquisition time than in A). (C) Comparison of the SNR between the signal in the hexagon (purple) and the background (yellow) for images acquired as in A using different number of projections.

A very important factor while performing optoacoustic acquisition in continuous mode is the correct movement of the rotation stage without interruptions and at a constant speed. To illustrate that the stage movement is

correctly performed, a sinogram of 3 microspheres with 100 μm size embedded in the same Z-plane in a scattering phantom is represented in Figure 4.6. The illumination wavelength employed was 750 nm corresponding to the maximum energy of the laser. The results indicate a smooth rotation around the sample and a correct reconstruction of the microspheres with the back-projection algorithm.
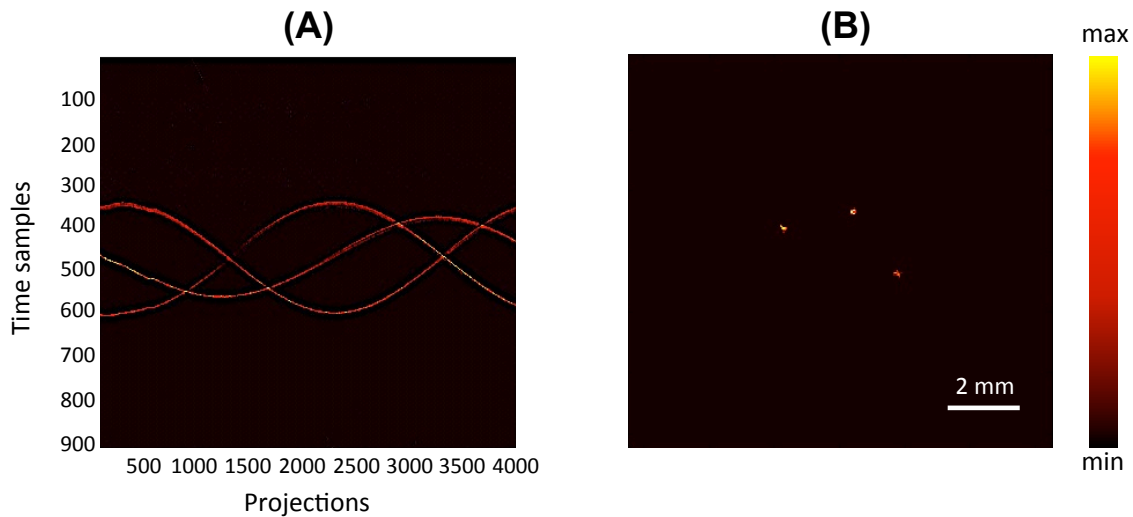
Figure 4.6: **Rotation around the sample and reconstruction. (A) Optoacoustic sinogram of 3 microspheres with 100 μm size. The time samples of the recorded optoacoustic signals are represented for every projection as sinusoids. The three curves appear to be smooth around the 360⁰ showing a continouos movement of the rotation motor. (B) Back-projection reconstruction of the same microspheres.**

4.3 Characterization of the system

Phantom experiments were performed to characterize the resolution, optical penetration and sensitivity of the system. The characterization phantoms were done using 1.3% (wt./vol.) agar (Sigma-Aldrich, St. Louis, MO, USA) in H2O. Intralipid (Sigma-Aldrich, St. Louis, MO, USA) was added to get a reduced scattering coefficient μs' = 5 cm-1. The final size of the phantoms was 18 mm in

diameter and 45 mm height. No optical absorption was added to the phantoms. A different tissue-mimicking phantom was used to characterize the optical penetration. The diameter and height of this phantom were 30 mm and 45 mm, respectively. India ink (Higgins, Sanford Bellwood, IL, USA) was added to this phantom to achieve a μ_a coefficient of 0.25 cm-1 at 800 nm. Intralipid (Sigma-Aldrich, St. Louis, MO, USA) at a concentration of 1.2% (vol./vol.) was also included, corresponding to a scattering coefficient μ_s' of 10 cm-1. The absorption and scattering coefficients of the phantom mimic those of blood at one of its isosbestic points (800 nm). The transducer used for the characterization experiments was the PNDT V319 as described in Table 4.1.

4.3.1 In-plane and vertical resolution

To evaluate the in-plane resolution of the RM-MSOT system, a cylinder scattering phantom containing two 20 μm diameter sutures forming a cross shape was imaged. The illumination wavelength was set to 750 nm and a band-pass filter was applied to the optoacoustic signals with cut-off frequencies between 5 and 25 MHz. The phantom was scanned along the Z-axis with a step of 50 μm between optoacoustic slices, creating a total of 50 different tomographic planes being reconstructed with back-projection. In Figure 4.7 A the reconstructed 3D volume of the sutures is presented. To calculate the in-plane resolution, a representative 2D optoacoustic slice near the suture intersection was selected from the acquired stack (Figure 4.7 B). The central profile of this image was extracted (blue in Figure 4.7 B) and fitted to a combination of two Gaussian curves (red in Figure 4.7 C). The resolution was defined according to the Rayleigh criterion by taking the distance between the centers of the Gaussians (green and black curves in Figure 4.7 D). The measured distance was 52 μm, which corresponds to the width of the convolution of the point spread function (PSF) of the system (corresponding to a point source) and a square function of

width 20 μm (representing the suture). Thereby, the full-width at half maximum of the PSF of the system was estimated as 50 μm, representing the actual resolution.
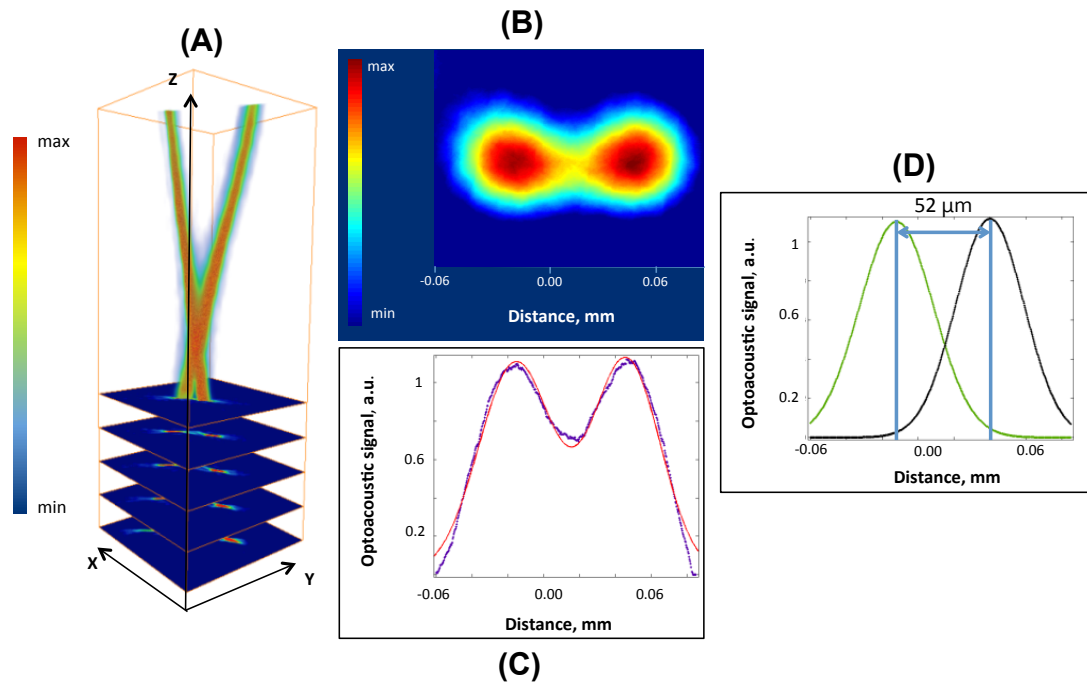
Figure 4.7: In-plane resolution obtained with the RM-MSOT system. (A) 3D optoacoustic reconstruction of two sutures forming a cross inside agar phantom after scanning with RM-MSOT along the Z-axis to study the in-plane resolution. (B) One of the images from the 3D-stack near the intersection of the two sutures. (C) Optoacoustic signal intensity profile along the middle of image B (blue). Also the fitting for the profile has been calculated (red). (D) Gaussian curves calculated after the fitting in C (green and black). The two Gaussians have been move until matching the Rayleigh criterion. The in-plane resolution was estimated as 50 μm.

The vertical resolution was studied with a suture with 30 μm diameter. It was scanned 15 mm along the Z-axis and parallel to the transducer focal area. One single spatial projection was acquired without rotating the sample, after 100 averages with a step of 10 μm. The illumination wavelength was set to 750 nm and the same filter as in the in-plane resolution experiment was applied for each

of the signals after averaging. Figure 4.8 presents the graph for the distribution of the maximum of the optoacoustic signal along the Z-axis at each measurement step (blue). After applying a Gaussian fit (red), the vertical resolution measured was estimated as 311 μm according to the Full Width at Half Maximum (FWHM) principle. Unlike the in-plane resolution, the vertical resolution was not significantly affected by deconvolution taking into account the suture size.
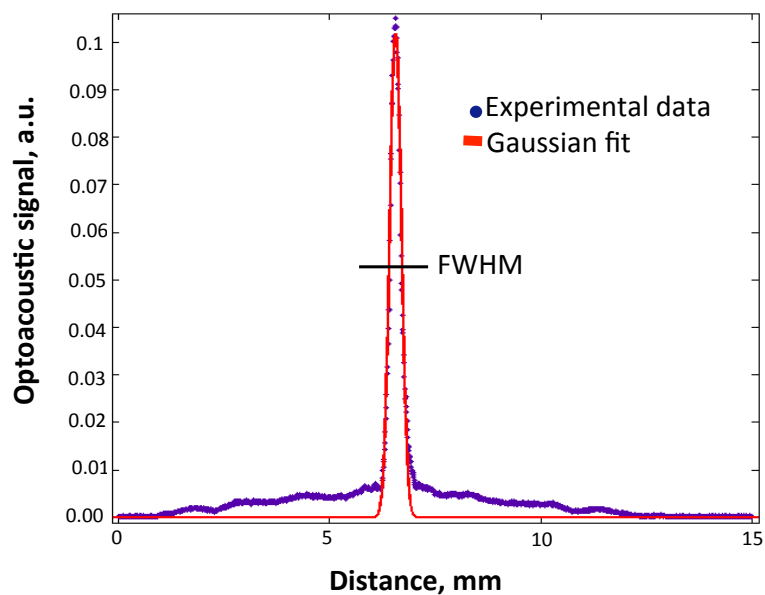
Figure 4.8: Vertical resolution measurement with RM-MSOT system. The spatial distribution of the maximum of the optoacoustic signal along Z-axis for each of the 10 μm steps acquired from the phantom containing a 30 μm thick suture is shown (blue). The vertical resolution measured after a Gaussian fit (red) was 311 μm according to the FWHM.

4.3.2 In-plane artifacts

One of the effects produced while performing OAT with a cylindrically-focused transducer having a finite width is the smearing in the images in absorbers that are positioned away from the center (in-plane artifacts). This is created due to the fact that reconstructions assumed point detectors in the model and not a

transducer with a certain surface. To illustrate this effect, a cylindrical-scattering phantom was done with 50 μm size microspheres located at the same plane. One single optoacoustic slice of the microspheres was reconstructed with direct back-projection (assuming point detectors) and with model-based inversion (assuming a line detector). The resulting images are showcased in Figure 4.9. The second method was chosen due to the reason that all the optoacoustic signals came from the same 2-D plane so that no out-of-plane artefacts are present. In Figure 4.9 (right) the correction of the smearing in the microspheres far from the center is clear. Modelling the shape of the transducer in the elevation direction would help minimizing the out-of-plane artefacts, which are not present in the example above but can be significant in practical cases. However, a three-dimensional model is required for this purpose, leading to unaffordable memory requirements for the resolution and number of projections of the system. Future developments of the model are however expected to further improve the reconstructions.

Direct Back-projection   Line detector Model-based
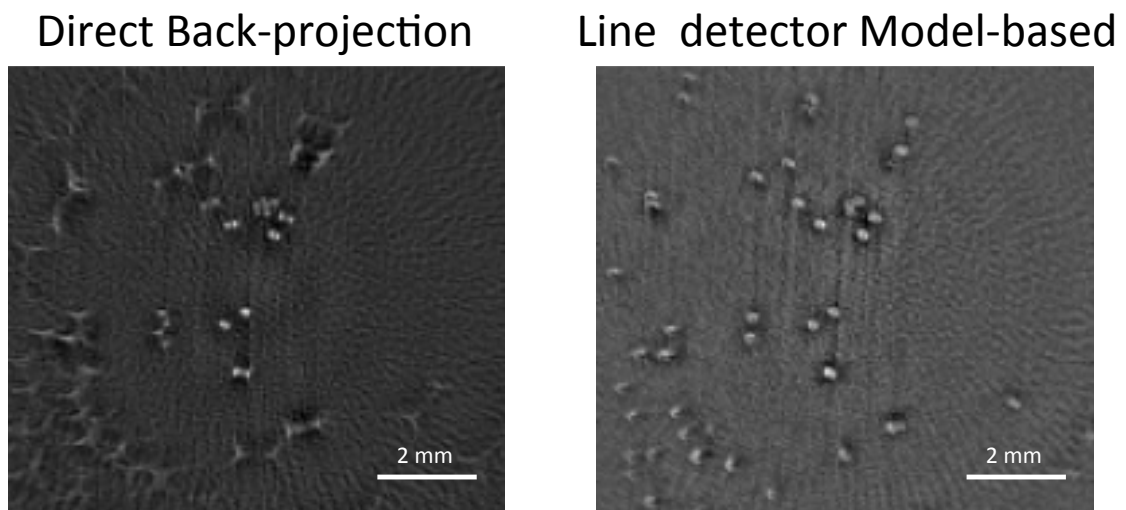
Figure 4.9: Reconstruction of microspheres. (Left) Direct back-projection optoacoustic image of 50 μm size spheres. (Right) Line detector model-based reconstruction for the same microspheres with correction of the smearing effect.

4.3.3 Measurements with two transducers

To prove the capability of the system to detect optoacoustic slices with two different transducers, the V319 and V320 were connected to the acquisition card symmetrically with the sample in the middle. In this case, a scattering phantom with 5 microspheres (3 of them with 200 μm and 2 with 100 μm) in the same Z-level was scanned. The results are shown in back-projection in Figure 4.10.
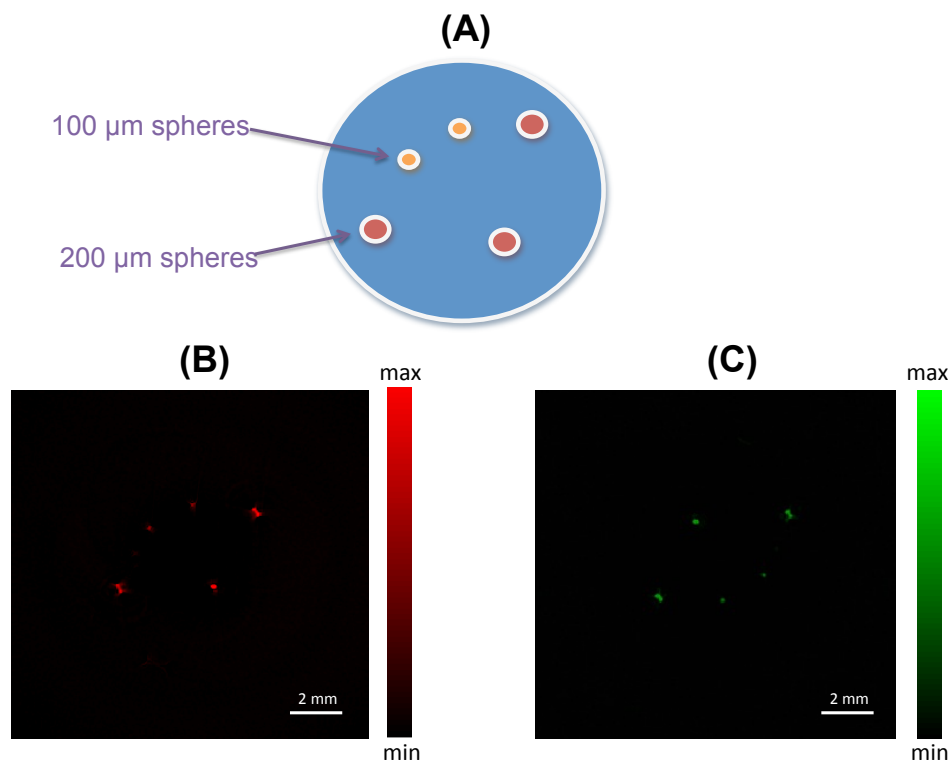
Figure 4.10: Reconstruction of microspheres with 2 transducers. (A) Diagram of the phantom with the microspheres. (B) Optoacoustic reconstruction of the microspheres using the 15 MHz central frequency transducer. (C) Optoacoustic reconstruction similar to B using the 7.5 central frequency transducer with 180⁰ difference in the image.

4.3.4 Optical penetration depth

To study the optical penetration capability of the RM-MSOT system, a phantom with similar absorption and scattering properties as in biological tissues was used to emulate the effects of imaging of deep-located structures. This phantom contained a 2 mm size hexagonal insertion with 10-fold absorption and same scattering as compared to the background, which simulates a possible blood vessel. A single optical plane of the phantom was acquired at 800 nm as explained above in Section 4.2.4. Figure 4.11 shows the optoacoustic reconstruction of the insertion obtained with direct back-projection. The calculated SNR ratio ($\mu_{signal}/\sigma_{background}$) between the signal in the center of insertion (red square) and background (white square) was 11.01, which was in agreement with the measured initial phantom absorption characteristics. This result demonstrates the capability of the system to image blood structures at depths of 15 mm within biological tissues, which is much deeper than the tumors studied.
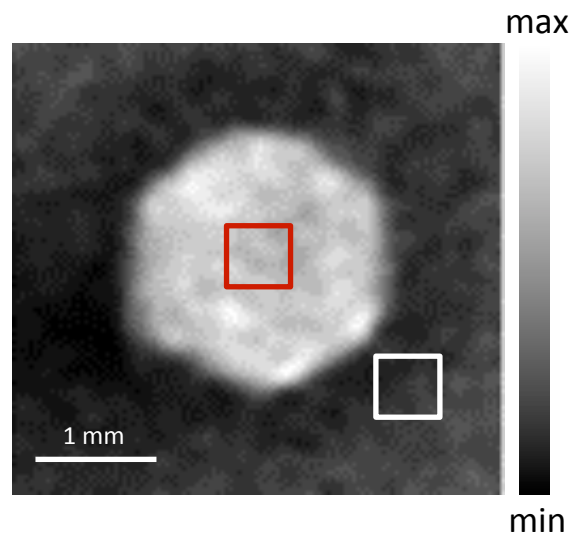

Figure 4.11: Insertion in tissue mimicking phantom. The estimated measured SNR ratio between the signal (red square) and background (white square) was 11.01.

4.3.5 System sensitivity

To estimate the sensitivity of the RM-MSOT system to detect external contrast agents, a scattering phantom with a 3 mm white plastic straw containing either liposomes with indocyanine green (Lipo-ICG) or AuNR disolved in DPBS (Gibco®|Life Technologies, Carsbad, CA, USA) to achieve various optical densities (0.25, 0.5, 1 and 2) was imaged at the peak absorption wavelengths (800 nm for the Lipo-ICG and 720 nm for the AuNR). Results show that both contrast agents could be visualized at all ranges of ODs studied, where the probes with higher concentration (Figure 4.12 A) present higher signal compared to the ones with lower concentration. The dependence of the optoacoustic signal and the OD of the probe were quantitatively studied. Therefore, the average optoacoustic signal was measured for each of the pixels inside the straws containing Lipo-ICG or AuNR in various concentrations and compared with the previously calculated OD in the spectrometer. As shown in Figure 4.12 B, the optoacoustic signals were directly proportional to the measured OD of the contrast agents. Linear regression equations and determination coefficients (R^2) were calculated to define how linear was the dependence between optoacoustic signals and ODs. The linear regression equations for Lipo-ICG and AuNR were respectively: y=6.5605x+2.1973 and y=2.8993x+0.0674. The calculated regression coefficients were R^2=0.9924 for Lipo-ICG and R^2=0.9957 for AuNR, which verified the capability of the imaging system to detect and differentiate external probes at different concentrations.

(A)   **(B)**
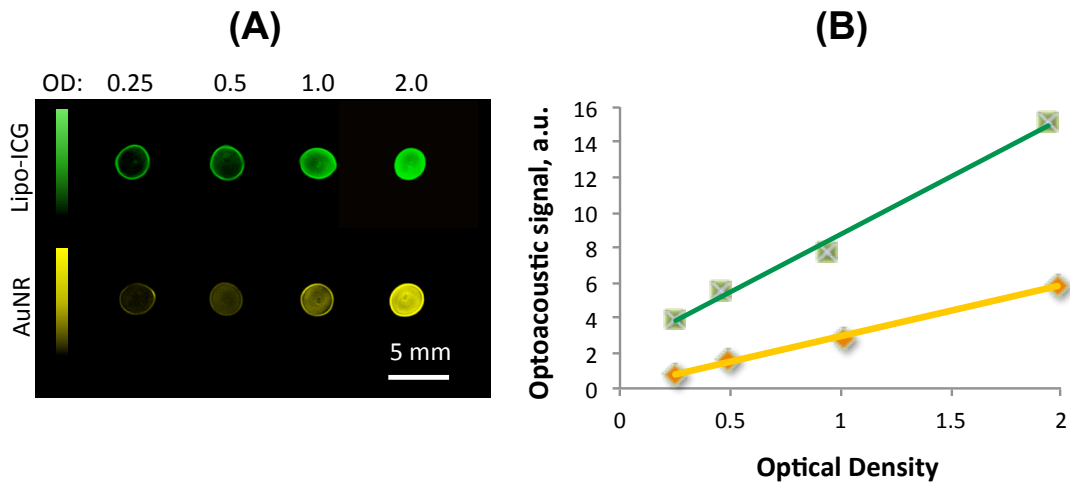
Figure 4.12: System sensitivity with external contrast agents. (A) Lipo-ICG (green) and AuNR (yellow) at several ODs were imaged showing an increasing optoacoustic signal from left to right. (B) Graph of the average optoacoustic signal inside the straws in dependence from OD measured with the spectrometer. Linear regression showed the dependence to be linear, for Lipo-ICG: y=6.5605x+2.1973 and R2=0.9924. For AuNR: y=2.8993x+0.0674 and R2=0.9957.

Figure 4.13 shows the ability of the RM-MSOT system to detect common external contrast agents used for studies upon multispectral imaging and specific signal unmixing with linear regression. A scattering phantom was imaged at different excitation wavelengths in one single slice, containing Lipo-ICG and AuNR in 3 mm size plastic white straws (2 OD each probe in the peak of their optical spectrum after being diluted in DPBS). The illumination wavelengths used were 700, 720, 770, 800, 830 and 860 nm. Model-based reconstruction and linear regression unmixing differentiated the two external contrast agents inside the phantom.
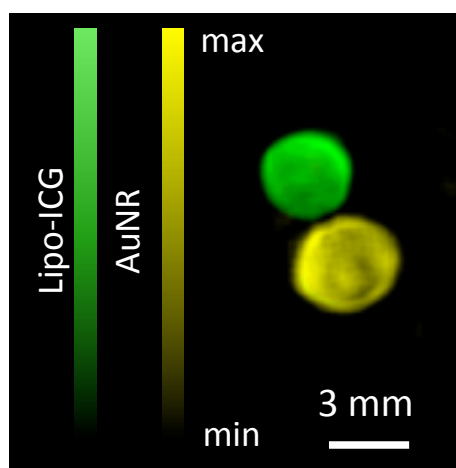
Figure 4.13: Unmixing of external contrast agents. In this case Lipo-ICG appears in green and AuNR in yellow with 2 OD in the peak of their optical spectrum.

To confirm the capacity of the RM-MSOT system to multispectrally unmix intrinsic contrast agents in biological tissues, a scattering phantom was imaged with oxygenated and deoxygenated New Zealand white rabbit blood *ex vivo* in 1 mm inner diameter Fine-Bore Polyethylene tubes (Smiths Medical, London, England). The blood oxygenation level was controlled by adding sodium hydrosulfite in Dulbecco's Phosphate-Buffered Saline similar to 3.6 and checked by the gas analyzer. As shown on Figure 4.14, the reconstructed images by model-based inversion algorithm contained 300 pixels and 4.3 mm field of view. Spectral fitting for the acquired and reconstructed images successfully revealed oxygenated (HbO_2) and deoxygenated hemoglobin (Hb), the principal intrinsic absorbers in mammalian blood.
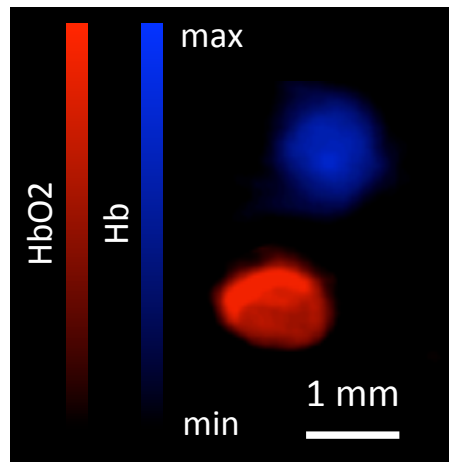
Figure 4.14: Unmixing of intrinsic contrast agents. Oxygenated blood appears in red and deoxygenated blood in blue.

4.4 Image reconstruction and unmixing methods

4.4.1 Reconstruction with different algorithms

To compare the performance of different reconstruction methods in optoacoustic imaging, the same acquired data with the RM-MSOT system was reconstructed with different approaches. Specifically, a HT29 tumor after 24 hours injection of Lipo-ICG was selected as a reference (same tumor studied in Section 4.5.3.2). The images obtained are shown in Figure 4.15. Figure 4.15 (i-x) are anatomical images of the tumor acquired at 800 nm (peak of the optical absorption spectrum of Lipo-ICG).

The first one (Figure 4.15 (i)), corresponds to the direct back-projection reconstruction, where for each of the 4000 projections, the optoacoustic signals recorded are "back-projected" in time and sum in each of the possible source pixels. It is the fastest and most memory demanding method and is normally used to render a qualitative image of the structures in the sample. It is generally a good

approach in devices with several detectors or arrays, giving real time optoacoustic images of tissues [94].

The next one (Figure 4.15 (ii)), tries to resolve the common problem of negative values with no physical meaning in a simple way, namely setting negative values to zero. In a first impression, most of the background noise disappears and the borders of the tumor are more defined but the inner parts remain without information.

On the other hand, model-based reconstruction represents a more memory-consuming approach. The image retrieved with this procedure is presented Figure 4.15 (iii). The main problem is the time to calculate the model-matrix A as already mentioned in Eq. (2.31), where the solution for the absorption was obtained with the LSQR algorithm. This matrix is dependent of the geometry of the setup and the speed of sound. Then, the same model-matrix cannot be used in two transducers with different focal distances acquiring data at the same time in the RM-MSOT system. Furthermore, in many cases the speed of sound is not known and the model-matrix has to be built several times for optimizing image quality. The reconstruction shows a better view of the inner part of the tumor and more characteristic vessels.

In Figure 4.15 (iv) the results obtained with model-based reconstruction and Tikhonov regularization are displayed. Using the RM-MSOT system, the optoacoustic reconstructions do not need of regularization because the whole 360 degrees are covered (full-view acquisition). In a limited-view scenario, Tikhonov regularization is a convenient method in the inversion process. Depending of the parameter λ (already explained in Eq. (2.32)) the penalty term is affected, thereby the reconstructions. With a λ =1 the results are the same than in Figure 4.15 (iii). In this case, the regularization parameter was designated as the result of the Frobenius norm of the model-matrix A.

Figure 4.15 (v) displays the image reconstructed with the weighted model-based reconstruction algorithm, which attempts to reduce the effect of internal

reflections and scattering of the acoustic waves in each of the detector projections around the tumor. The probability of the acoustic waves at a given detector position and time of being reflected or scattered during their propagation paths is taken into account, trying to give a more realistic view of the real absorption distribution in tissue.

The negative values retrieved in model-based reconstructions can be avoided with a LSQR minimization and a positive constrain to the optical absorption H. The image retrieved with this reconstruction method is displayed in Figure 4.15 (vi). As opposed to the unconstraint formula in Eq. (2.31) that can be computed directly, the model-based with positive constrain can only determined in an iterative way.

One of the principal problems while performing optoacoustic reconstructions with model-based algorithms is the computational requirement needed to invert huge model matrices with a large amount of nonzero values, which makes difficult also the work with sparse time-domain model matrices. Polar coordinates model-based reconstructions decreases the computation time of standard model-based procedures, trying to get the advantage of knowing the geometrical symmetries in most of the optoacoustic tomographic systems. The image retrieved with this approach is displayed in Figure 4.23(vii). In this way, the computation of an efficient model matrix with less memory requirements and faster calculation periods is done. In the already mentioned methods, 4000 projections were used. In this case a polar grid with 4000 angle pixels and 500 radius pixels were used. Here also a positive constrain to the LSQR inversion was done. The final results were similar to the ones obtained in Figure 4.15 (vi) but with a better use of computational resources.

In the already presented images, the signals are assumed to be recorded with a single point detector, although the acoustic pressure is detected in a surface (active area of the transducer). The image in Figure 4.15 (viii) corresponds to an attempt to model the shape of the transducer with a single central line with a

length equal to the diameter of the transducer. Assuming that cylindrically-focused detectors are not so sensible to out-of-plane signals, the optoacoustic problem can be simplified to a 2-D slice. A positive constrain was also introduced in this case. The results confirm that the assumption that only one line is needed is not accurate in practice due to the fact that a sample like a tumor with a certain volume and hence produces out-of-plane signals when measured with a cylindrically-focused transducer. With this configuration of detectors and compare to other type of transducers, the acoustic waves coming from different planes are not so strong although the best solution is to model the transducer in the whole active surface. This approach needs a large amount of memory and is not practical in conventional computers.

The image in Figure 4.15 (ix) is obtained with the same type of reconstruction as in Figure 4.15 (vi), but in this case with light fluence correction as explained in Section 4.4.2. In order to estimate the light fluence distribution, the boundary of the phantom was manually segmented and a simulation was done assuming a homogeneous absorption and scattering coefficients within the tissue. The result of normalizing the model-based tomographic reconstruction obtained with positive constrain with the light one obtained from the simulation shows the inner components of the tumor brighter.

Figure 4.15 (x) displays the same image as in Figure 4.23 (ix) after applying a vessel filter proposed in [95] to define the vasculature of the tumor. This filter organizes the eigenvalue decomposition of the local Hessian matrix at each image pixel to locate tubular structures. In optoacoustic images, it is a very effective filter, removing noise and highlighting vessels. The parameters of this algorithm need to be used very carefully, since is very easy to create ghost vessels from artifacts.

Figure 4.15 (xi) uses different optoacoustic images, acquired at different wavelengths (700, 720, 770, 800, 830 and 860 nm) like the peak wavelength of

the external contrast probe in Figure 4.15 (iii) and with linear fitting and the spectral signature of Lipo-ICG, the probe distribution is mapped.

Figure 4.15 (xii-xiv) presents validation images of the same coronal tumor region *ex vivo* (hematoxylin and eoxin (H&E), epifluorescence and CD31 respectively). The histological validation of tumors is described in Section 4.5.2.4.

Direct-Backprojection
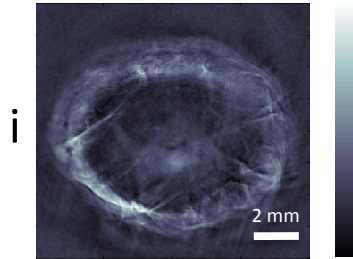
Direct-Backprojection with negative values to zero
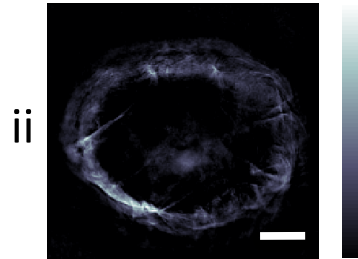
Model-Based
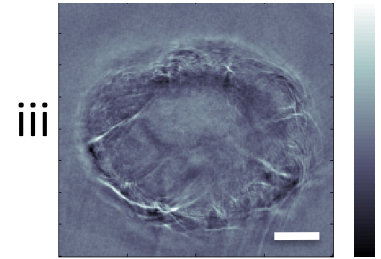
Model-Based Tikhonov Regularization
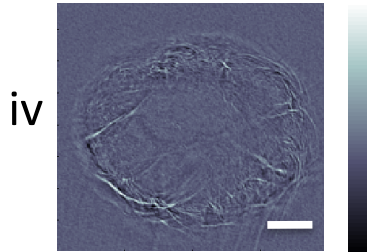
Weighted Model-Based
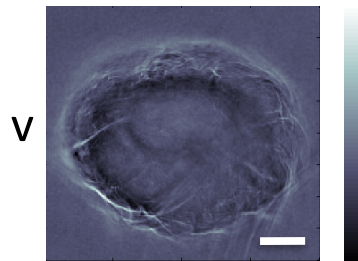
Model-Based Positive Constrain
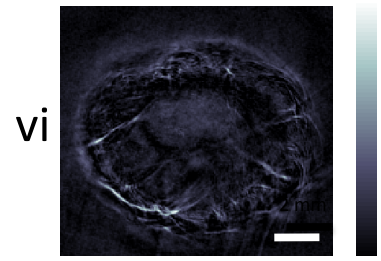
Polar Coordinates Model-Based Positive Constrain
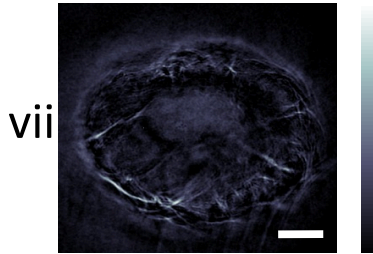
Polar Coordinates Model-Based Positive Constrain Line Detector
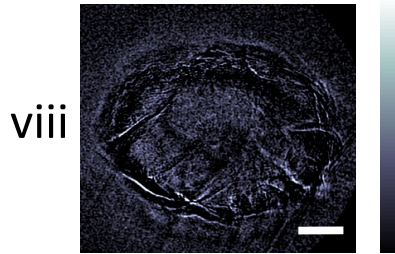
Model-Based Positive Constrain with fluence correction
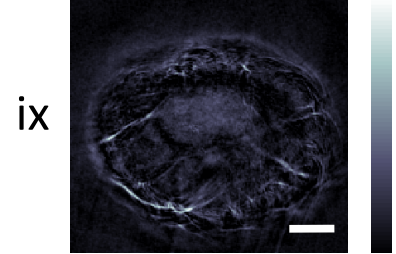
Model-Based Positive Constrain with fluence correction and vessel filter
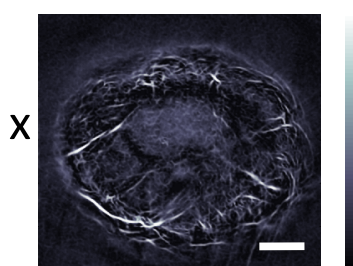
Lipo-ICG Unmixing Model-Based

H&E

Epifluorescence   CD31
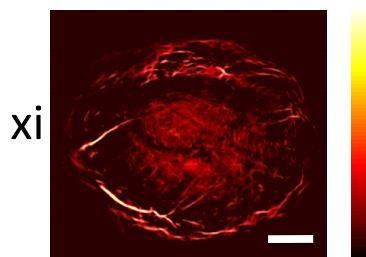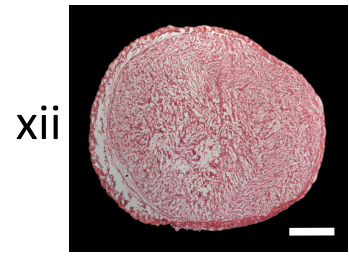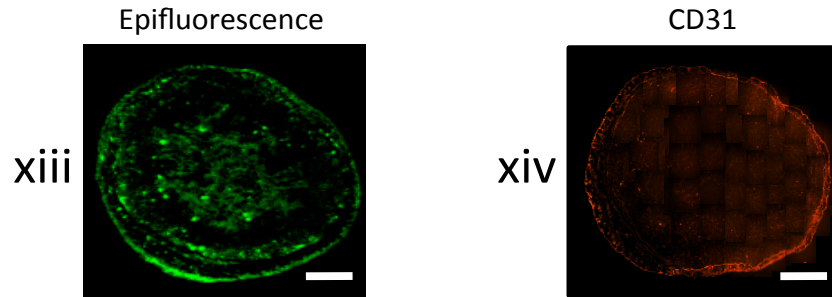
Figure 4.15: Optoacoustic images and validation of a HT29 tumor model reconstructed with different algorithms. (i-x) Optoacoustic anatomical images of the tumor acquired at 800 nm as illumination wavelength (peak of the optical absorption spectrum of Lipo-CIG). (xi) Functional image of Lipo-ICG distribution after spectral fitting. (xii-xiv) Validation images of the same coronal region of the tumor *ex vivo*.

4.4.2 Light fluence correction in tissue

One of the important factors while performing imaging in tumors is the scattering and absorption that light undergoes while travelling through the surface to the inner part of tissue. Consequently, the reconstructed images show that structures located deep inside appear to have a lower intensity as compared to the superficial ones having the same absorption. To avoid this effect, normalization with the light fluence is required. However, detailed modeling of the optical fluence is a difficult task since the distribution of the optical properties within the tissue is not known. However, a simple model of light propagation in a uniform tissue can be sufficient to enhance the quality of the images. In our case, we manually segmented the tumors and considered that the scattering and absorption coefficients were uniform within the tissue. Specifically, the optical properties were chosen as μ_a=0.3 cm^{-1} and $\mu_{s'}$=10 cm^{-1} [96]. Then, we calculated the light fluence distribution using the finite element method (FEM) [97]. An example of the estimated light fluence is shown in Figure 4.16 A, and tumor image being corrected for light attenuation is displayed in Figure 4.16 B.
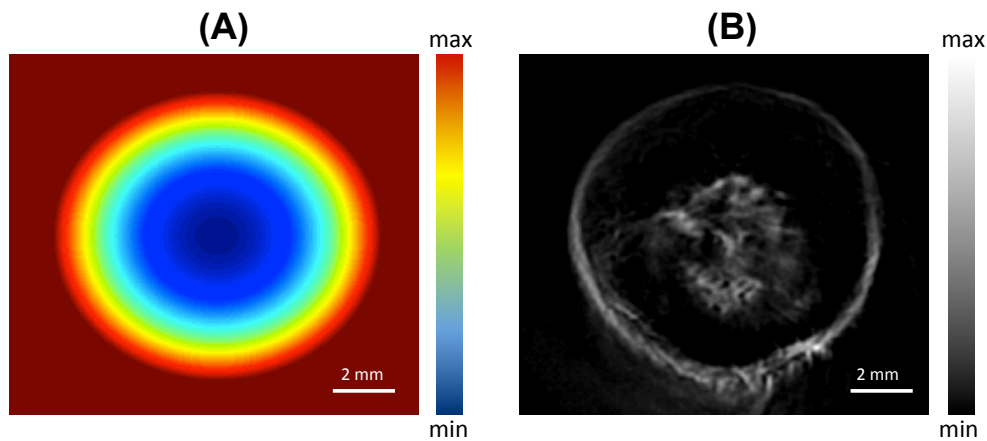
Figure 4.16: Optical attenuation correction in 4T1 tumor. (A) A cylindrical uniform tissue-mimicking phantom with a radius of 5 mm (same radius at the tumor in (B)) and optical attenuation coefficient with values of μa=0.3 cm-1 and μs'=10 cm-1 presented a 50 % of light attenuation with uniform illumination in the surface after simulation. (B) Optoacoustic reconstruction in direct back-projection with negative values to zero of an *ex vivo* 4T1 tumor illuminated at 750 nm with no external contrast agents injected after being divided the original image by the values in (A).

4.5 Optoacoustic imaging of tumor vasculature and probe distribution

4.5.1 Introduction

MSOT as an emerging modality for visualization in nanomedicine due to its spectral differentiation properties [19], permiting accurate resolution of optical contrast agent distribution in tissue. The RM-MSOT system combines these unique imaging features, which are not available in other imaging methods. RM-MSOT is ideally suited to map optical contrast in 3-D and high resolution.

While endogenous contrast agents correspond primarily to hemoglobin, melanin, water and lipids, contrast enhancement can be performed with the help of probes like metal nanoparticles (in most of the cases gold) and organic chromophores or fluorochromes. The last ones, while desired for labelling in preclinical and clinical optical imaging, do not present strong optoacoustic efficiency (as it was proved in Section 3.5). Gold nanoparticles, nevertheless, have strong optoacoustic responses due to plasmon resonances; however their long retention times in tissue make them not so easy to accept in clinical studies.

After taking into account the results obtained in Section 3.5, the first outcome of the present chapter is the use of a non-metal nanoparticle composed of organic fluorescent dyes of clinical importance in optoacoustic imaging, yielding stronger optoacoustic signals than the "gold standard", i.e. gold nano-particles. For this goal, clinically-used PEGylated liposomes (the basis of the intravenous drug DOXIL®) were re-engineered and combined with the FDA approved fluorochrome ICG [98]. Liposomes can be designed as drug delivery systems and were used in several fields like clinical medicine [99]. We were particularly interested in knowing the Lipo-ICG distribution within the entire tumor mass in high-resolution, a capacity that has been so far unachievable. Such imaging potential not available before is supposed to have important implications into the validation of nanoparticle distribution *in vivo* and in the development of personalized patient treatment. The Lipo-ICG properties as theranostic contrast agent, its lower photobleaching effect compared to ICG and its higher optoacoustic efficiency, makes this FDA-approved liposomal form a probe to be considered in the RM-MSOT system. Optical microscopy gives an incomplete picture of nano-particle location as it accesses only volumes of about $(0.5 \text{ mm})^3$. In this case, the small field of view achieved does not permit understanding of the capability of an optical nanoparticle to enter the tumor mass. RM-MSOT system shows a critical potential for non-invasively study and longitudinally follow the

distribution of liposomes within tumors. The system was particularly designed, engineered and first explored herein to study the spatial heterogeneity of nanoparticle distribution in tumor tissues. Such imaging capabilities not previously available are thought to have important broader implications into the validation of nanoparticle performance and in the design of patient cohorts for personalized treatment, possibly based on the tumor heterogeneity and particle distribution characteristics on a per patient basis.

In a secondary section, the use of gold nanoparticles as optoacoustic contrast agents in tumor tissue is presented. Gold nanoparticles are a common choice for contrast and therapeutic agents due to their superior optical properties [100–106], biocompatibility, and facility of bioconjugation with biomarkers to build nano-sized contrast agents with molecular specificity [107–109]. The normal approach of creating plasmonic optoacoustic contrast agents is usually done to increase the optical absorption cross-section of nanoparticles by controlling their size and shape, and to select the peak position and the relative amplitude of absorption and scattering cross-sections [110,111]. Gold nanocages, nanoshells and nanorods have shown their properties as characteristic external contrast agents with tunable optical absorption cross-sections [112–115]. In this thesis, AuNR were injected in mice bearing tumors and the distribution of the contrast agents was mapped with the RM-MSOT system in the tumor volume.

The analysis of spatial distribution for the different nanoparticles was achieved along with the visualization of the principal intrinsic contrast agents (HbO_2 and Hb) in order to study vascularization, probe perfusion and extravasation within the tumors. In a similar approach the oxygenation in tumors was studied in mice at different breathing conditions.

4.5.2 Materials and methods

4.5.2.1 Cancer models

All practices involving experimental animals were performed in agreement with German federal law, rules and regulations of Government of Upper Bavaria (ref. 55.2.1.54-2632-102-11). The female 8-week old Athymic Hsd Foxn Nude Mice (Harlan Winkelmann, Germany) used in this work presented neither scattering of sound nor light absorption at the skin surface due to the absence of hair. This mouse line is also immunocompromised and therefore ideal for tumor growth and development. Two tumor models are described in this thesis, one of them representative of rapid growth and based on 4T1 murine breast cancer cells (CRL-2539) [116] and the other using HT-29 human adenocarcinoma cells (ATCC-HTB-38) with slower growing time [117]. The mice were injected subcutaneously in the back with cell suspensions (either 0.8 million for 4T1 cells or 1.5 million for HT29 cells) in 50 μL PBS. The animals were positioned and imaged in the plastic bed fixed to the rotation stage of the RM-MSOT system. The tumor size was approximately of 8-10 mm in diameter at the time of the experiments with the RM-MSOT system.

HT-29 tumor-bearing mice   4T1 tumor-bearing mice
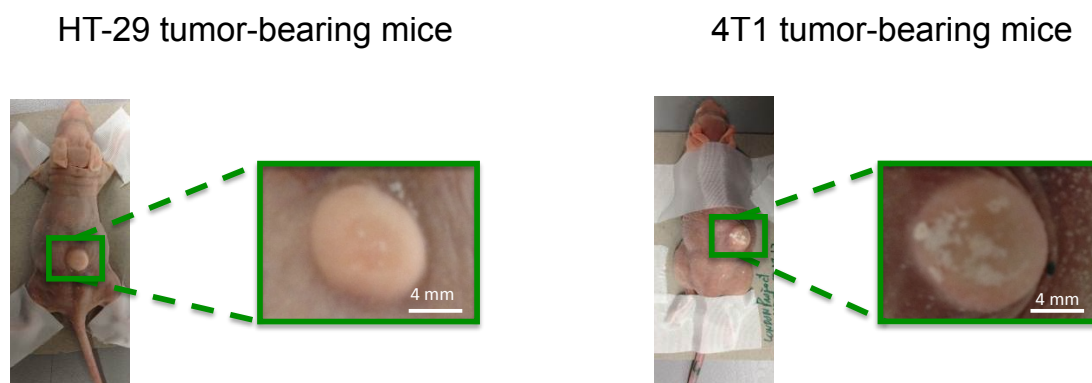
Figure 4.17: Animal tumor models.

4.5.2.2 Probes preparation, injection and imaging protocol

One contrast agent based on the same type of PEGylated liposomes used in DOXIL preparations was made using the vesicle preparation protocol explained in [98]. With a lipid content of 3.5 mM and ICG concentration of 75 µM liposomes (Lipo-ICG), was allowed to self-assemble to create vesicles. Lipo-ICG compound showed higher photo-absorbing behavior than the equivalent free ICG in PBS with an absorption peak at 800 nm. Moreover, a study overtime performed during 5 days showed that after the 1 day the peak absorbance of free ICG decreased sharphly while the signal for the Lipo-ICG remained almost constant after the total period.

Optoacoustic images of the tumors (4T1 and HT29) were acquired with the RM-MSOT system at different time points (1 h, 5 h and 24 h) *ex vivo* or after intravascular tail-vein injection of 200 µL of Lipo-ICG corresponding to a sum of ~ 15 nmol of ICG.

For the experiments with AuNR, bearing 4T1 tumor allografts were used. The tumor carrying mice were injected in the tail vein (i.v.) 1 hour before the optoacoustic imaging session with 5×10^{12} AuNR 30-PM-750-50 (Nanopartz, Loveland, Colorado, USA). The optical absorption peak of the probe was 720 nm.

4.5.2.3 Animal positioning and anesthesia in the RM-MSOT system

For the experiments with tumors in mice, the animals were positioned on a plastic bed fixed to the rotation stage (Figure 4.18 A). The bed had a hole in the middle to ensure proper tumor positioning and enable contact with water as an acoustic coupling medium. The tumor was illuminated by the four arms of the fiber bundle at the correct focal distance from the transducer (Figure 4.18 B).
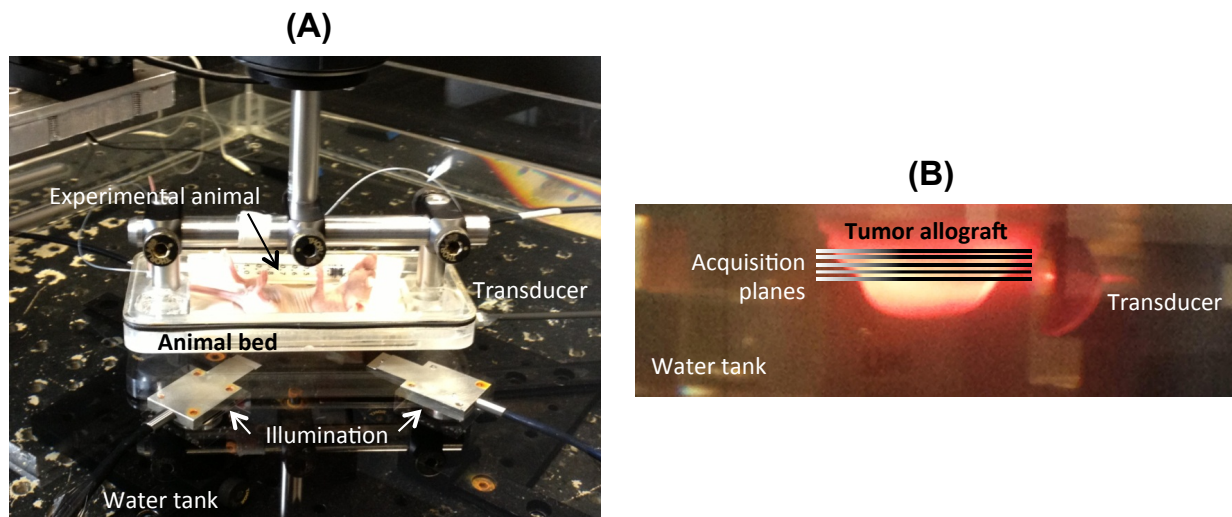
Figure 4.18: Mice positioning for tumor imaging. (A) RM-MSOT system with plastic bed. The animals are rotated in the plastic bed around the fixed illumination sources and transducer with the tumors inside the water tank to provide acoustic coupling medium. (B) Illuminated tumor allograft and PNDT V319 transducer with approximated imaging acquisition planes.

experiments in mice were performed with either injected or breathed anesthesia. In the first case, doses with of a mix of Ketamine (Bela-pharm GmbH & Co. KG, Vechta, Germany) 100 mg/kg body weight and 5 mg/kg body weigth Xylazine (Bayern Healthcare GmbH, Leverkusen, Germany) were administered. In the second option, an anesthetic system that enriches medical air (20 % O_2) or 100 % O_2 with Isoflurane 1.8 % was used (Figure 4.19 A). The concentration of Isoflurane was administered using a PPV$_\Sigma$ vaporizer (Penlon, Abingdon, England) and the levels of the gases were controlled by different flow meters. After the vaporizer, the narcosis gas was distributed through hoses and valves to a mouse breathing mask or to a narcosis box independently. A vacuum pump ensured continuous flow of the narcosis gas without emissions to the free air, and a coal filter absorbed it as last step. The mouse-breathing mask was fixed in the bed and the anesthetic gas was administered through a self-developed part that enables the flow from a static hose to another hose fixed to the mask (Figure 4.19 B).

(A) **(B)**
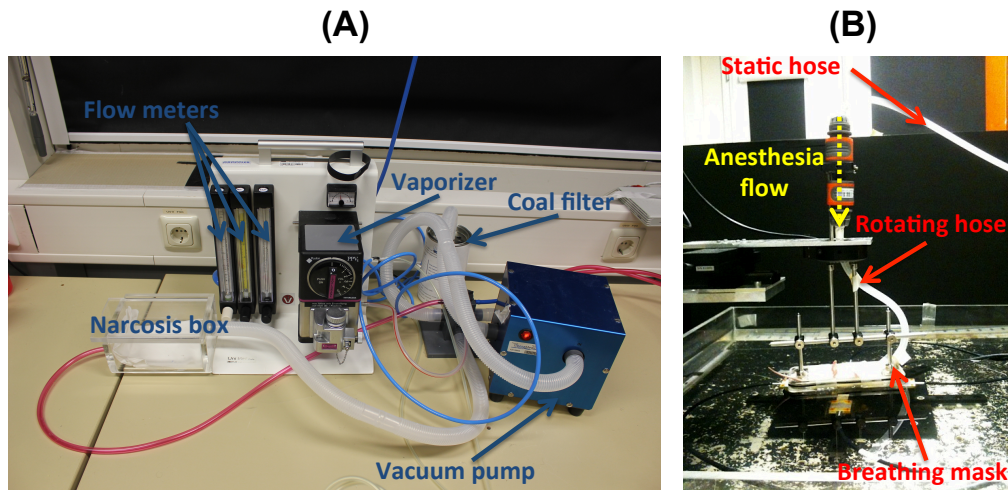
Figure 4.19: Devices used to provide Isoflurane to the RM-MSOT. (A) Anesthetic machine components. (B) Anesthesia flow mechanism to the breathing mask in the rotation stage.

4.5.2.4 Histological validation of tumors

To validate *in vivo* experiments, the animals were sacrificed by Ketamine/Xylazine overdose inmediately after the optoacoustic imaging session, and frozen to -80°C for storage until analysis was performed. Fluorescence cryosection imaging (FCSI) was done *ex vivo* in coronal planes equivalent to the optoacoustic imaging slices on the studied tumors every 150 μm from top towards the animal body after embedding them in optimal cutting temperature media (Sakura Finitek Europe B. V., Zoeterwonde, NL). To confirm the presence of Lipo-ICG, color and fluorescence images were captured, using a RGB-filter set (Chroma xxx) for the reflection images and a pair of 740/40 (Chroma Technology Corporation, Bellow Falls, USA) and 785LP by the same company for the excitation and emission of ICG respectively. The FCSI system reported elsewhere [118] was based on a cryotome (CM 1950, Leica Microsystems, Wetzlar, Germany), which was equipped with a NIR sensitive electron multiplying charge-coupled device (EMCCD) Luca-R (Andor, Belfast, Northern Ireland), a white light source KL2500LCD (Schott, Mainz, Germany) and 2 filter-wheels, both for the excitation and emission paths.

20 μm thick cryo-slices in representative planes were obtained and imaged by an epi-illumination fluorescence system based on a Leica Z16 macroscopic lens. In the case of AuNR detection, the Leica Z16 fluorescent microscope was used with dark field setup. Further sections were stained by conventional H&E as described in [119]. Immunohistochemistry was done on frozen sections by using antibodies against CD31 (Dianova GmbH, Hamburg, Germany) a marker for blood vessel endothelia. The antibody reaction was visualized with Alexa 594-conjugated secondary antibody (Invitrogen, Darmstadt, Germany). The negative controls were performed with adjacent sections treated in the same way, but with omitted primary antibody. H&E as well as CD31 stained slices were imaged with a Leica DM 2500 upright microscope using a Leica EC3 color camera (Leica Microsystems, Wetzlar, Germany).

4.5.3 Results

4.5.3.1 *Ex vivo* imaging of tumors with high resolution

In a first step, the spatial distribution of Lipo-ICG as external vascular probe was studied *ex vivo* to see the capacity of the RM-MSOT system to get 3D rendering of detailed extravasation and microenvironment profiles within solid tumors. The mouse with subcutaneous 4T1 murine breast tumor was scanned directly after euthanasia at the peak wavelength of Lipo-ICG (800 nm) along the Z-axis with a step of 50 μm between consecutive slices. Figure 4.20 illustrates the 3D anatomic reconstruction of the peak wavelength for Lipo-ICG in this tumor. Optoacoustic images were acquired every 50 μm along the Z-axis after applying a bandpass filter between 0.1 and 20 MHz to the signals. The given 2D image stack (Figure 4.20 A) was rendered to get the 3D map of Lipo-ICG distribution inside

and around the solid breast tumor (Figure 4.20 B). The Lipo-ICG signal was found in the tumor periphery as well as in its interior. The last result was validated with a 3D reconstruction of a serial cryo-slicing image stack for Lipo-ICG signal (Figure 4.20 C). The distribution of the contrast agent rendered with the RM-MSOT system matched that obtained with cryo-slicing images, showing concentration of the agent in the center of the tumor on this level (asterisk) and some blood vessels in the boundary (arrow). It can be noticed that the optoacoustic images revealed more details and yielded clear pictures for the tumor part adjacent to the rest of the body, also visualizing vasculature around the tumor.
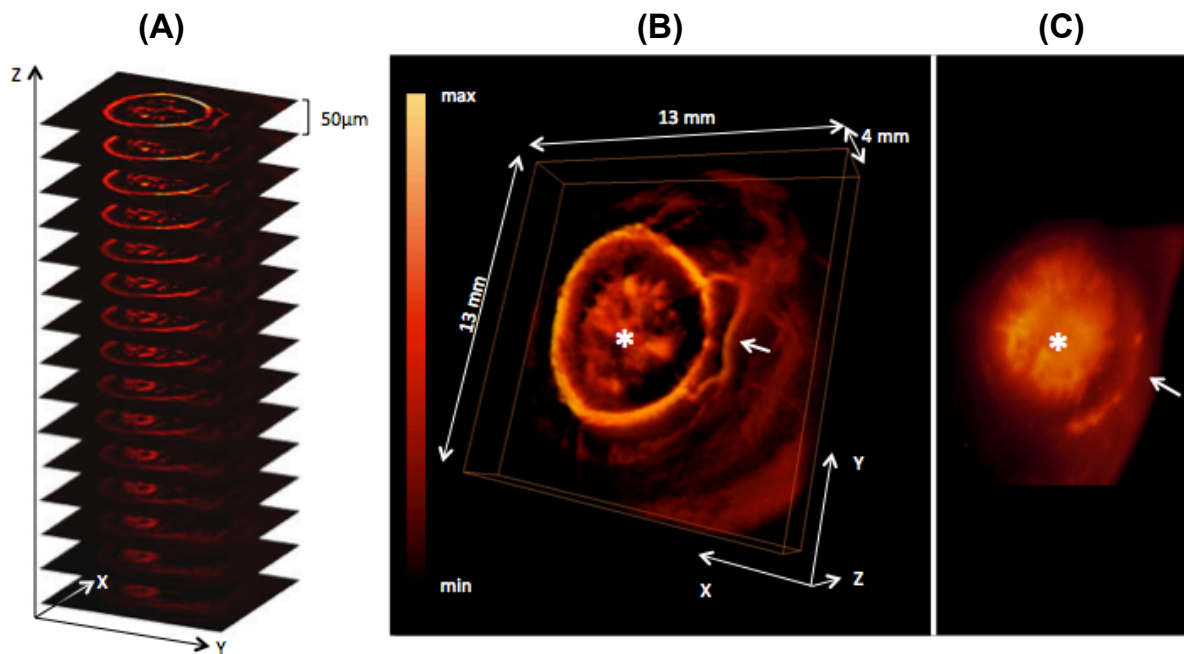
Figure 4.20: Ex vivo Lipo-ICG spatial distribution in a 4T1 tumor. (A) Stack of optoacoustic images in the XY-plane acquired at 800 nm every 50 μm along the Z-axis. (B) 3D rendering of the distal tumor part, which shows Lipo-ICG distribution inside and in the periphery around the 4T1 tumor allograft. The color bar displays the level of Lipo-ICG optoacoustic signal in arbitrary units (a.u.). (C) 3D rendering validation made of serial cryo-slicing epi fluorescence images for Lipo-ICG in the same tumor as imaged by mesoscopy MSOT in B. The inner signal appears in both validation and optoacoustic 3D reconstruction (asterisk) and also in some peripheral vessel (arrow).

The result after applying to each of the 4000 projections of the same 4T1 tumor different bandpass filters is shown in Figure 4.21. The results showcase that most of the information was contained in lower frequencies.
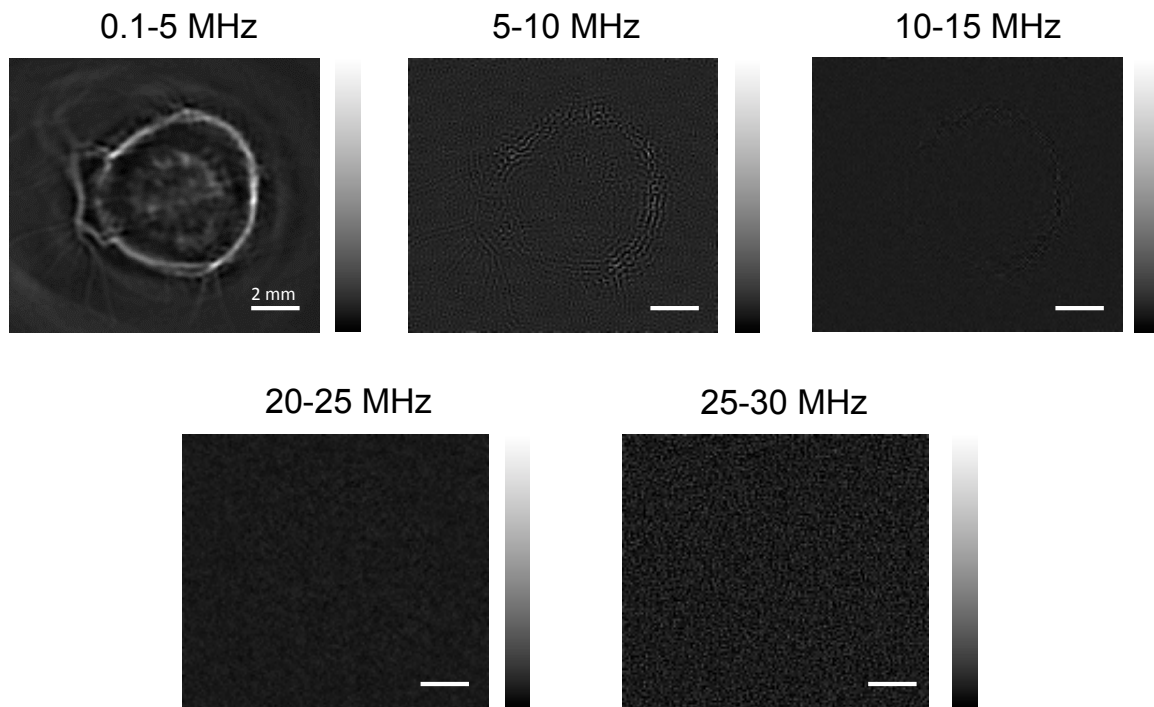
Figure 4.21: Optoacoustic *ex vivo* 4T1 tumor images with different filters.

4.5.3.2 *In vivo* imaging of Lipo-ICG in heterogenic solid tumors

To show the Lipo-ICG kinetics of particles distribution, the two different animal tumor models (HT29 and 4T1) were each scanned at different time points. After injecting intravenously Lipo-ICG, the mice were positioned in the plastic bed and slices were acquired at 1, 5 and 24 hours, displaying the tumor microenvironment at a high resolution [98].

In Figure 4.22 C (i and vi), coronal slices through the 4T1 and HT29 tumors respectively obtained at the illumination wavelength of 800 nm are displayed, providing high-resolution anatomical views of the tumors. The results reveal a reach vascular pattern in the core of 4T1 tumor, although an avascular part in the

tumor periphery is to be noted, as also proved in the rendered 3-D reconstruction on Figure 4.22 B. The image stack that had created the 3-D reconstruction is given in Figure 4.22 A with a vertical step of 250 μm between slices. Compared to the 4T1 tumor, the HT29 provides another appearance with large peripheral vessels but less vascular density in its core. With the multispectral capabilities of RM-MSOT system, the recognition of Lipo-ICG based on its absorption signature, could be achieved at high resolution.

In Figure 4.22 C (ii-iv) the images of Lipo-ICG distribution in the 4T1 tumor at 1 h, 5 h and 24 h time points are given after linear fitting unmixing. The results reveal a specific distribution of the Lipo-ICG over time in the central part of the tumor, which by the 5 h time point has taken a large portion of the vascular pattern (Figure 4.22(ii)). However, there is a characteristic absence of Lipo-ICG in the avascular part of the tumor. This pattern is validated by the fluorescence cryosection in Figure 4.22 C (v) and consistent with the already-mention optoacoustic images.

In Figure 4.22 C (vi-ix) the analogous measurements from the HT29 tumor model are shown. Compared to the 4T1 model reconstructions, the displayed Lipo-ICG distribution present a limited extravasation in this type of tumor even after 24 h, as also confirmed with the HT29 fluorescence cryoslice images (Figure 4.22 C (x)). The results permit understandings not only the Lipo-ICG distribution but also the spatial heterogeneity of tumors, showing lower vessel density and permeability for the HT29 tumor vs the 4T1 tumor. Figure 4.22 C (x) has been scaled with a higher gain than the one in Figure 4.22 C (v) so the intensities are not comparable in these two images.
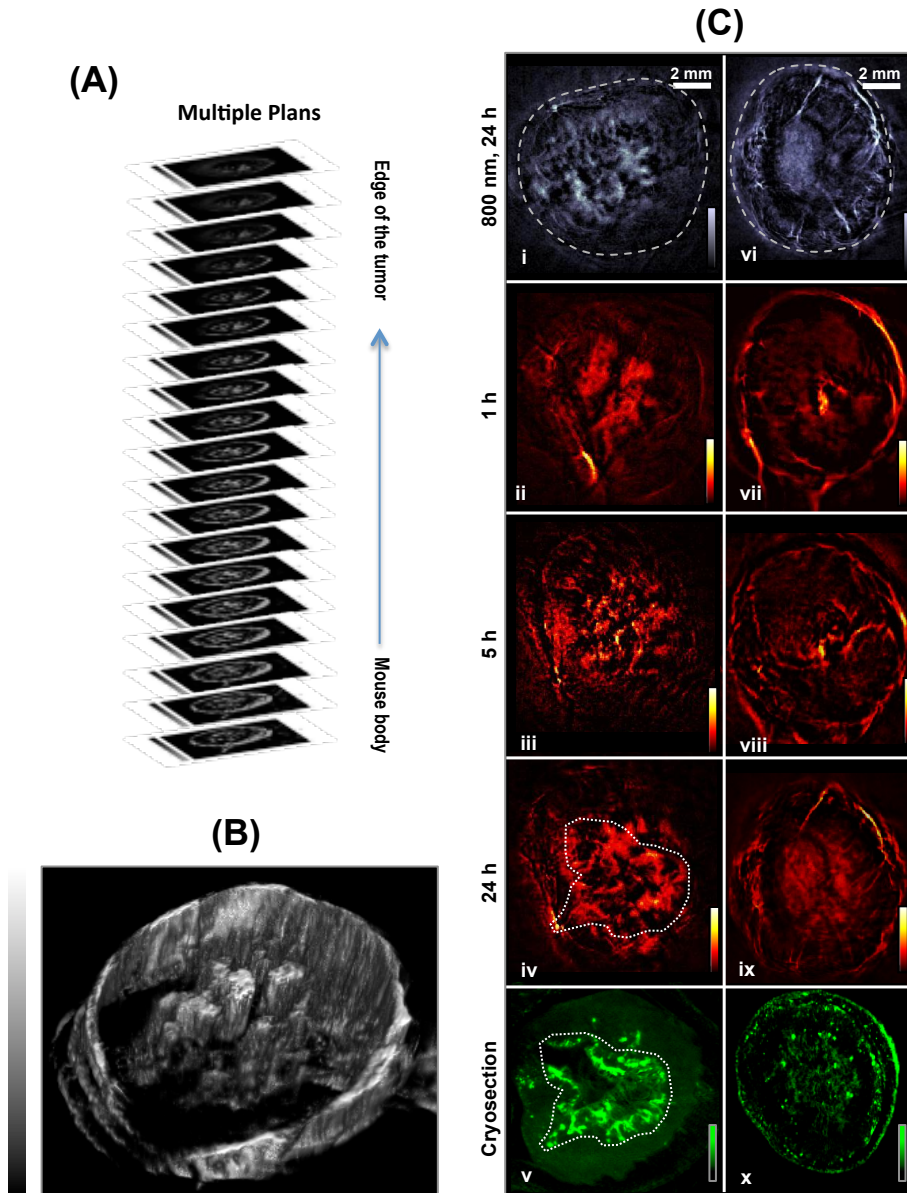
Figure 4.22: Kinetics of accumulation of Lipo-ICG in 4T1 and HT29 tumor models at different time points. (A) Optoacoustic stack of images from a 4T1 tumor with a step of 250 μm between slices along the Z-axis and 800 nm as illumination wavelength. **(B)** 3-D reconstruction created with the images in A cut by an angle plane. **(C i)** Optoacoustic coronal plane image of a 4T1 tumor, acquired at 800 nm illumination wavelength, 24 h after injection of the contrast agent. **(C ii-iv)** Lipo-ICG signal after unmixing the same tumor 1 h, 5 h, and 24 h after injection. **(C v)** Fluorescence from Lipo-ICG (green scale) acquired from a thin slice of the 4T1 tumor, 24 h after injection. The tumor boundaries are outlined. **(C vi-x)** The same layout is used to display images of a HT29 tumor.

Figure 4.23 shows optoacoustic images of another 4T1 tumor allograft *in vivo* in a coronal plane 1 h after administration of Lipo-ICG. Upon multispectral optoacoustic acquisition at 700, 720, 770, 800, 830 and 860 nm as illumination wavelengths, the specific contrast agent signal was spectrally resolved with linear fitting. The unmixed image displays such signal indicating Lipo-ICG distribution mainly in the tumor periphery. However, a certain quantity was also detectable inside the tumor, likely due to extravasation of the probe from the tumor vasculature. As it was displayed, the intrinsic properties of the RM-MSOT system allow the acquisition of anatomical and functional information in the same experimental set as indicated in the same figure (image at the peak wavelength of Lipo-ICG and unmixing of the same contrast agent). For the least square linear fitting unmixing, it is assumed that the spectra at different points in the image is a linear combination of the extinction coefficients of oxygenated and deoxygenated hemoglobin and the probe. However, variations in the laser energy and light attenuation as a function of wavelength hamper proper unmixing, and typically cross-talk appears in the unmixed images. In this way, blood structures (representing the anatomy) can be projected onto the unmixed image of the probe. This limits the sensitivity of the method. Correction of this effect is a long-standing challenge as it requires accurate modeling and very careful control on the experimental procedure, and is out of the scope of this thesis.
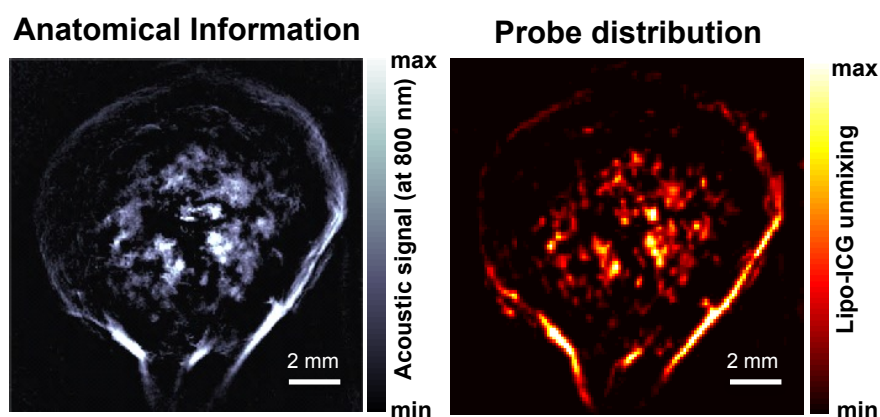
Figure 4.23: Optoacoustic images of a 4T1 tumor after 1 hour injection of Lipo-ICG *in vivo*. Left) Optoacoustic image at the peak wavelength of Lipo-ICG (800 nm) obtained with back-projection with negative values set to zero. (Right) Unmixing with spectral fitting of Lipo-ICG.

To better understand *in vivo* experiments with the RM-MSOT system, a histological study of some 4T1 tumor sections is shown in Figure 4.24. H&E staining was used to give an overview of the properties of tissue at this tumor level and cell viability. The distribution of Lipo-ICG was confirmed by epifluorescence image, showing the brightest signal where the probe was located. CD-31 staining was also performed to assess tumor vasculature. In Figure 4.24 A the reconstitution of complete tumor slices stained with H&E is shown. They were acquired from two 4T1 tumors harvested at 1 h and 24 h post injection. At the same tumor level epifluorescence images were taken also in both tumors, showing the extravasation of Lipo-ICG moving from the highly vascularized outer boundaries to the inner core. Figure 4.24 B displays in higher resolution H&E, CD31 and fluorescence microscopy images at 800-830 nm (Lipo-ICG signal) from the areas marked with the three boxes on Figure 4.24 A. Results from both tumors obtained at 1 h and 24 h post injection are displayed. CD31 staining overall confirmed the differences in tumor vascularization according to the RM-MSOT system experiments. 1 h after injection, Lipo-ICG is present in the tumor vasculature. The signal is not visible at 24 h (Figure 4.24 B (iv)). On the other

hand, Lipo-ICG signal from the tumor core raises from 1 h to 24 h as seen comparing Figure 4.24 B (iii) and Figure 4.24 B (vi).

(A)

(B)
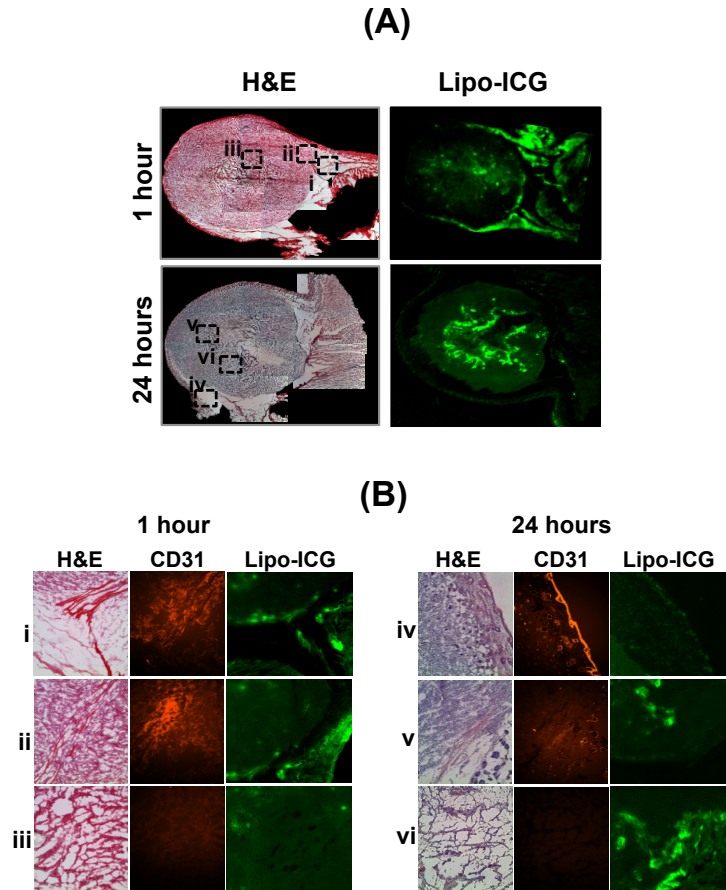
Figure 4.24: Ex vivo histology study of Lipo-ICG extravasation in 4T1 tumor model. Reconstitution of H&E staining and epifluorescence images of 4T1 tumor slices 1 hour (top) and 24 h (bottom) after injection of lipo-ICG. (B) H&E (color channel), CD31 (red channel) and Lipo-ICG (green channel) microscopy pictures of various locations of the tumor presented in (A), i-iii for 1 h after Lipo-ICG injection (left) and iv-vi for 24 h after Lipo-ICG injection (right).

4.5.3.3 *In vivo* imaging of gold nanoparticles and intrinsic functional contrast

In a similar approach as in the Lipo-ICG imaging experiments, the specific AuNR signal after multispectral acquisition was determined in the tumor region. In Figure 4.25 A top, the optical spectrum for the AuNR used is shown. The optoacoustic spectrum was equivalent. In Figure 4.25 A botton, an anatomical image of the studied 4T1 allograft at 800 nm with superimposed specific AuNR distribution profile is displayed. The AuNR signal was found mainly in blood vessels (arrows) and commenced to emerge in the tumor periphery major vessels (box 2) in the vicinity of the rest of the body. Figure 4.25 B shows the validation of AuNR optoacoustic signal rich distribution areas with the CD31 blood vessel staining marker in the studied tumor. It is demonstrated that AuNR started to be located in the region adjacent to the rest of the body with higher concentration in blood vessels (see Figure 4.25 A and B, box 2 compared to the box 1). Dark field was performed, showing the presence of AuNR where the optoacoustic specific signal was also detected by MSOT (Figure 4.25 C, DF1). In the region with non-visible AuNR signal in MSOT, the probe was also not present on the validation experiment (Figure 4.25 C, DF2). The histological overview of the tumor was implement with H&E staining (Figure 4.25 C).

As one of the principal advantages of MSOT, the capability of the system to image the distribution and at the same time co-registration of intrinsic and external contrast signals in the same experimental data set is showcased. As dominant intrinsic contrast agents in tissue, MSOT imaging with tumor-bearing mice permits spectral resolution of HbO_2 and Hb *in vivo*. Figure 4.25 D confirms the co-registration of HbO_2 and Hb heterogenic distribution profiles in the tumor, contributed by differentially oxygenated blood in the periphery and in the inner part of the tumor. The spectrum in the regions of interest with mostly oxygenated and deoxygenated blood was additionally evaluated in Figure 4.25 D, (ROI 1 and

2). In these regions, the spectra was calculated locally (black line) and compared to the theoretical spectra for HbO2 (red) and Hb (blue).

As a last step, the distribution of AuNR in the tumor was shown (Figure 4.25 E) and compared with the ones for HbO_2 and Hb. 1 h after the injection of AuNR, the main proportion of AuNR signal was found to rather match with HbO_2 component (Figure 4.25 F), but not with the Hb one (Figure 4.25 G). This result denoted that at this time point, the external contrast agent was probably localized in the arterial vasculature, but not in the venous one containing Hb as a principal absorption component. The extravasation of AuNR only began into the tumor mass.
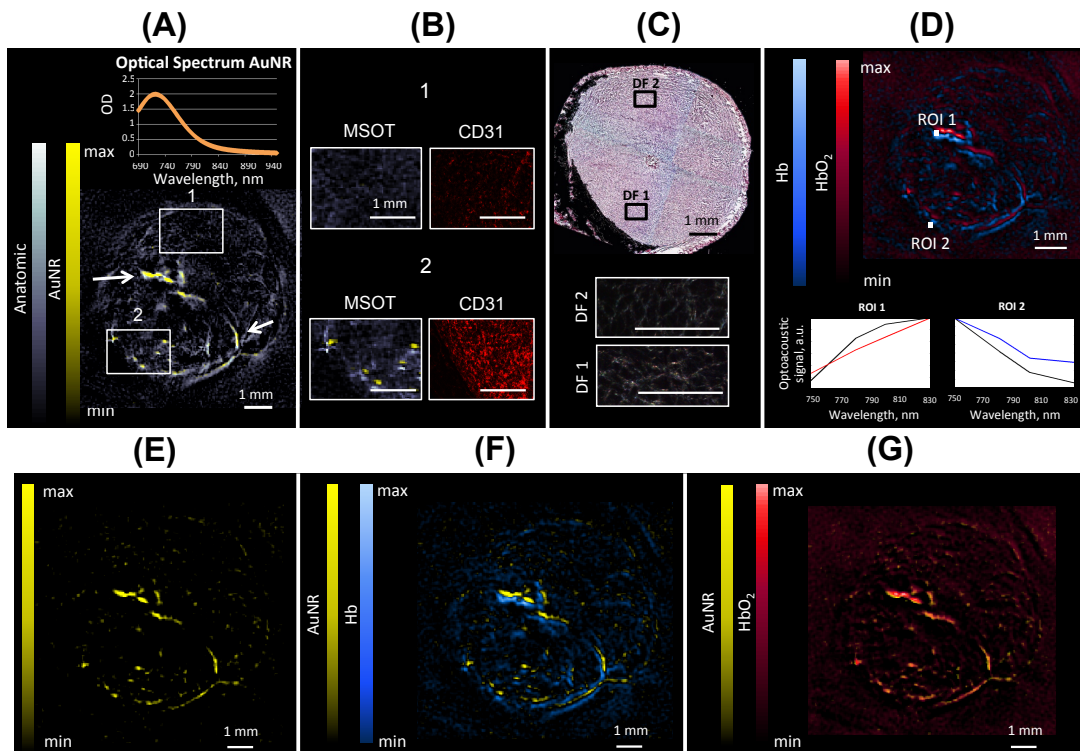
Figure 4.25: RM-MSOT system imaging and validation of AuNR and blood oxygenation spatial distribution in 4T1 breast tumor allograft. (A) Optical spectrum for AuNR (top) and specific signals (yellow) multispectrally resolved, superimposed with anatomic image (grey) at 720 nm illumination wavelength (peak of AuNR) (botton). The AuNR signal was located mainly in blood vessels (arrows). Regions 1 and 2 were used to validate in B. (B) CD-31 immunohistochemical staining as a blood vessel marker shows that AuNR was concentrated in tareas with higher number of blood vessels. (C) H&E staining for tumor histological profile. DF1 and DF2: regions with and without AuNR contrast agent respectively. Small boxes: dark field microscopy profiles with AuNR map. Scale bars: 50 μm. (D) Optoacoustic profiles for Hb and HbO_2. Small boxes: Graphs for spectral characteristics measured in the ROIs containing mostly HbO_2 and Hb components. The black curves on the graphs indicate the calculated spectra in each of the ROIs. They are compared to the theoretical spectra: HbO_2 (red) and Hb (blue). (E) Specific signal for AuNR after multispectral unmixing. (F) Specific signals for AuNR and Hb were spectrally resolved, but could not be co-localized. (G) Specific signals for AuNR and HbO_2 were spectrally resolved and could be co-localized confirming AuNR to be located mostly in arterial blood vessels 1 h after i.v. injection.

4.5.3.4 Tumor oxygenation at different breathing conditions

In this experiment, a 4T1 tumor was imaged in three different conditions (same Z-plane) with different percentages of O_2 in the breathing gas. The animal was anesthetized in the first two scans with Isoflurane as explained in 4.5.2.3, initially with medical air (20 % O_2) and then with 100 % O_2. Finally, the mouse was sacrificed with a mixture of Ketamine/Xylazine and the last scan was performed. The three scans were separated by 10 minutes in order for the tissue to stabilize with the new conditions. A color image taken with the cryoslicer at approximately the same coronal optoacoustic slice is shown (Figure 4.26 A). After multi-wavelength acquisition data (710, 730, 760, 800, 830 and 850 nm), back-projection reconstruction of the different wavelengths signals and linear fitting was performed. The principal endogenous contrast agents (HbO_2 in red and Hb in blue) were unmixed in the tumor (Figure 4.26 B). As expected, the oxygenation maps were not the same for the three scans. The higher amount of HbO_2 was found while breathing 100 % O_2, whereas no HbO_2 was detected in the dead mouse.

(A)

(B)

20 % oxygen   100 % oxygen   dead
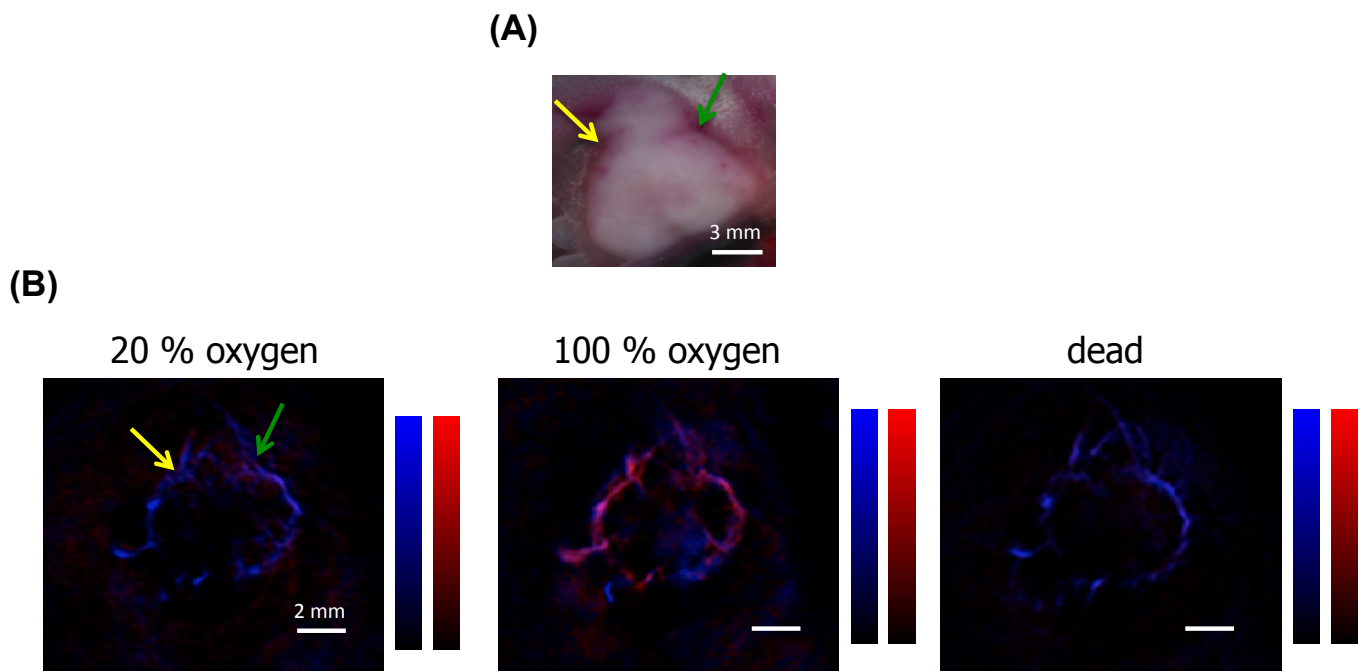
Figure 4.26: Tumor oxygenation varying the breathing conditions. (A) Color image while cryoslicing at the same tumor level than the optoacoustic reconstructions in B. The arrows indicate similar structures in both cases. (B) Optoacoustic reconstruction unmixing after linear fitting with HbO$_2$ (red) and Hb (blue).

4.5.4 Discussion

In this chapter, we have shown that the RM-MSOT system provides high-fidelity images of heterogenic solid tumor models (4T1 and HT29) *in vivo* and *ex vivo* in mice. This system has typical MSOT advantages such as the capacity to simultaneously acquire anatomical and molecular data in an experimental data set with co-registration of different contrast agents. Then, it meets the demand for the analysis of microenvironment gradients deep in solid preclinical tumor models. The superior resolution combined with sustained competitive imaging depth is critical to understand tumor heterogeneity and functional properties during tumor development and anticancer therapy.

Two different probes (Lipo-ICG and AuNR) were injected in mice and mapped within the tumors to show the ability of the system to differentiate external contrast agents from the rest of tissue structures. Mapping Lipo-ICG in heterogeneous solid tumors revealed a detailed probe biodistribution pattern as well as the capacity for 3D imaging as a complementary tool to standard MSOT. Moreover, the RM-MSOT system provided kinetic location of the external contrast agent at different time points. In the same way, the RM-MSOT system could resolve and analyze *in vivo* specific signals for AuNR contrast agent upon multiple wavelength acquisition with high resolution. Clear similarities were found between optoacoustic and validation profiles in *ex vivo* slicing for both probes.

Also important is the high resolution imaging capacity of intrinsic contrast, namely Hb and HbO2, which is indicative of hypoxia and tumor perfusion heterogeneity. In this way, other important pathophysiological gradients can be defined. In order to prove the reliability of the RM-MSOT system to resolve Hb and HbO2, several regions of interest in the tumors were experimentally compared and resolved with theoretical spectra. This analysis revealed correlation, demonstrating that the RM-MlSOT system yielded a real map of the intrinsic contrast components *in vivo*. Both endogenous contrasts were studied also under different breathing condition.

5 Conclusions and outlook

5.1 Conclusions

In this thesis we aimed at a two-fold objective for important improvements of MSOT in practical scenarios. In a first step, we discussed the concept of efficiency of probes, which can serve as a guide for probe selection in molecular imaging. In a second and principal objective, we developed a mesoscopic optoacoustic system for high-resolution visualization of tumors in preclinical experiments and showcased important applications in cancer research.

The importance of choosing an efficient probe was studied with a macroscopic optoacoustic system for small animals. Phantom experiments were performed to study the efficiency of gold nanoparticles and fluorescent dyes. The importance of the quantum yield of dyes was noted in the reduction of efficiency. Photobleaching effects were also analyzed and ICG was shown to be more affected by this effect than other dyes. An optoacoustic spectrometer was also developed to study the spectrum of optoacoustic signals. The performance of this system was showcased with oxygen saturation measurements in blood, which were comparable to the repective measurements obtained with a gas analyzer.

The principal outcome of this thesis was the creation of a rotational mesoscopic optoacoustic system (RM-MSOT) for the visualization of heterogenic solid tumors in preclinical studies. The reconstructed tomographic data provided high-fidelity images with an in-plane resolution of 50 μm and penetration depths beyond 15 mm when using a piezoelectric cylindrically-focused immersion transducer with 15 MHz central frequency. Different reconstruction algorithms were explored in the thesis, where a tradeoff generally exists between image quality and computation time. The system has typical MSOT advantages, such us the ability to simultaneously acquire anatomical and molecular information in the same data set with seamless co-registration at different optical wavelengths.

The characterization of the RM-MSOT system was achieved with different phantoms and *ex vivo* and *in vivo* studies were performed in mice with two tumor models. The 4T1 breast cancer cell line results in a fast growing tumor with leaky vasculature and the HT29 colon carcinoma model presents slower growth and a restricted microvascular network. The 4T1 tumor shows a rich vascular outline in its core, but an avascular pattern in the tumor periphery. The shape of HT29 tumor is different, displaying large peripheral vessels and less vascular density in its core.

The major advantages of the RM-MSOT system technology were highlighted with the detailed *in vivo* and *ex vivo* imaging of external and intrinsic contrast agent concentrations in preclinical models of breast cancer. The capacities of the system to image the spatial distribution of injected probes in slices of the tumors *in vivo* was showcased, and volumetric imaging was also achieved by stacking the two-dimensional cross-section. High-resolution with competitive imaging depth is important in the research of tumor heterogeneity and functional properties during tumor formation and anticancer therapy. The probe distribution images rendered by the RM-MSOT system could be co-registered with the anatomical ones and correlated with the validation *ex vivo* images, demonstrating the reliability of the setup.

The performance of the RM-MSOT system in imaging the bio-distribution of two important contrast agents, namely liposomal ICG and gold nanorods, was showcased. Liposomes are known as the most common vehicle currently used for targeted drug delivery. The liposomes employed enable observations of enhanced permeation and retention with the RM-MSOT system. The optoacoustic setup offered a detailed view of the particle distribution within tumors and a marked variation on the delivery ability in the two different tumor models. Detection of Lipo-ICG based on its absorption signature was performed at different time points. Shortly after injection, Lipo-ICG stayed limited to the vascular system and did not distribute within other tissues or deoxygenated regions of limited blood supply. In later time points, the concentration of the liposomes in the center of the 4T1 tumor was detected with a corresponding decrease of visible signal in the surrounding vasculature. The results were different in the HT29 tumor model. Lipo-ICG did not appear in the tumor core and persisted in the tumor peripheral vasculature. The results were confirmed also with epi-fluorescent illumination. The distribution of AuNR in 4T tumors was also resolved with the RM-MSOT system *in vivo* upon multiple wavelength acquisition and validated with dark field imaging. The AuNR signal was resolved primarily in blood vessels and started to appear in the tumor periphery major vessels.

Imaging of intrinsic contrast agents like Hb and HbO_2, was also achieved in the same setup. The maps of these components represent an indicative sign of hypoxia and tumor perfusion heterogeneity and define also other important pathophysiological gradients. To demonstrate the consistency of the RM-MSOT system to resolve Hb and HbO_2, regions of interest were selected in the studied tumors and compared to the theoretical spectra. Co-localization of AuNR with HbO_2 demonstrated high-resolution multichannel imaging and probe distribution shortly after injection. Experiments using breathing air at different oxygen levels also demonstrate similar results in regions of interest marked in the tumors.

The reported RM-MSOT system proved the high potential for studying heterogeneous vasculature, blood oxygenation and pathophysiological profiles as a function of tumor microenvironment at any stage of tumor development, using its multispectral imaging capacity to compare and co-localize external and intrinsic contrast agents. The setup may find application as a valuable preclinical tool for studying the pathophysiology of tumors and their response to treatment using specific contrast agents and internal microenvironment gradients.

5.2 Outlook

One of the challenges of the RM-MSOT system is to reduce the required acquisition time to obtain a stack of 2-D image slices and to perform a measurement at multiple wavelengths. The first is necessary when a higher number of optoacoustic planes are required for a better vertical resolution. The second is needed to estimate (unmix) the spatial distribution of endogenous or exogenous contrast agents, which generally changes with time. A possible solution to this problem is to increase the number of single element transducers around the sample or to use arrays of detectors covering a wider angle of view. Another solution is to increase the rotation speed, which may come to the detriment of image quality unless the pulse repetition rate of the laser is also increased.

Other setups based on scanning the transducer(s) instead of the sample can also be explored, where gas anesthesia can be more efficiently provided but problems arise due to the need of scanning the optical illumination elements. Cylindrically-focused transducers with higher frequencies can also be characterized and used for tumor imaging in the RM-MSOT system. However, detectors with wider element diameter or tighter focus present more difficulties to scan around the tumors due to the proximity of the animal body.

Considering that a significant number of projections are needed to create images from the samples, new memory-efficient reconstruction algorithms must be explored in future work. Various filters highlighting the particular structures of tissue can be also used for image quality enhancement, and further studies for the automatic selection of the speed of sound in tissue as a basic step of image reconstruction can also be helpful.

References

1.   Bell, A.G., Selenium and the Photophone. Nature, 1880. 22: p. 500-503.
2.   Bell, A.G., Upon the production of sound by radiant energy. Philosophical Magazine Series 5, 1881. 11(71): p. 510-528.
3.   The Manufacturer and Builder. 1881. p. 156.
4.   Tyndal, J. in Proc. Roy. Soc. (London) 1881.
5.   Veingerov, M.L., New Method of Gas Analysis Based on Tyndall-Roentgen Opto-Acoustic Effect. 1938. 19: p. 687.
6.   Maiman, T., Stimulated Optical Radiation in Ruby. Nature, 6 August 1960. 187: p. 493–494.
7.   Patel, C.K., E.G. Burkhardt, and C.A. Lambert, Spectroscopic measurements of stratospheric nitric oxide and water vapor. Science, 1974. 184(4142): p. 1173-6.
8.   Angelsen, B., Ultrasound Imaging: Waves, Signals, and Signal Processing. 2000.
9.   Inc., O.N., Panametrics Ultrasonic Transducers. 2009: Waltham, MA 02453 USA.
10.   Wang, L.V. and H.-i. Wu, Biomedical optics : principles and imaging. 2007, Hoboken, N.J.: Wiley-Interscience. xiv, 362 p.
11.   Wang, L.V., Tutorial on photoacoustic microscopy and computed tomography. Ieee Journal of Selected Topics in Quantum Electronics, 2008. 14(1): p. 171-179.
12.   V. Z. Gusev, A.A.K., Laser Optoacoustics November 1, 1992: American Institute of Physics.
13.   Wang, L.V., Photoacoustic imaging and spectroscopy. Optical science and engineering. 2009, Boca Raton: CRC. xx, 499 p.
14.   Cox, B.T., et al., k-space propagation models for acoustically heterogeneous media: Application to biomedical photoacoustics. Journal of the Acoustical Society of America, 2007. 121(6): p. 3453-3464.
15.   Xu, M.H. and L.H.V. Wang, Photoacoustic imaging in biomedicine. Review of Scientific Instruments, 2006. 77(4).
16.   Beard, P., Biomedical photoacoustic imaging. Interface Focus, 2011. 1(4): p. 602-631.
17.   Lutzweiler, C. and D. Razansky, Optoacoustic Imaging and Tomography: Reconstruction Approaches and Outstanding Challenges in Image Performance and Quantification. Sensors, 2013. 13(6): p. 7345-7384.
18.   Kruger, R.A., et al., Thermoacoustic CT with radio waves: a medical imaging paradigm. Radiology, 1999. 211(1): p. 275-8.

19. Ntziachristos, V. and D. Razansky, Molecular Imaging by Means of Multispectral Optoacoustic Tomography (MSOT). Chemical Reviews, 2010. 110(5): p. 2783-2794.

20. Kim, C., C. Favazza, and L.H.V. Wang, In Vivo Photoacoustic Tomography of Chemicals: High-Resolution Functional and Molecular Optical Imaging at New Depths. Chemical Reviews, 2010. 110(5): p. 2756-2782.

21. Tzoumas, S., et al., Unmixing Molecular Agents From Absorbing Tissue in Multispectral Optoacoustic Tomography. Ieee Transactions on Medical Imaging, 2014. 33(1): p. 48-60.

22. Luke, G.P. and S.Y. Emelianov, Optimization of in vivo spectroscopic photoacoustic imaging by smart optical wavelength selection. Optics Letters, 2014. 39(7): p. 2214-2217.

23. Razansky, D., C. Vinegoni, and V. Ntziachristos, Multispectral photoacoustic imaging of fluorochromes in small animals. Optics letters, 2007. 32(19): p. 2891-2893.

24. Van Veen, R.L.P.S., H.J.; Pifferi, A.; Torricelli, A.; Cubeddu, R., Determination of VIS-NIR Absorption Coefficients of Mammalian Fat, with Time- and Spatially Resolved Diffuse Reflectance and Transmission Spectroscopy., in Proceedings of the Biomedical Topical Meeting. 2004: Miami Beach, FL, USA.

25. Wang, L.V., Multiscale photoacoustic microscopy and computed tomography. Nature Photonics, 2009. 3(9): p. 503-509.

26. Wang, L.H.V. and S. Hu, Photoacoustic Tomography: In Vivo Imaging from Organelles to Organs. Science, 2012. 335(6075): p. 1458-1462.

27. Hoelen, C.G. and F.F. de Mul, Image reconstruction for photoacoustic scanning of tissue structures. Appl Opt, 2000. 39(31): p. 5872-83.

28. Xu, M.H. and L.H.V. Wang, Universal back-projection algorithm for photoacoustic computed tomography. Physical Review E, 2005. 71(1).

29. Wang, X., et al., Photoacoustic tomography of biological tissues with high cross-section resolution: reconstruction and experiment. Med Phys, 2002. 29(12): p. 2799-805.

30. Dean-Ben, X.L., et al., Statistical Approach for Optoacoustic Image Reconstruction in the Presence of Strong Acoustic Heterogeneities. Ieee Transactions on Medical Imaging, 2011. 30(2): p. 401-408.

31. Razansky, D., et al., Multispectral opto-acoustic tomography of deep-seated fluorescent proteins in vivo. Nature Photonics, 2009. 3(7): p. 412-417.

32. Ma, R., et al., Non-invasive whole-body imaging of adult zebrafish with optoacoustic tomography. Physics in medicine and biology, 2012. 57(22): p. 7227-7237.

33. Razansky, D., A. Buehler, and V. Ntziachristos, Volumetric real-time multispectral optoacoustic tomography of biomarkers. Nature Protocols, 2011. 6(8): p. 1121-1129.

34. Dean-Ben, X.L., et al., Accurate Model-Based Reconstruction Algorithm for Three-Dimensional Optoacoustic Tomography. Ieee Transactions on Medical Imaging, 2012. 31(10): p. 1922-1928.

35. Rosenthal, A., V. Ntziachristos, and D. Razansky, Model-based optoacoustic inversion with arbitrary-shape detectors. Medical Physics, 2011. 38(7): p. 4285-4295.

36. Wang, K., et al., Investigation of iterative image reconstruction in three-dimensional optoacoustic tomography. Phys Med Biol, 2012. 57(17): p. 5399-423.

37. Rosenthal, A., D. Razansky, and V. Ntziachristos, Fast Semi-Analytical Model-Based Acoustic Inversion for Quantitative Optoacoustic Tomography. Ieee Transactions on Medical Imaging, 2010. 29(6): p. 1275-1285.

38. Dean-Ben, X.L., V. Ntziachristos, and D. Razansky, Acceleration of Optoacoustic Model-Based Reconstruction Using Angular Image Discretization. Ieee Transactions on Medical Imaging, 2012. 31(5): p. 1154-1162.

39. Szabo, T.L., (2004). Diagnostic Ultrasound Imaging: Inside Out. New York, NY: Elsevier Academic Press.

40. Saunders., C.C.P.a.M.A., Lsqr: An algorithm for sparse linear equations and sparse least square. ACM Transactions on Mathematical Software. 8(1): p. 43-71.

41. Buehler, A., et al., Model-based optoacoustic inversions with incomplete projection data. Medical Physics, 2011. 38(3): p. 1694-1704.

42. Hansen, C., Rank-Deficient and Discrete Ill-Posed Problems: Numerical Aspects of Linear Inversion. 1998: Society for Industrial and Applied Mathematics. 263.

43. Dean-Ben, X.L., et al., Weighted model-based optoacoustic reconstruction in acoustic scattering media. Physics in Medicine and Biology, 2013. 58(16): p. 5555-5566.

44. Queiros, D., et al., Modeling the shape of cylindrically focused transducers in three-dimensional optoacoustic tomography. Journal of Biomedical Optics, 2013. 18(7).

45. Mitsuhashi, K., K. Wang, and M.A. Anastasio, Investigation of the far-field approximation for modeling a transducer's spatial impulse response in photoacoustic computed tomography. Photoacoustics, 2014. 2(1): p. 21-32.

46. Araque Caballero, M.A., et al., Model-based optoacoustic image reconstruction of large three-dimensional tomographic datasets acquired with an array of directional detectors. IEEE Trans Med Imaging, 2014. 33(2): p. 433-43.

47. Aguirre, J., et al., A low memory cost model based reconstruction algorithm exploiting translational symmetry for photoacoustic microscopy. Biomedical Optics Express, 2013. 4(12): p. 2813-2827.

48.   Lutzweiler, C., X.L. Dean-Ben, and D. Razansky, Expediting model-based optoacoustic reconstructions with tomographic symmetries. Medical Physics, 2014. 41(1).

49.   Zhang, H.F., K. Maslov, and L.H.V. Wang, In vivo imaging of subcutaneous structures using functional photoacoustic microscopy. Nature Protocols, 2007. 2(4): p. 797-804.

50.   Razansky, D., Multispectral Optoacoustic Tomography-Volumetric Color Hearing in Real Time. Ieee Journal of Selected Topics in Quantum Electronics, 2012. 18(3): p. 1234-1243.

51.   Glatz, J., et al., Blind source unmixing in multi-spectral optoacoustic tomography. Optics express, 2011. 19(4): p. 3175-84.

52.   Cox, B., et al., Quantitative spectroscopic photoacoustic imaging: a review. Journal of Biomedical Optics, 2012. 17(6).

53.   Dean-Ben, X.L., et al., Fast unmixing of multispectral optoacoustic data with vertex component analysis. Optics and Lasers in Engineering, 2014. 58: p. 119-125.

54.   Weissleder, R.a.e.I., Molecular imaging principles and practice. Vol. p. xxii, 1357 p. 2009: People's Medical Pub. House,: Shelton, Conn.

55.   Eghtedari, M., et al., High sensitivity of in vivo detection of gold nanorods using a laser optoacoustic imaging system. Nano Letters, 2007. 7(7): p. 1914-1918.

56.   Liang, F. and B. Chen, A Review on Biomedical Applications of Single-Walled Carbon Nanotubes. Current Medicinal Chemistry, 2010. 17(1): p. 10-24.

57.   Filonov, G.S., et al., Deep-Tissue Photoacoustic Tomography of a Genetically Encoded Near-Infrared Fluorescent Probe. Angewandte Chemie-International Edition, 2012. 51(6): p. 1448-1451.

58.   de la Zerda, A., et al., Family of Enhanced Photoacoustic Imaging Agents for High-Sensitivity and Multiplexing Studies in Living Mice. Acs Nano, 2012. 6(6): p. 4694-4701.

59.   Lamela, H., V. Cunningham, and D.C. Gallego, Experimental study using optoacoustic spectroscopy (OAS) on spherical gold nanoparticles. Optics and Laser Technology, 2011. 43(1): p. 143-146.

60.   Kircher, M.F., et al., A brain tumor molecular imaging strategy using a new triple-modality MRI-photoacoustic-Raman nanoparticle. Nature Medicine, 2012. 18(5): p. 829-U235.

61.   Jokerst, J.V., et al., Gold Nanorods for Ovarian Cancer Detection with Photoacoustic Imaging and Resection Guidance via Raman Imaging in Living Mice. Acs Nano, 2012. 6(11): p. 10366-10377.

62.   de la Zerda, A., et al., Ultrahigh Sensitivity Carbon Nanotube Agents for Photoacoustic Molecular Imaging in Living Mice. Nano Letters, 2010. 10(6): p. 2168-2172.

63.   Liong, M., et al., Multifunctional inorganic nanoparticles for imaging, targeting, and drug delivery. Acs Nano, 2008. 2(5): p. 889-896.

64.	Zhang, Y., H. Hong, and W. Cai, Photoacoustic imaging. Cold Spring Harbor protocols, 2011. 2011(9).

65.	Luke, G.P., D. Yeager, and S.Y. Emelianov, Biomedical applications of photoacoustic imaging with exogenous contrast agents. Annals of Biomedical Engineering, 2012. 40(2): p. 422-37.

66.	Laufer, J., E. Zhang, and P. Beard, Evaluation of Absorbing Chromophores Used in Tissue Phantoms for Quantitative Photoacoustic Spectroscopy and Imaging. Ieee Journal of Selected Topics in Quantum Electronics, 2010. 16(3): p. 600-607.

67.	Chang, S.S., et al., The shape transition of gold nanorods. Langmuir : the ACS journal of surfaces and colloids, 1999. 15(3): p. 701-709.

68.	Buehler, A., et al., Video rate optoacoustic tomography of mouse kidney perfusion. Optics letters, 2010. 35(14): p. 2475-2477.

69.	Basic Concepts Of Analytical Chemistry. New Age International; 1998. 504 p.

70.	Eilert-Zell K. Characterization of a combined optoacoustic / ultrasound system (OPUS) for tomographic absorption measurements [Internet]. Technische Universität München; 2012 [cited 2014 Nov 7]. Available from: https://mediatum.ub.tum.de/?id=1113311

71.	Marshall, M.V., et al., Near-Infrared Fluorescence Imaging in Humans with Indocyanine Green: A Review and Update. Open Surg Oncol J, 2010. 2(2): p. 12-25.

72.	Briely-Sæbø K, B.A. Accurate de-oxygenation of ex vivo whole blood using sodium dithionite. in Proc 8th Annual Meeting, ISMRM. 2000. Denver.

73.	Tredan, O., et al., Drug resistance and the solid tumor microenvironment. Journal of the National Cancer Institute, 2007. 99(19): p. 1441-1454.

74.	Condeelis, J. and J.E. Segall, Intravital imaging of cell movement in tumours. Nat Rev Cancer, 2003. 3(12): p. 921-30.

75.	Wang, X., et al., Application of nanotechnology in cancer therapy and imaging. CA Cancer J Clin, 2008. 58(2): p. 97-110.

76.	Conway, J.R., N.O. Carragher, and P. Timpson, Developments in preclinical cancer imaging: innovating the discovery of therapeutics. Nat Rev Cancer, 2014. 14(5): p. 314-28.

77.	Li, C., A targeted approach to cancer imaging and therapy. Nat Mater, 2014. 13(2): p. 110-5.

78.	Hoffman, R.M., The multiple uses of fluorescent proteins to visualize cancer in vivo. Nat Rev Cancer, 2005. 5(10): p. 796-806.

79.	Brindle, K., New approaches for imaging tumour responses to treatment. Nat Rev Cancer, 2008. 8(2): p. 94-107.

80.	Emblem, K.E., et al., Vessel architectural imaging identifies cancer patient responders to anti-angiogenic therapy. Nat Med, 2013. 19(9): p. 1178-83.

81.	Atreya, R., et al., In vivo imaging using fluorescent antibodies to tumor necrosis factor predicts therapeutic response in Crohn's disease. Nat Med, 2014. 20(3): p. 313-8.

82. Ellenbroek, S.I. and J. van Rheenen, Imaging hallmarks of cancer in living mice. Nat Rev Cancer, 2014. 14(6): p. 406-18.

83. Wang, X., et al., Noninvasive laser-induced photoacoustic tomography for structural and functional in vivo imaging of the brain. Nature biotechnology, 2003. 21(7): p. 803-6.

84. Gamelin, J., et al., Curved array photoacoustic tomographic system for small animal imaging. Journal of biomedical optics, 2008. 13(2): p. 024007.

85. Burgholzer, P., et al., Thermoacoustic tomography with integrating area and line detectors. Ieee Transactions on Ultrasonics Ferroelectrics and Frequency Control, 2005. 52(9): p. 1577-1583.

86. Jose, J., et al., Passive element enriched photoacoustic computed tomography (PER PACT) for simultaneous imaging of acoustic propagation properties and light absorption. Optics Express, 2011. 19(3): p. 2093-2104.

87. Gamelin, J., et al., A real-time photoacoustic tomography system for small animals. Optics Express, 2009. 17(13): p. 10489-10498.

88. Xia, J., et al., Whole-body ring-shaped confocal photoacoustic computed tomography of small animals in vivo. Journal of Biomedical Optics, 2012. 17(5).

89. Duarte, F.J., Spectroscopic applications of tunable optical parametric osciltors, in Tunable Laser Applications. 2009, CRC: New York.

90. Institute, A.L., American National Standards for the Safe Use of Lasers. 2000.

91. Wang, K., et al., An imaging model incorporating ultrasonic transducer properties for three-dimensional optoacoustic tomography. Ieee Transactions on Medical Imaging, 2011. 30(2): p. 203-14.

92. Ma, R., et al., Multispectral optoacoustic tomography (MSOT) scanner for whole-body small animal imaging. Optics express, 2009. 17(24): p. 21414-26.

93. van Daatselaar, A.N., P.F. van der Stelt, and J. Weenen, Effect of number of projections on image quality of local CT. Dentomaxillofacial Radiology, 2004. 33(6): p. 361-369.

94. Dean-Ben, X.L., A. Ozbek, and D. Razansky, Volumetric Real-Time Tracking of Peripheral Human Vasculature With GPU-Accelerated Three-Dimensional Optoacoustic Tomography. Ieee Transactions on Medical Imaging, 2013. 32(11): p. 2050-2055.

95. Frangi, A.F.e.a., Multiscale Vessel Enhancement Filtering. MICCAI, 1998. 1496: p. 130-137.

96. Ale, A., et al., FMT-XCT: in vivo animal studies with hybrid fluorescence molecular tomography-X-ray computed tomography. Nature Methods, 2012. 9(6): p. 615.

97. Ale, A., et al., Imaging performance of a hybrid x-ray computed tomography-fluorescence molecular tomography system using priors. Medical Physics, 2010. 37(5): p. 1976-1986.

98.   Beziere, N., et al. Rethinking Optoacoustic Contrast: PEGylated Liposomal ICG within the Tumor Micro-environment. Biomater 2014.

99.   Al-Jamal, W.T. & Kostarelos, K. Liposomes: from a clinically established drug delivery system to a nanoparticle platform for theranostic nanomedicine. Accounts of chemical research 44, 1094-1104 (2011).

100.   Kim, J.W., et al., Golden carbon nanotubes as multimodal photoacoustic and photothermal high-contrast molecular agents. Nature Nanotechnology, 2009. 4(10): p. 688-694.

101.   Li, P.C., et al., In vivo Photoacoustic Molecular Imaging with Simultaneous Multiple Selective Targeting Using Antibody-Conjugated Gold Nanorods. Optics Express, 2008. 16(23): p. 18605-18615.

102.   Mallidi, S., et al., Molecular specific optoacoustic imaging with plasmonic nanoparticles. Optics Express, 2007. 15(11): p. 6583-6588.

103.   Chen, J.Y., et al., Immuno gold nanocages with tailored optical properties for targeted photothermal destruction of cancer cells. Nano Letters, 2007. 7(5): p. 1318-1322.

104.   West, J.L. and N.J. Halas, Engineered nanomaterials for biophotonics applications: Improving sensing, imaging, and therapeutics. Annual Review of Biomedical Engineering, 2003. 5: p. 285-292.

105.   Huang, X.H., et al., Cancer cell imaging and photothermal therapy in the near-infrared region by using gold nanorods. Journal of the American Chemical Society, 2006. 128(6): p. 2115-2120.

106.   Huang, X.H., et al., Plasmonic photothermal therapy (PPTT) using gold nanoparticles. Lasers in Medical Science, 2008. 23(3): p. 217-228.

107.   Kumar, S., et al., Plasmonic nanosensors for imaging intracellular biomarkers in live cells. Nano Letters, 2007. 7(5): p. 1338-1343.

108.   Loo, C., et al., Immunotargeted nanoshells for integrated cancer imaging and therapy. Nano Letters, 2005. 5(4): p. 709-711.

109.   Kumar, S., J. Aaron, and K. Sokolov, Directional conjugation of antibodies to nanoparticles for synthesis of multiplexed optical contrast agents with both delivery and targeting moieties. Nature Protocols, 2008. 3(2): p. 314-320.

110.   Lee, K.S. and M.A. El-Sayed, Gold and silver nanoparticles in sensing and imaging: Sensitivity of plasmon response to size, shape, and metal composition. Journal of Physical Chemistry B, 2006. 110(39): p. 19220-19225.

111.   Jain, P.K., et al., Calculated absorption and scattering properties of gold nanoparticles of different size, shape, and composition: Applications in biological imaging and biomedicine. Journal of Physical Chemistry B, 2006. 110(14): p. 7238-7248.

112.   Skrabalak, S.E., et al., Gold Nanocages: Synthesis, Properties, and Applications. Accounts of Chemical Research, 2008. 41(12): p. 1587-1595.

113. Yang, X.M., et al., Photoacoustic tomography of a rat cerebral cortex in vivo with au nanocages as an optical contrast agent. Nano Letters, 2007. 7(12): p. 3798-3802.
114. Li, M.L., et al., In-vivo photoacoustic microscopy of nanoshell extravasation from solid tumor vasculature. Journal of Biomedical Optics, 2009. 14(1).
115. Kim, C., et al., In Vivo Molecular Photoacoustic Tomography of Melanomas Targeted by Bioconjugated Gold Nanocages. Acs Nano, 2010. 4(8): p. 4559-4564.
116. Demers, M., et al., Increased Efficacy of Breast Cancer Chemotherapy in Thrombocytopenic Mice. Cancer Research, 2011. 71(5): p. 1540-1549.
117. Fogh, J., J.M. Fogh, and T. Orfeo, One hundred and twenty-seven cultured human tumor cell lines producing tumors in nude mice. J Natl Cancer Inst, 1977. 59(1): p. 221-6.
118. Sarantopoulos, A., G. Themelis, and V. Ntziachristos, Imaging the Bio-Distribution of Fluorescent Probes Using Multispectral Epi-Illumination Cryoslicing Imaging. Molecular Imaging and Biology, 2011. 13(5): p. 874-885.
119. Lillie, R.D., P. Pizzolato, and P.T. Donaldson, Nuclear stains with soluble metachrome metal mordant dye lakes. The effect of chemical endgroup blocking reactions and the artificial introduction of acid groups into tissues. Histochemistry, 1976. 49(1): p. 23-35.